JOURNAL OF THE

AERONAUTICAL SCIENCES

VOLUME 25 JANUARY, 1958 NUMBER 1

ST LOUIS PUBLIC LIBRARY NOV 10 1959

CONTENTS

Experimental Investigation of the Rotating Stall in a Single-Stage Axial Compressor ..... JACQUES VALENSI 1

Aerodynamics of Nonuniform Flows as Related to an Airfoil Extending Through a Circular Jet ..... SCOTT RETHORST 11

The Hydrodynamics and Heat Conduction of a Melting Surface ..... GEORGE W. SUTTON 29

Incompressible Potential Flow About Axially Symmetric Bodies in Ducts ..... PHILIP LEVINE 33

The Crippling Strength of Compression Elements ..... GEORGE GERARD 37

The Characteristics of Two-Dimensional Sails in Hypersonic Flow ..... WALTER DASKIN AND LEWIS FELDMAN 53

Readers' Forum 56

Published by
INSTITUTE OF THE AERONAUTICAL SCIENCES, INC.

JOURNAL OF THE AERONAUTICAL SCIENCES

Editor: W. R. Sears
Director, Graduate School of Aeronautical Engineering, Cornell University

Associate Editor: Robert R. Dexter *Managing Editor:* Rita J. Turino
Editorial Assistant: Caroline Taylor

Editorial Committee

Aerodynamics and Fluid Mechanics

Holt Ashley
H. Julian Allen
Dean R. Chapman
Francis H. Clauser
Hugh L. Dryden
John C. Evvard
Antonio Ferri
Alexander Flax
Wallace D. Hayes
R. T. Jones
Carl Kaplan
H. W. Liepmann
C. C. Lin
H. F. Ludloff
Harold Luskin
Clark B. Millikan
Henry T. Nagamatsu
H. J. E. Reid
George S. Schairer
G. B. Schubauer
John Stack
Theodore Theodorsen
Arthur N. Tifford
Th. von Kármán

Flight Testing

R. R. Gilruth
Melvin N. Gough
W. L. Howland
W. F. Milliken, Jr.

Rotating Wing Aircraft

F. B. Gustafson
K. H. Hohenemser
Bartram Kelley
R. B. Maloy
Ralph McClarren
R. H. Miller
R. H. Prewitt
Igor I. Sikorsky

Structures

John E. Duberg
R. R. Heldenfels
N. J. Hoff
Samuel Levy
J. F. McBrearty
W. Ramberg
E. E. Sechler
F. R. Shanley
C. R. Strang
S. Timoshenko

Meteorology

C. F. Brooks
D. M. Little
F. W. Reichelderfer
K. C. Spengler

Vibration and Flutter

Lee Arnold
M. A. Biot
R. L. Bisplinghoff
Harold A. Cheilek
I. E. Garrick
Martin Goland

Aircraft Design

W. E. Beall
E. H. Heinemann
Hall L. Hibbard
Richard Hutton
C. L. Johnson
A. A. Kartveli
F. K. Teichmann

Electronics

K. C. Black
M. V. Kiebert, Jr.
David S. Little
Paul Rosenberg
Giles J. Strickroth

Physiologic Problems

H. G. Armstrong
Louis H. Bauer
Robert J. Benford
W. Randolph Lovelace, II
Ross A. MacFarland

Flight Propulsion

William Bollay
George W. Brady
R. P. Kroon
Frank E. Marble
Abe Silverstein
E. S. Taylor

Instruments

Alan G. Binnie
Charles H. Colvin
Frank R. Cook
C. S. Draper
S. G. Eskin
C. F. Savage
R. C. Sylvander

SUBSCRIPTION RATES

Journal of the Aeronautical Sciences, Published Monthly. United States and Possessions: 1 Year, $15.00; Single Copies, $1.50. Foreign Countries Including Canada (American Currency Rates): 1 Year, $16.00; Single Copies, $1.50.

Aeronautical Engineering Review, Published Monthly. United States and Possessions: 1 Year, $5.00; Single Copies, $0.50. Foreign Countries Including Canada (American Currency Rates): 1 Year, $6.00; Single Copies, $0.50.

Notices of change of address should be sent to the Institute at least 30 days prior to actual change of address.

Manuscripts for publication, proofs, and all correspondence should be addressed to the Editorial Office of the Journal.

Publication Office, 20th and Northampton Sts., Easton, Pa. Correspondence regarding subscriptions may be addressed to the Editorial Office of the Journal of the Aeronautical Sciences, 2 East 64th Street, New York 21, N.Y.

© *Copyright, 1957, by the Institute of the Aeronautical Sciences, Inc.*

Entered as Second-Class Matter at the Post Office, Easton, Pa., May 1, 1937. Acceptance for mailing at a special rate of Postage provided for in the Act of August 24, 1912. Authorized April 29, 1937.

W

H

co
bo
st
re
ti
up
vi
we
wi
re

th
fo
bl
ro

in
se
to
w

w
m
ro
re
cy

va
fr
st
by
ar

pr

A
vi

de
ar
th

F

Applied Science Dept.

JOURNAL OF THE AERONAUTICAL SCIENCES

VOLUME 25 JANUARY, 1958 NUMBER 1

Experimental Investigation of the Rotating Stall in a Single-Stage Axial Compressor*

JACQUES VALENSI**

Institut de Mécanique des Fluides de l'Université d'Aix-Marseille

SUMMARY

The investigation was conducted on a single-stage axial flow compressor consisting of a row of 30 inlet guide vanes with solid body prerotation followed by a row of 31 rotor blades with constant work along radius, at design, and a row of 34 stator blades re-establishing conditions at rotor inlet. The stage has a hub to tip diameter ratio of 0.5 with a tip diameter of 0.50 m. and is set up between an entrance cone and a diffuser with a throttling device at the downstream end. The rotating stall characteristics were carefully investigated by pressure measurements performed with stagnation and static pressure probes connected to quick response pressure gages, as well as by smoke observations.

The stall occurs toward the tip of rotor blades with closing throttle at the peak pressure point. It appears initially in the form of a single propagating stall region, which interests three blade channels and which rotates at a speed equal to 0.68 the rotor speed.

The number of stalled regions increases upon further decrease in flow rate, from one to eight regions. Further throttling causes separation at the suction side of the guide vanes; a one-region total span rotating stall is then observed on the guide vanes, which affects the instantaneous flow rate through the stage.

The propagation speed of the stall, and to a certain extent, the width of the stalled regions, appear to be independent of the number of regions for the first kind of stall which originates at the rotor blade tips. However, the intensity of stall of the different regions is largely and erratically variable from one to another cycle of rotating stall, especially for the multi-region pattern.

Stroboscopic observation of smoke filaments shows a cyclic variation of the air velocity direction at the rotor inlet, with a frequency equal to the number of turns per second of rotation stall times the number of regions. The variation is governed by separation on the rotor blades and increases gradually in amplitude with the number of stalled regions.

High-frequency pictures confirm the observations made with pressure gages.

Presented at the Aerodynamics—I Session, Twenty-Fifth Annual Meeting, IAS, New York, January 28–31, 1957. Revised and received September 4, 1957.

* The results presented in this paper form a portion of research done under the sponsorship of the European Office of the ARDC and with the assistance of Societe EM. Hispano Suiza by whom the blades were manufactured.

** Professor, Faculty of Sciences, and Director, Institute of Fluid Mechanics.

SYMBOLS

V = vector absolute velocity
W = vector relative velocity
v = tangential component of absolute velocity
w = axial component of absolute velocity
u_0 = tip velocity
u = circumferential velocity at radius r
φ = dimensionless axial velocity at radius r, w/U_0
ϕ = average flow coefficient
λ = dimensionless tangential velocity at radius r
r_0 = radius at the tip of the blades
ξ = dimensionless radius r/r_0
c = airfoil chord length
s = cascade pitch
t = maximum thickness of cylindrical sections of blades
α = direction of absolute velocity from compressor axis
β = direction of relative velocity from compressor axis
ψ_t = local total pressure rise coefficient
Ψ_t = mass weighted average total pressure rise coefficient
ψ_s = local static pressure rise coefficient
Ψ_s = mass weighted average static pressure rise coefficient
η = compression efficiency
N = r.p.m.
h = absolute rotative speed of rotating stall
C_L = lift coefficient per unit length of blade
C_D = drag coefficient per unit length of blade

(1) INTRODUCTION

ROTATING STALL in an axial compressor has been the object of extensive experimental investigations† during the course of the last few years. Its characteristics have been described in many instances and its mechanism seems to be clearly understood. So far, two main methods of approach have been used—the hot wire anemometer technique and static pressure measurements. In order to complete the observation already described, an attempt has been made to apply two other methods of approach for investigating the rotating stall on a single stage axial flow compressor—stagnation pressure measurements and smoke surveys.

† See References.

A716696

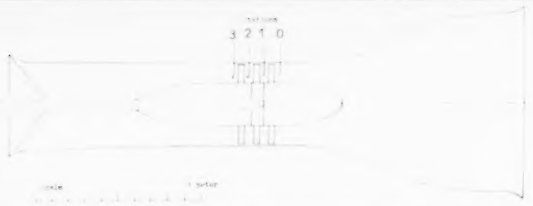

FIG. 1. Schematic diagram of compressor installation and axial measuring stations along compressor.

Both methods complete each other and, together with static pressure measurements, seem to permit a precise determination of rotating stall characteristics.

Smoke observations show the development of stalling on the rotor blades quite clearly; they confirm the assumptions already made for the mechanism of the onset of rotating stall. The rotor speed being kept constant, partial-span stall is first observed at the tip of rotor blades, with closing throttle from peak pressure point. The number of stalled regions increases upon further decrease in flow rate, from one to eight regions, while no significant variation is observed in the speed of stall. Further throttling causes separation on the suction side of the guide vanes, the severity of which increases towards the tip. A one-region total-span rotating stall is then observed on the guide vanes, which affects the flow rate through the stage. The absolute speed of this stall is about three times lower than the speed of partial stall on the rotor blades. Further decreases in flow rate cause the disappearance of periodic phenomena; random stall is observed until, at a very low flow rate, an intense one-region root to tip stall is initiated on the rotor blades. Reverse flow is then observed in the stalled region, which extends through the entire stage, up to a certain distance upstream of the guide vanes.

Thence three distinct types of stall are observed; multiregions are observed only in the first type, and the stall speed seems in this case not to depend on the number of regions. As to the instantaneous flow rate at a given point, it remains constant at a given throttle for the first type of rotating stall, while it fluctuates periodically for the second and third types, although in these latter cases the mean flow rate through the compressor remains constant.

Those results may hold only for the present particular design, but it must be stressed that this design simulates internal flow commonly employed in modern high-performance turbomachines.

An attempt has been made of the application of existing theories for the prediction of stall propagation speed of the rotating stall of the first type. In this case the stall interests only a narrow field about the rotor row, an assumption which is made in most of the calculations. Sears theory[9] yields results in agreement with the experiments, so long a suitable lag is introduced, of which evidence seems to be given by the smoke pictures (see, for instance, Plates 1 and 2). Some details of the application of the Fabri and Siestrunck theory,[11] as suggested by Prof. M. Roy, are given in the Appendix.

TABLE 1

Distributor (30 blades)					
ξ	0.50	0.625	0.75	0.875	1
s/c	0.523	0.653	0.783	0.913	1.047
c (mm.)	50	50	50	50	50
t/c (max.)	0.124	0.112	0.0993	0.087	0.0734
α_1° (outlet)	14°39′	18°24′	22°13′	26°09′	30°25′
$C_L \cdot (c/s)$	0.519	0.656	0.800	0.954	1.126
Rotor (31 blades)					
s/c	0.551	0.703	0.861	1.028	1.207
c (mm.)	46	45	44	43	42
t/c (max.)	0.150	0.130	0.110	0.090	0.070
β_1° (inlet)	31°28′	39°38′	47°31′	55°09′	63°
β_2° (outlet)	−24°08′	−5°19′	13°53′	31°43′	48°04′
$C_L \cdot (c/s)$	2.114	1.730	1.404	1.140	0.927
Stator (34 blades)					
s/c	0.511	0.641	0.768	0.895	1.027
c (mm.)	45	45	45	45	45
t/c (max.)	0.140	0.123	0.105	0.088	0.070
α_1° (outlet)	12°28′	16°39′	21°30′	27°23′	35°20′
α_2° (inlet)	52°02′	50°40′	51°07′	53°11′	57°20′
$C_L \cdot (c/s)$	1.736	1.488	1.316	1.162	1.081

(2) TEST COMPRESSOR

The stage consists of a row of 30 inlet guide vanes with solid body prerotation, followed by a row of 31 rotor blades with constant work along radius at design, and a row of 34 stator blades re-establishing flow conditions at rotor inlet. Design flow angles at the rows from the axial direction, as well as the main characteristics of the blades, are given in Table 1. The stage has a hub to tip diameter ratio of 0.5, with a tip diameter of 0.50m. The blading was computed, with the assumption of perfect fluid, by the use of the linearized three-dimensional flow theory (axisymmetric flow) to give a total pressure rise coefficient of 0.637 at a flow ratio of 0.48.

The cylindrical sections of the blades at different radii were computed as cascades of airfoils, by means of the conformal transformation of suitable ovals. The design allowed sufficient space between the rows for the instrumentation required to permit a detailed analysis of blade row flow distribution; the cylindrical casing was made of transparent perspex to permit visual observations. A cross-sectional view of the test installation is presented in Fig. 1, where the principal dimensions are summarized.

The air flows into the compressor through a double curvature entrance cone. The shape of this cone as well as the streamlined shape of the front part of the hub have been designed so as to provide a uniform flow across the compressor inlet, with a very thin boundary layer at the walls. The contraction ratio is about 6.4. A fine gauze was installed at the entrance cone inlet in order to damp out eventual gusts. Two short ducts of constant annulus area are seen between the compressor stage itself, on one hand, and between the compressor stage and exit cone, on the other hand. Those ducts are of sufficient length for allowing the flow to assume very nearly its asymptotic pattern and permit easy measurements. An interconnected set of four

Ref. 629.1
Shelved w. 050
APR 19

1 (smooth flow)

2

3

4

5 (complete stall)

7 (complete stall)

PLATE 1. Rotating stall, second type (high-frequency pictures), $\phi = 0.313$, $\xi = 0.88$, 2,460 r.p.m., time interval between successive pictures = 1/450 sec.

1

2 (smooth flow)

3

4 (onset of stall)

5 (stall)

6 (flow reestablished)

PLATE 2. Five region rotating stall (high-frequency pictures), $\phi = 0.37$, $\xi = 0.88$, 2,460 r.p.m., time interval between successsive pictures = 1/450 sec.

wall static pressure orifices is located midway through the front cylindrical duct, which was calibrated to give the total flow coefficient. The exit portion of the installation consists of a slightly diverging duct with an expansion area ratio of 1.36. The throttling device at the downstream end of the exit cone is driven by an electric motor operated from the test bed stand.

In order to permit easy visual observations, the blades of the three rows are set on the hubs. The pieces of metal required for holding the instrument carriages screwed on the outside wall of the casing make only a small obstruction. A driving mechanism allows the rotation of the casing; the clearance between the tips and the casing is 0.2 to 0.6 mm. A 22 hp. electric asynchronous motor drives the compressor shaft by means of pulleys and belts.

Most of the measurements were made at a rotative speed of 2,460 r.p.m.; hence, compressibility effects were negligible, and the blades could be considered rigid as far as aerodynamic forces were concerned. The power input to the compressor could be found from accurate measurements of the rotative speed and of the driving torque which was determined by means of a torquemeter.

(3) Instrumentation

For the evaluation of overall performance and individual blade row flow details, in the normal range of operation as well as inside the rotating stall range, extensive instrumentation was located at stations 0, 1, 2, and 3 as shown in Fig. 1. Stations 1 and 2 are situated midway between adjacent rows; station 0 and 3 are situated midway through the front and rear ducts of constant annulus area. Static pressure orifices were provided also at the outer wall immediately upstream and downstream of the rotor blade tips.

Flow Rate Measurements

Station 0 was used to determine the radial distribution of velocity at the compressor inlet and consequently, by integration, the flow rate as a function of the rotational speed and of the throttle position. To this effect a static probe of the conventional type was shifted radially and, *for steady flow*, readings were taken on an alcohol manometer, of the pressure difference between the pressure transmitted by the probe and the stagnation pressure at the hub nose. This last pressure was taken as reference pressure in all pressure measurements. The set of static holes at station 0 were calibrated after the static probe surveys. During operation with partial-span stall the net flow rate through the compressor and the torque necessary to drive the compressor remain essentially constant.

To permit the correct measurements of unsteady flow, (so long there is no return flow), the static probe was then connected to a dynamic pressure gage, as described below. Station 0 was also used for the distribution of smoke through streamlined tubes of convenient diameters in order to get a picture of the flow pattern through the stage, and especially upstream and downstream of the rotor row.

When return flow is observed at station 0, at very low flow rates, as will be seen further on, the rate of flow had to be measured by means of static pressure holes drilled on two flanges at the exit of the throttling device (those flanges are not shown in Fig. 1).

Evaluation of Flow Details at Station 1, 2, and 3 in the Normal Range of Operation

Station 1 was used to evaluate both the flow conditions downstream of rotor and upstream the stator. Station 3 was used for the evaluation of flow conditions downstream of stator.

Probe carriages at those three stations would permit radial surveys with different types of probes—one yaw and stagnation pressure probe of the well known claw type, and one static probe. Circumferential surveys were achieved by the rotation of the casing. The probe carriage could also hold minute streamlined tubes for smoke distribution, for carrying out detailed observations of the flow pattern through individual row.

Investigation of Flow Details in the Rotating Stall Range

The same stations as described above were used for the performance of pressure and smoke radial and circumferential surveys, but the instruments used for this part of the program are different from the ones used for investigations in the normal range of operation. Moreover, two more stations, a and b, already described, immediately upstream and downstream the rotor, were used for the measurement of static pressure by means of small orifices drilled through the casing.

The stagnation and static pressure probes are made of monel tubes of short length (about 60 mm.) and small inner diameter (1 mm.). The stagnation pressure heads are made as conventional pitot tubes, whereas the static pressure heads are of the disc type. Very short rubber tubing is used for connecting the probes with electrical pressure gages.

Electrical Pressure Gages

The electrical pressure gages are of the variable air gap inductance type. They answer to the following requirements: small size, good frequency response to several hundred cycles per second, insensitivity to mechanical vibrations, sensitivity at low pressures, convenient output, simple construction.

The gage components are arranged in the following way: a corrugated thin diaphragm of magnetic material (μ-metal), is clamped between two cup-shaped case halves (made also of μ-metal); each of them has a cylindrical core piece through which is drilled a pressure opening. An inductance coil is cemented about each core piece. Each case half, together with the diaphragm, constitutes, for the coil inside, a magnetic circuit with a small air gap (1/10 mm.) between the core piece and the diaphragm.

The pressure openings permit the connection of both the air gaps to two pressure probes or one to a

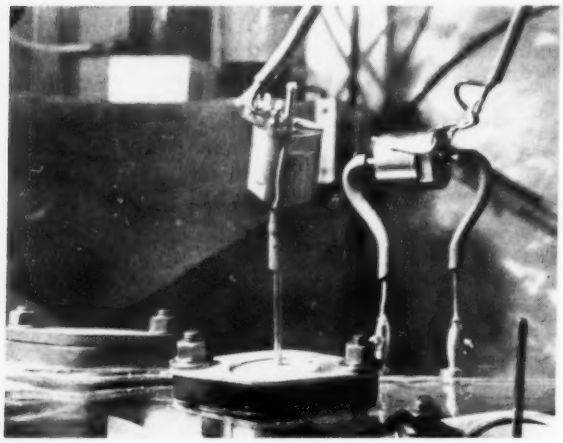

FIG. 2. Stagnation and static pressure taps in connection with pressure gages.

pressure probe on one side and the other to a pressure orifice at the hub nose (see Fig. 2). The coils are connected in adjacent arms of an a.c. Wheatstone bridge, which is fed by an audio frequency oscillator. The block diagram of the carrier equipment used is shown in Fig. 4; the electronic equipment itself is shown in Fig. 3. Galvanometers of the moving magnet type, of suitable natural frequency and damping, are used in the recorder. The static and dynamic behaviors of the pressure gages associated to different pressure heads have been thoroughly investigated.

Frequency response curves to direct repeated rectangular impulses were established with a pressure pulsator, simulating the flow conditions about the different heads, which are prevailing at the different stations when the compressor is stalling.

A typical static calibration curve is shown in Fig. 7, as well as a frequency response calibration curve. No acoustical resonances were observed up to frequencies of the order of 250 cycles per sec. Satisfactory behavior of the pressure gages was consequently to be expected for the investigation of rotating stall of which maximum apparent frequency is around 200 cycles per sec., when the rotational speed of the rotor is 2,460 r.p.m.

Smoke Generator and Light Sources

Ammonium chloride was used in the present investigation, as in the previous ones which the author had performed on propellers. This was produced with a generator described previously (see reference 12, pp. 46–48).

The smoke is distributed in the stream, most usually at station 0, with streamlined tubes made of monel which the smoke cannot corrode (the blades themselves made of duralumin are protected by a thin coat of alumin). Flashes are produced by discharge of a capacitor of suitable capacity in a tube containing rare gases and a few drops of mercury. The high voltage generator which has been used is the so called "stroborama" built by Seguin in Paris, in which a thyratron switch has been substituted for the mechanical one. This device can be used as a stroboscope with a flash frequency ranging between 6 to 50 per sec. Alternatively, series of 10 to 12 flashes of very short duration can be produced, the time interval between each flash varying between 1/300 to 1/1000 sec. In order to achieve the highest contrast for the observation of smoke filaments (the filament lines are as described by Bairstow), the light source must be located opposite to the observer. Also the use of a concave mirror in order to focus the light over the smoke jet is recommended.

(4) RESULTS AND DISCUSSION

Performance Characteristic of the Compressor in the Steady State, and in the Rotating Stall Range

Mass weighted average total and static pressure rise coefficients for the rotor are plotted in Fig. 5 against flow coefficient; they are based on the difference in pressure between stations 2 and 1.

Maximum pressure rise coefficients are seen to take place at $\phi = 0.388$. From this point, with further throttling Ψ_t seems to be decreasing continuously.

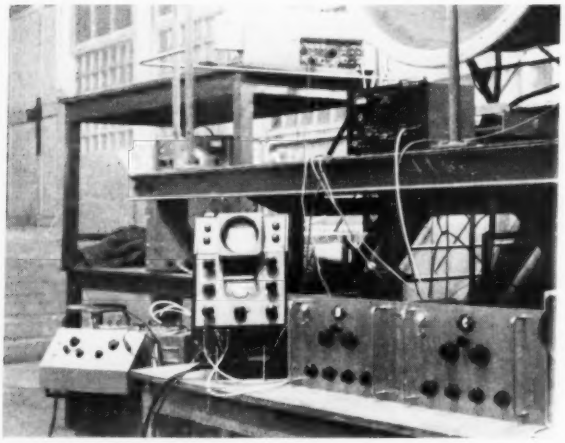

FIG. 3. Electronic equipment, stroborama, and recorder.

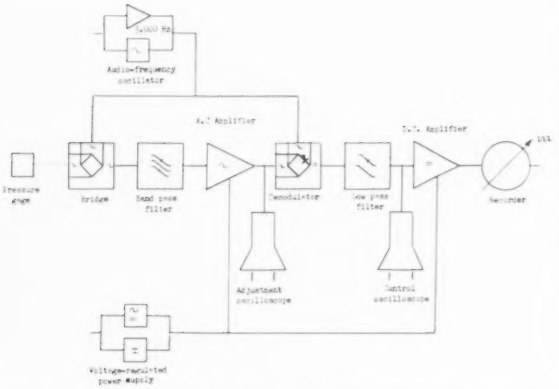

FIG. 4. Block diagram of the carrier equipment used with the pressure gages.

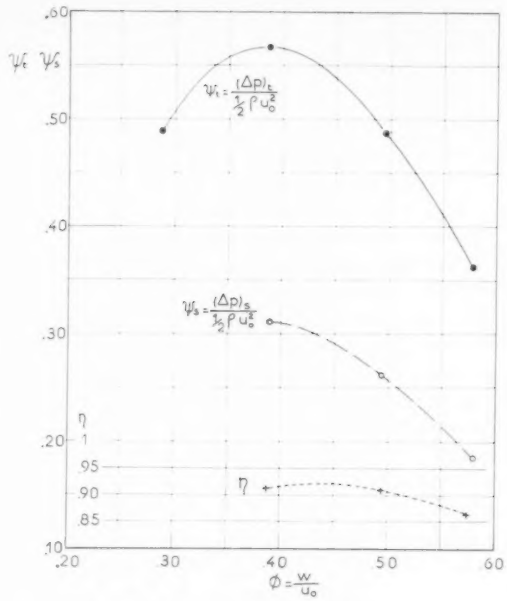

FIG. 5. Overall performances.

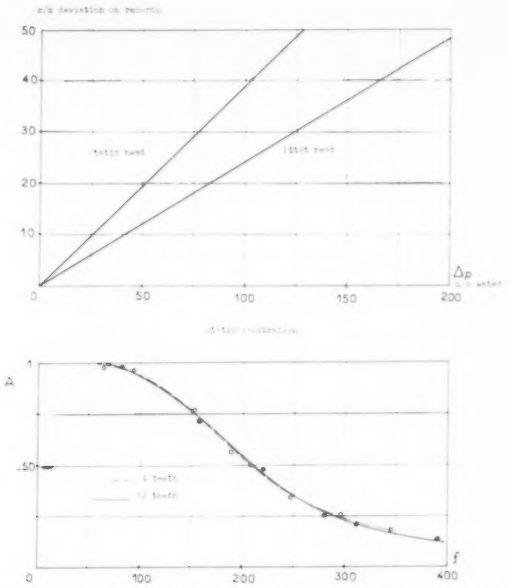

FIG. 7. Frequency response to square waved repeated pulses (pressure gage + probe + galvanometer).

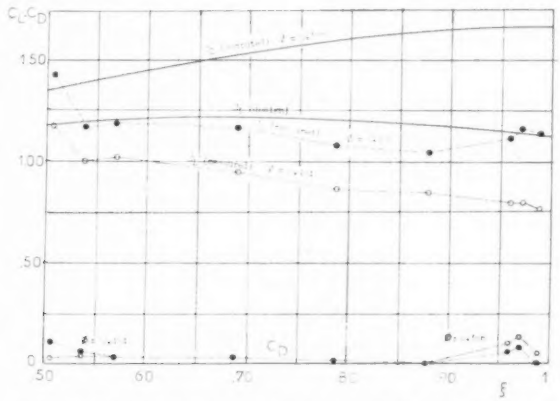

FIG. 6. Rotor cascade radial variation of C_L and C_D (measured and computed) $\phi = 0.484$, design, and 0.388 (peak pressure rise).

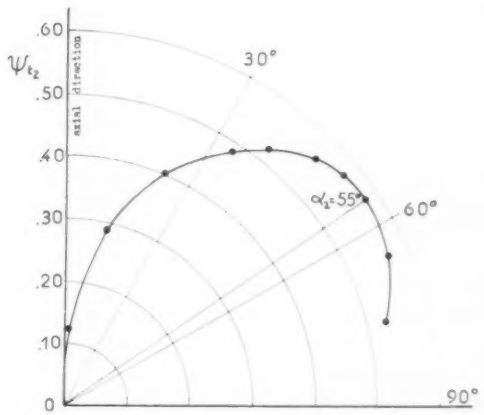

FIG. 8. Stagnation pressure rise readings against orientation angle of the probe.

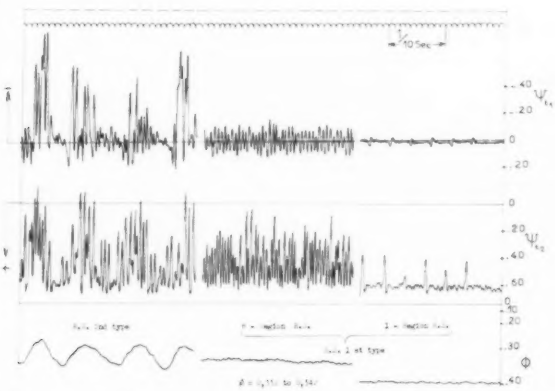

FIG. 9. Type of records at stations 1 and 2 (stagnation pressure probe) 2,460 r.p.m., $\xi = 0.896$.

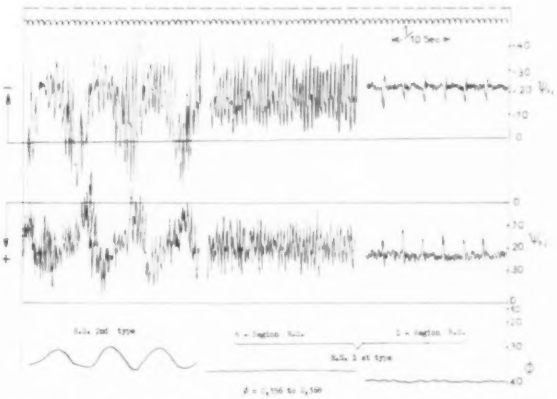

FIG. 10. Type of records at stations 1 and 2 (static pressure taps).

The efficiency curve, plotted also on the same Figure against ϕ, appears to be very flat in a wide range of flow coefficient, up to the peak pressure point.

Rotor cascades radial variation of C_L and C_D are plotted in Fig. 6 for design ϕ and $\phi = 0.388$ corresponding to maximum pressure rise. There is a tendency for C_L to increase towards the tips of the blades when the compressor is throttled. Simultaneously the C_D increases rapidly, forecasting the onset of stall, for sections toward the tips of the blades.

Rotating Stall Characteristics

The characteristics described hereafter are depicted after the examination of dynamic pressure records and from smoke observations performed as stated in Section (3) above. Those will be discussed below.

The stall occurs towards the tip of rotor blades with closing throttle at the peak pressure point. It appears initially in the form of a single propagating region. This type of stall starts at $\phi = 0.384$ and extends from the outer radius to $\xi = 0.75$, while toward the inner radius the fluctuations in pressure become much smaller and irregular. It interests three blade channels at the outer radius and contracts inwards.

Further throttling results in the formation of two stalled regions at $\phi = 0.38$, then of three, four, five, six, and eventually, seven or even eight regions, around $\phi = 0.35$.

The absolute rotating speed of the stall has been measured for all patterns by comparing records made with two stagnation pressure heads at station 2, 45° apart along the circumference. No significant variations are observed following the pattern; the rotating speed seems to be practically irrespective of the number of stalled regions and equal to 0.68 the rotating speed of the rotor. This fact is confirmed by stroboscopic observation of smoke as will be seen further on. Also the width of the regions and their radial extent seems not to depend on the number of regions.

However, the intensity of stall of the different regions appears to be largely and erratically variable from one to another cycle of rotating stall, especially when the number of regions is high (6 to 8); for instance, one or two regions may vanish and temporarily modify the pattern. Still, on the whole, the severity of stall seems to increase with the number of regions.

As a rule, for the two- and three-region pattern, the distribution of the regions is not regular along the cycle. But apart from the erratic variations pointed out above, the distribution of regions tends to become symmetrical over the cycle, when the number of regions is above three.

Simultaneously with the increase in number of regions, under $\phi = 0.35$, the stalled regions extend upstream of the rotor row. The interaction upon the flow round the guide vanes is large enough from $\phi = 0.35$ downwards, to cause separation on the suction side of these blades, from the leading edge. A one-region root to tip rotating stall pattern is then initiated along the guide vanes with increasing severity towards the tip, which affects the flow through the entire stage. It interests circumferentially half of the blades of the distributor row.

The absolute speed of the stall in terms of the speed of the rotor is 0.293. Therefore it is quite distinct from the previous speed of stall on the rotor, but it must be pointed out that this new speed corresponds to a quite different type of stall.

No change in the characteristics of this new pattern, apart from the severity of stall, is observed with closing throttle, down to $\phi = 0.245$. Further decreases of the flow rate cause the disappearance of the periodic phenomena. Random stall is then observed, with closing throttle, to be especially intense over the outer parts of the blades of the three rows, until, when $\phi = 0.146$, a sudden change of the pattern occurs—a one region root to tip stall is observed which is initiated on the rotor blades and interests half of the blades of the rotor row. In the stalled region, separation takes place from the leading edge of rotor blades and a reverse flow occurs through the entire stage, which extends up to a certain distance upstream of the guide vanes. To this new pattern of stall corresponds first a net increase of the mean flow rate, ϕ jumping from 0.145 to 0.213. Further throttling brings no change of this ultimate type of rotating stall, down to $\phi = 0.186$. Inside the range $0.213 \geqslant \phi \geqslant 0.186$, the absolute speed of stall remains constant and equal to 0.207, the rotational speed of the rotor.

To summarize, three distinct types of rotating stall are observed with closing throttle from peak pressure point. The first kind initiates on the rotor blades and affects only the outer parts of the rotor blades. The stalled region extend steadily upstream upon further throttling, until the second type of stall occurs as the result of separation over the guide vanes. The ultimate type of rotating stall is initiated on the rotor blades as the result of total span separation over those blades, from the leading edge. To the first type corresponds, for a given throttle and at a given point, no variation against time of the rate of flow through the stage. To the second and third types correspond, for a given throttle and at a given point, periodic fluctuations of the instantaneous rate of flow. Still in both those latter cases the mean flow rate through the stage remains constant. To each type of stall corresponds a given propagation speed, which is practically irrespective of the number of regions, at least for the first type. For the second and third type, a one-region stall only is observed.

Stagnation Pressure Fluctuations Due to Rotating Stall

An investigation has first been made of the influence of the angle of the pressure head, from the rotation axis, on the galvanometer readings. The head was held at station 2 and at $\xi = 0.964$ and was set at 55° from the rotation axis, which orientation was found to be correct by means of the yaw probe, in the steady state, at peak pressure rise ($\phi = 0.388$). Tests were then performed after further throttling, when the one or the four-

region stall was established. Decreasing or increasing the setting angle would result, after the readings, as shown in Fig. 8, in an apparent reduction of the maximum pressure rise during the periods when the flow is not separated. Consequently, the readings are assumed to be correct in the unstalled zones, when, at any radius, the head is set at an angle as determined by previous measurements in the steady state. It was admitted that such settings would be still convenient for measuring to a certain extent the pressure drops in the stall zones. At least the readings in the stall zones should permit an appreciation of the severity of the stall.

An example of stagnation pressure records at station 1 and 2 is given in Fig. 9, where are shown the time base (1/100 sec.); the fluctuations in pressure rise at station 2, with the stagnation pressure at the hub nose as reference pressure; the fluctuations in pressure rise at station 1, with the same reference pressure; and finally, the rate of flow as measured by means of a probe at a given circumferential position at station 0 (first and second types of stall).

The readings concerning the pressure fluctuations at station 1 are of small amplitude; they correspond, with decreasing flow, to a slight rise followed by a drop. Fluctuations in the direction of the velocity which are quite significant in this field, as will be seen further on, may have some bearings on the readings.

For the first type of rotating stall and for one-region stall the pressure drops at station 2 appear to be, on the average, equal to about one third of the pressure rise in the unstalled zones. The pressure rise coefficient outside the stall zones remains equal to the peak pressure rise in the steady state.

An example is given of the pressure records in the case of multiregion stall for eight-region stall, which occurs for ϕ from 0.332 to 0.342. Radial variation of relative stagnation pressure rise fluctuations and of maximum pressure rise coefficient at stations 2 and 3 and at $\phi = 0.384$ (one region stall), are shown in Fig. 11.

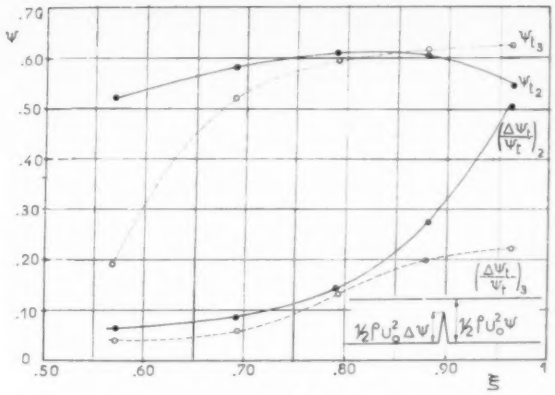

FIG. 11. Radial variation of relative stagnation pressure rise fluctuations and of maximum pressure rise coefficient at stations 2 and 3, 2,460 r.p.m., $\phi = 0.384$ (one-region stall).

Static Pressure Fluctuations for the First Type of Stall

Measurements at the Outer Wall.—The pressure are measured with the stagnation pressure at the hub nose as reference pressure. At station 2 a drop in pressure is observed in the stall zones, while, outside the stall zones and for patterns ranging from one- to four-region stall, the rise in pressure remains equal to the rise in the steady state at $\phi = 0.388$. This pressure rise decreases slightly with further throttling. At station 1 a pressure drop is observed outside the stall zone, which, when the number of regions is one or two, is equal to the pressure drop in the steady state at $\phi = 0.388$. In the stalled zones, with decreasing flow the fluctuation in pressure is composed of a rise in pressure followed by a drop. For one-region stall the fluctuations in pressure at station 2 are smaller than half the pressure rise outside the stall zone. At station 1 the increase in pressure corresponding to the fluctuations, and for the same stall pattern, is about one third of the pressure drop outside the stall zone; the decrease in pressure is about one quarter of the same pressure drop. For the same pattern and outside the stall zone, at station 2 the pressure rise is nearly equal to the pressure drop at station 1.

Similar phenomena are observed at stations a and b adjacent to the rotor on both sides. However, outside the stall zone the pressure differences are smaller compared with the differences in pressure measured at stations 1 and 2. Inside the stall zones, on the contrary, the fluctuations are far larger. A large part of this result seems to be due to a clearance effect.

An example of the static pressure records at stations 1 and 2 is shown in Fig. 10. The composition of this diagram is similar to that of Fig. 9. In the case of multiregion stall, the records concern the six-region stall pattern which occurs for ϕ between 0.356 and 0.368.

Measurements Along the Radius—The observations are very much similar to the ones above described.

Smoke Surveys and Smoke Pictures

Photographs have been taken of the filament lines in the steady state and in the rotating stall state. Those were taken with the apparatus already described, by means of an ordinary camera for stroboscopic observations, and by means of a rotating drum for images in rapid succession. A sample of the images in the steady state is shown in Fig. 12, corresponding very nearly to peak pressure rise.

All along the radius, vortices are seen shedding from the rotor blades, as the circulation in the flow increases from hub to tip. Although this is not apparent in the picture, those vortices are still present over the stator blades and even downstream of the stator.

Stroboscopic observations of smoke filaments between the distributor row and the rotor row and between the mean radius and the outer radius, performed at a frequency slightly smaller than the absolute rotational speed of the stall (first kind of rotating stall), show up for one-region stall—a nonuniform rotation of the filament lines in the sense of the stall rotation.

No significant variation of the rotational stall speed

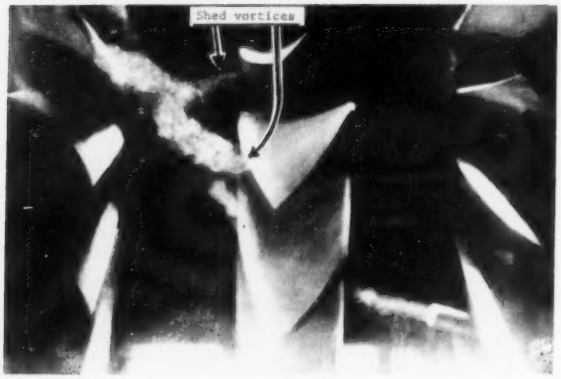

FIG. 12. Filament lines downstream of rotor, $\xi = 0.69$, $\phi = 0.40$, 2,460 r.p.m.

is observed with the number of regions. But the amplitude of the fluctuations of the filament lines increases with the number of regions, to become very large at flow rates corresponding to the second type of rotating stall. The frequency of fluctuations of the filament lines is equal to the rotational speed of propagation of the stall multiplied by the number of stalled regions. To these fluctuations correspond obviously a cyclic variation of the relative incidence at the rotor blades, which is far from being harmonic.

Plates 1 and 2 are extracted from high-speed films taken by means of the rotating drum. In both plates the number of frames per second ranges from 450 to 500.

Plate 1 concerns the second type of stall. The flow is seen to stall severely in the images 5 and 7. The following frame, which is not reproduced here, shows a reversal of the flow through the rotor; as a matter of fact, the air appears to be cycling in front of the rotor in the stalled regions. The complete stalling cycle appears to last about 2/100 sec. Such a time seems to be rather long, but it must be recalled that when the compressor is stalling severely, the number of stalled regions is quite irregular (the effects of the first kind of stall appear to be superimposed on the fluctuations of the flow rate due to the second kind of rotating stall).

Plate 2 concerns the five-region rotating stall state (first type of stall). Stalling is shown clearly in images 4 and 5, but comparison with the images of Plate 1 shows the stall to be less severe. The complete cycle is shown to last about 1/130 sec.—a duration which is in good agreement with the data of dynamic pressure measurements.

In both series of pictures there is some evidence of aerodynamic lag.

(5) Conclusions

Investigations have been made of the rotating stall flow pattern on a single-stage axial compressor by means of dynamic stagnation and static pressure measurements and of smoke surveys. Both techniques yield results which are in good agreement. Smoke surveys appear to be of great assistance in the explanation of the rotating stall mechanism. Three distinct types of rotating stall can occur, but application of the existing theories should be sought for the first type only.

Appendix

Principle of the Theoretical Computation of Rotating Stall Absolute Rotative Speed, After Fabri and Siestrunck

The calculations of references 10 and 11, which are performed in the case of a single row, can be extended to the case of a rotor row between two stationary rows.

The following assumptions are made which permit calculations to be performed: the blade rows are made up of an infinite number of blades, outside the stall zones the rotor cascade relative inlet flow angle remains equal to the zero lift angle, there is no through velocity inside the stalled zones, and the stall zones may be represented as wakes in the Helmoltz sense.

The disturbances at the rotor do not interact noticeably on the distributor at the onset of the first kind of rotating stall, (an assumption which is in agreement with the observations as described above in the present paper).

An expression for the ratio h/N is derived, from the above assumptions and from the compatibility conditions at the wakes boundaries throughout the rotor cascade, as

$$h/N = 1/2\,[(1 + \psi)/(1 - \varphi \tan \beta_1)]$$

with $$\psi = (p_\infty - p_0)\xi^2/(1/2)\,\rho u_0^2$$

being the local static pressure rise coefficient before stall, p_0 the stagnation pressure at the hub nose, φ the local flow coefficient before stall, and β_1 the rotor cascade relative inlet flow angle.

The above formula applied to the case of the compressor of the present paper, at dimensionless radius 0.8, yields $h/N = 0.72$, instead of 0.68, as derived from measurements for the propagation speed of the rotating stall of the first kind.

References

[1] Grant, Howard P., *Hot Wire Measurements of Stall Propagation and Pulsating Flow in an Axial Flow Inducer-Centrifugal Impeller System*, Pratt & Whitney Research Report No. 133, June, 1951.

[2] Iura, T., and Rannie, W. D., *Observations of Propagating Stall in Axial-Flow Compressors*, California Institute of Technology Mechanical Engineering Laboratory Report No. 4, April, 1953.

[3] Iura, T., and Rannie, W. D., *Experimental Investigation of Rotating Stall in Axial Compressors*, Trans. ASME, April, 1954.

[4] Emmons, H. W., Pearson, C. E., and Grant, H. P., *Compressor Surge and Stall Propagation*, Trans. ASME, Vol. 77, No. 4, pp. 455–467; Discussion, pp. 467–469, May, 1955.

[5] Huppert, Merle C., and Benser, William A., *Some Stall and Surge Phenomena in Axial-Flow Compressors*, Journal of the Aeronautical Sciences, Vol. 20, No. 12, pp. 835–845, December, 1953.

[6] Sears, W. R., *On Asymmetric Flow in an Axial-Flow Compressor Stage*, Journal of Applied Mechanics, Vol. 20, No. 1, pp. 57–62, March, 1953.

(*Continued on page 72*)

Aerodynamics of Nonuniform Flows as Related to an Airfoil Extending Through a Circular Jet*

SCOTT RETHORST**

California Institute of Technology

SUMMARY

A method has been derived for the determination of the downwash in the field of an airfoil extending through a circular jet. This solution for values of downwash was then employed in lifting surface theory to determine the lift distribution on a wing extending through a circular jet.

The basic approach for the downwash solution was to consider the flow resulting from the viscous action of the vortex sheet constituting the jet boundary. The method of solution is essentially based on a division of the flow thus induced by this jet boundary into parts which are even and odd with respect to the direction of flow. The analysis due to the even part alone is similar to previous theories, which in effect disregarded the odd part. Such previous results for the lift distribution based on the even part alone differ considerably from the experimental values. The results based on the total of the even and odd parts show good agreement with the experiments, illustrating the necessity of including the odd part of the flow when the segment of the wing immersed in the jet is of low aspect ratio.

The problem has been solved in parametric form, so that the results may be employed to determine the characteristics of any geometry wing-jet combination at any jet velocity ratio.

SYMBOLS

r_o	= jet radius
x, y, z	= rectangular coordinates (Fig. 1)
ξ, η, ζ	= nondimensionalized rectangular coordinates, x/r_o, $y/r_o, z/r_o$
$\bar{x}, \bar{y}, \bar{z}$	= rectangular coordinate running variables
α, β, γ	= nondimensionalized rectangular coordinate running variables, $\bar{x}/r_o, \bar{y}/r_o, \bar{z}/r_o$
x, r, θ	= cylindrical coordinates
ρ	= nondimensionalized radius, r/r_o
s	= semiwidth of horseshoe vortex
b	= wing span
S	= wing area
$\boldsymbol{A}$	= vector velocity potential of flow induced by horseshoe vortex
ϕ	= scalar velocity potential of flow induced by jet boundary
V_j	= jet velocity
V_o	= outer or free-stream velocity
μ	= V_o/V_j
Γ	= circulation strength
$\boldsymbol{v}$	= vector perturbation velocity
u, v, w	= rectangular perturbation velocities
u_r	= radial perturbation velocity
I, K	= modified Bessel functions
A, B	= coefficients in series representation of ϕ
p	= summation index
λ	= variable of integration
c, d	= spanwise locations of horseshoe vortices, nondimensionalized with respect to jet radius r_o
h	= perpendicular distance to a line vortex
R'	= three-dimensional nondimensionalized potential distance = $\sqrt{\xi^2 + (\eta - \beta)^2 + \zeta^2}$
R	= two-dimensional nondimensionalized potential distance = $\sqrt{(\eta - \beta)^2 + \zeta^2}$
n	= number designating a particular horseshoe vortex, starting from left wing tip
ν	= number designating a particular downwash point, starting from left wing tip
$d\boldsymbol{l}$	= differential length element of horseshoe vortex, nondimensionalized with respect to jet radius r_o
P_ν	= downwash points
Q_ν	= vortex points
N	= number of horseshoe vortices across total wing span
$F(\bar{x}, \bar{y})$	= downwash velocity at any point $(\bar{x}, \bar{y})$ caused by a rectangular horseshoe vortex of unit semiwidth and circulation strength equal to 4π
$F_{\nu n}$	= wing downwash coefficient; the downwash at any downwash point P_ν due to the nth horseshoe vortex
$G(\xi, \eta)$	= downwash velocity at any point (ξ, η) caused by the jet boundary reaction to a rectangular horseshoe vortex of unit semiwidth and circulation strength equal to 4π
$G_{\nu n}$	= jet boundary downwash coefficient; the downwash caused by the jet boundary at any point P_ν due to the nth horseshoe vortex
p, q	= coordinates of a point on the wing surface with respect to root quarter chord, based on semiwidth of horseshoe vortex
$\bar{x}, \bar{y}$	= coordinates of a point in the wing surface with respect to the origin of a unit horseshoe vortex, based on semiwidth of horseshoe vortex
W	= Wronskian of Bessel functions = $I(\lambda)K'(\lambda) - I'(\lambda)K(\lambda) = -(1/\lambda)$
$\bar{W}$	= modified Wronskian = $V_o^2 I'(\lambda)K(\lambda) - V_j^2 I(\lambda)K'(\lambda)$ Note: $\lim_{V_o \to V_j} \bar{W} = +(1/\lambda)V_j^2$

Received June 10, 1957.

* This paper is a condensation of the author's Ph.D. thesis at the California Institute of Technology.[1] A nonmathematical report on this work[2] was presented at the Low-Speed Flight Session, National Summer Meeting, IAS, Los Angeles, June 18–21, 1956. This research is being extended under contract by the Office of Naval Research.

The author wishes to acknowledge the guidance of Dr. Homer J. Stewart, as well as the encouragement of Dr. Clark B. Millikan and Dr. Morgan Ward, in carrying out this research. The author is also indebted to Dr. Richard Talmadge of the Lockheed Aircraft Corporation for programing and performing the numerical computations by electronic data processing equipment.

** Now, Consultant, and President, Vehicle Research Corporation, Pasadena, Calif.

INTRODUCTION

THE AERODYNAMICS of an airfoil in a uniform flow field is a highly developed subject. If the flow

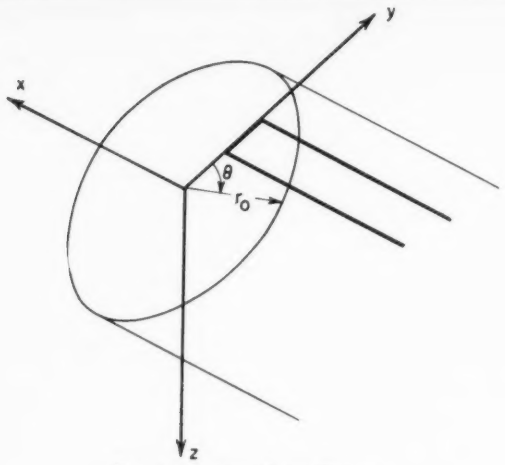

FIG. 1. System of coordinates.

field is nonuniform, the subject becomes much more complex. A general attack on this nonuniform flow problem was made by von Kármán and Tsien in 1945.[3] The method developed was subsequently utilized by Fejer for the case of a flow whose velocity varied linearly in the spanwise direction.[4]

Many examples of nonuniform flow arise in fluid mechanics, which would benefit from recognition and treatment as special cases of this branch of aerodynamics. Among these are vectored slipstream, jet flap, Coanda effect, supercirculation, thrust augmentation, and shrouded propellers.

In general, the areas of endeavor which have stimulated interest in the aerodynamics of nonuniform flow fall into one of two categories. First, there are the many arrangements such as those listed above which involve the behavior of airfoils immersed in or adjacent to flows of finite extent generated by and external to power plants. Second, such flow conditions are encountered within certain power plants, providing, for example, the environment of nonuniform flow in which the blades of turbomachinery operate.

This paper is concerned primarily with the first of these areas of endeavor. Since the power plants which are used to generate these flows of finite extent most often involve rotating machinery, this paper specifically treats a jet which is circular.

The problem of determining the characteristics of an airfoil extending through a circular jet has itself been investigated from several points of view. One is the influence of a propeller slipstream on an airplane's flight characteristics. Another is the influence of the boundaries of a wind tunnel on an airfoil being tested therein.

An analytical treatment of the problem of a wing in a propeller slipstream was given by Koning,[5] based on lifting line theory. The results of Koning's analysis, because of his method of computation, are valid only for small increments of the jet velocity. Other early estimates[6–8] were based on semiempirical factors, and gave satisfactory results within the speed-power range for which they were developed. However, the higher ratios of jet velocities attainable through turboprop engines have stimulated renewed interest in solutions valid at all jet velocities. This interest is further augmented by the development of certain types of vertical take-off aircraft, and other configurations where the higher jet velocities now attainable produce the dominant effect on performance.

Graham, Lagerstrom, Licher, and Beane[9] recently surveyed the slipstream problem, and extended Koning's results in a form valid (within the original assumptions) at all jet velocities. Graham's study also included an application of slender body theory to this problem. These two theories were compared with the experimental data of Stuper,[10] which seemed to lie between the two theories.

In most cases of interest the width of a propeller slipstream is of the same order as the wing chord immersed in it. With the aspect ratio of the immersed segment thus of the order of one, it would seem lifting surface theory would be required to properly describe the actual conditions. The finding of Graham that the available experimental data lay midway between the two limiting theories, lifting line and slender body, would appear to support this view.

The difficulty in applying lifting surface theory to this problem is the determination of the downwash due to the boundary of the jet at points downstream of the lifting line. However, the downwash aft of the lifting line is of interest in certain wind-tunnel problems, and has been determined by Lotz[11] and Burgers.[12] These wind-tunnel investigations were situations where the outer velocity was zero and the airfoil lay entirely within the jet, and as such were special cases of the general problem of an airfoil extending through a circular jet. A similar investigation for a closed wind tunnel was carried out by Eisenstadt.[13]

This paper develops the general case where there exists an outer velocity and where the airfoil extends through the jet. This permits the calculation of the downwash due to the boundary in the entire field aft of the lifting line. Any wing problem in principle can then be solved by lifting surface methods.

As an example, the wing problem investigated experimentally by Stuper[10] is solved by finite step methods,[14] based on the approximate lifting surface method of Weissinger.[15]

The solution presented in this paper has necessarily employed certain idealizations of flows occurring in practice in order to make the problem amenable to analytical treatment. This fact, discussed in detail by the writer elsewhere,[2] should be kept in mind in applying the results of this paper in design.

Analysis of Downwash Due to the Jet Boundary

The problem, as illustrated in Fig. 2, is an airfoil spanning a circular jet. This circular jet of velocity V_j is bounded by an infinite outer flow of velocity V_o. The finite wing extends symmetrically completely across the jet into the outer flow on both sides.

In the analysis, expressions will be developed for downwash due to the jet boundary reaction to infinitesimal vortex elements, which may be integrated to give the contributions of finite vortices. The airfoil itself will then be replaced by a series of such finite horseshoe vortices. The case for such a vortex inside or outside of the jet will then be solved separately. These horseshoe vortices, illustrated in Fig. 3, will be represented in width parametrically, so that combinations may later be superimposed to represent any arbitrary jet-wing combination. The circulation around the horseshoe vortex as illustrated is taken as positive.

The fluid is assumed to be an ideal, incompressible, nonviscous fluid, and this leads to the Laplace equation as the governing equation.

The boundary of the jet is a free surface. The presence of different velocities on its two sides gives rise to a vortex sheet on the boundary. This vortex sheet has associated with it a flow system such that the required conditions on pressure and continuity of the boundary are satisfied.

Thus the requirements of the jet boundary determine the flow, aside from the singularities represented by the wing and its wake. Two conditions must be satisfied on the boundary in a linearized small perturbation theory. First, the pressure of the inside flow (region j) must at the boundary equal the pressure of the outside flow (region o). Otherwise, the acceleration of the fluid would be infinite across the boundary. In terms of the perturbation velocity, $\boldsymbol{v}$, whose axial and radial components are u and u_r, respectively, this condition is written

$$V_j u_j = V_o u_o \tag{1}$$

The second boundary condition is one of continuity, and states that the boundary must consist of streamlines—that is, the inside and outside flow must be tangent at the boundary. For a circular jet, this tangency condition is expressed as

$$V_o u_{r_j} = V_j u_{r_o} \tag{2}$$

The perturbation flow $\boldsymbol{v}$ is composed of two parts, that due to the wing and that due to the boundary. The flow due to the wing, or due to the system of horse-

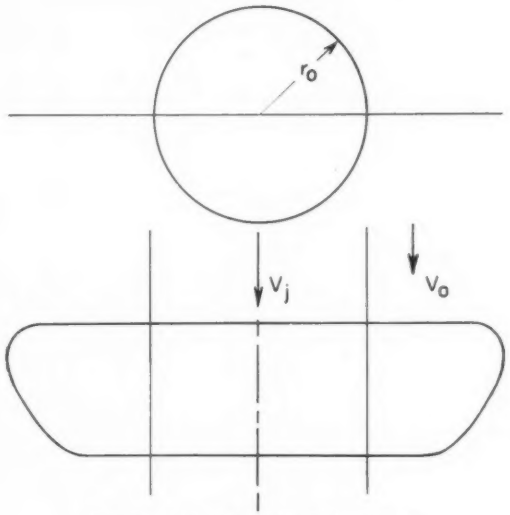

FIG. 2. Airfoil spanning a circular jet.

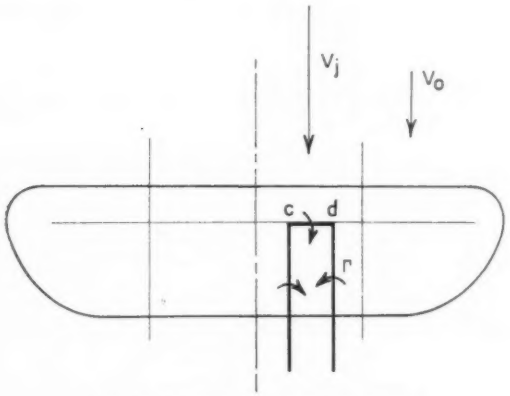

FIG. 3. Elementary horseshoe vortex.

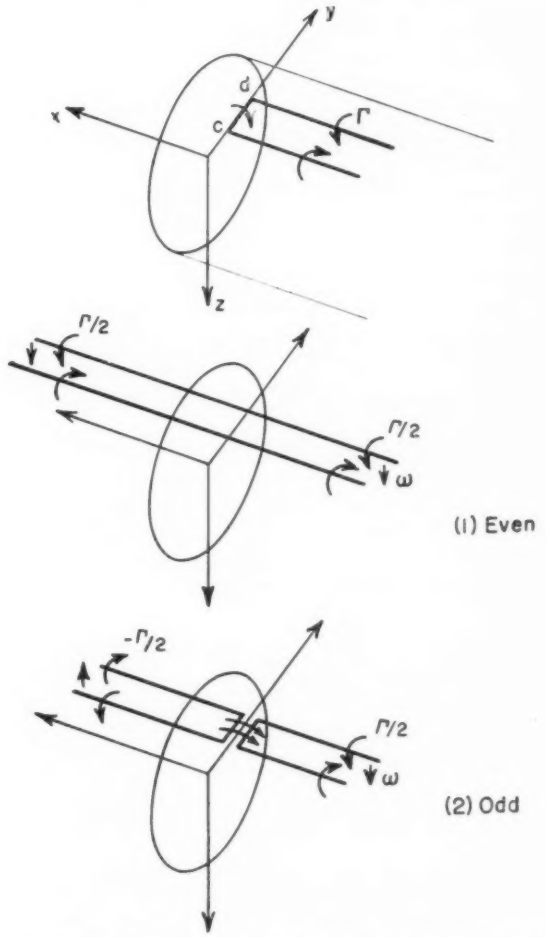

FIG. 4. Even and odd parts of elementary horseshoe vortex inside jet.

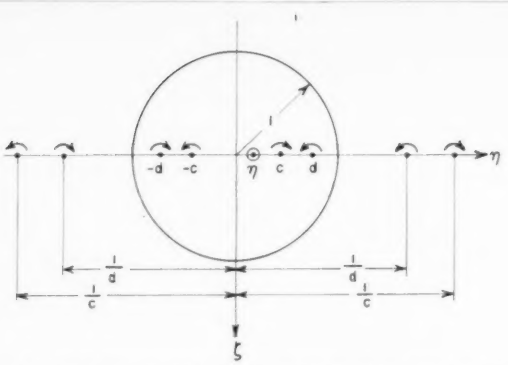

FIG. 5. Two-dimensional vortex system of a pair of symmetrically spaced horseshoe vortices inside jet.

shoe vortices used to represent it, is known, and may be readily determined by the Biot Savart law. The essential problem then is to determine the unknown flow due to the jet boundary. The sum of the two flows then constitutes the total perturbation flow.

We note the single elementary horseshoe vortex of strength Γ may be decomposed into two halves, one even (1) and one odd (2), each of strength $\Gamma/2$, as illustrated in Fig. 4. These two systems are independent, and satisfy the boundary conditions independently.

This decomposition of the vortex into its even and odd parts with respect to x will facilitate the solution of the problem, as the even part is two-dimensional, and may be readily solved by two-dimensional potential theory. The solution of the odd part, while more complicated, may be facilitated by employing antisymmetry conditions.

Horseshoe Vortex Inside Jet

The elementary horseshoe vortex inside the jet is first decomposed into its even and odd parts. Each of these halves satisfies the boundary conditions separately, so we may adopt whatever method of solution is most feasible for each case.

Even System—The even system, as illustrated in Fig. 4, is two-dimensional. This plane flow may then be solved most simply by two-dimensional potential theory. In terms of our boundary conditions, the condition (1) has vanished with the x component of the perturbation velocity. However, the radial boundary condition (2) still applies.

This requirement, for the case of a vortex located inside the jet, may be met by an image system consisting of vortices located outside the jet at the inverse points, as shown in Fig. 5.

It has been shown (see reference 5, p. 391) that, when a real vortex is located inside a jet, the contribution to the motion inside the jet due to the boundary is that represented by this fictitious image system outside the boundary, modified in intensity by the factor $+[(V_j^2 - V_o^2)/(V_j^2 + V_o^2)]$. Thus when the outer velocity V_o is zero, the image strength is undiminished. As V_o approaches V_j, the image strength vanishes with the boundary.

Also, the contribution of the boundary to the motion outside the jet, due to a real vortex located inside the jet, in the presence of a boundary, is that of the real vortex itself, modified in intensity by the factor $-[(V_j - V_o)^2/(V_j^2 + V_o^2)]$. When the outer velocity V_o is zero, this boundary contribution is undiminished, and completely cancels the real vortex inside. As the outer velocity V_o approaches V_j, the boundary vanishes, and the effect of the real vortex inside is undiminished.

Effect inside jet: For a real horseshoe vortex of strength Γ lying in the plane $z = 0$, of small but finite span extending between two parametric nondimensionalized points c and d, the even part consists of two line vortices of strength $\Gamma/2$ extending to $\pm\infty$ through these points. The image line vortices then extend through the inverse points of c and d—namely, $1/c$ and $1/d$, respectively.

Since the image system replaces the boundary, the downwash due to the boundary, for the even system, may be obtained as the downwash due to the image system. This may be obtained by a straightforward application of the Biot Savart law.

For two line vortices through points c and d, as illustrated in Fig. 5, the downwash induced at any point in the jet η, in the plane of the vortex due to the image vortices, may be found as follows.

For a doubly infinite vortex of strength $\Gamma/2$ the induced downwash is

$$w(\eta) = (\Gamma/2)/2\pi h$$

where h is the perpendicular distance from the point η to the vortex. Hence, for the image pair located at the inverse points of c and d, where the first subscript on $w(\eta)$ refers to the location of the effect point; the second to the location of the real vortex,

$$w_{jj}(\eta) = \frac{\Gamma}{4\pi r_o}\left[\frac{1}{(1/d) - \eta} - \frac{1}{(1/c) - \eta}\right]$$

and for the image pair located at the inverse points of $-c$ and $-d$,

$$w_{jj}(\eta) = \frac{\Gamma}{4\pi r_o}\left[\frac{1}{(1/d) + \eta} - \frac{1}{(1/c) + \eta}\right]$$

Hence, for a pair of finite horseshoe vortices, symmetrically spaced with respect to the axis of the jet, the downwash due to the image of the even part, induced at a point η inside the jet, taking into account the image strength factor, is

$$w_{jj}(\eta) = \frac{V_j^2 - V_o^2}{V_j^2 + V_o^2}\frac{\Gamma}{4\pi r_o} \times \left[\frac{1}{(1/d) - \eta} - \frac{1}{(1/c) - \eta} + \frac{1}{(1/d) + \eta} - \frac{1}{(1/c) + \eta}\right] \tag{3}$$

Effect outside jet: Here the downwash induced at a point η outside the jet by the boundary due to a pair of real line vortices of strength $\Gamma/2$ extending to $\pm\infty$ through points c and d is

$$w_{oj}(\eta) = (\Gamma/4\pi r_o)\{[1/(\eta - c)] - [1/(\eta - d)]\}$$

and that induced by the vortex pair at $-c$ and $-d$ is

$$w_{oj}(\eta) = (\Gamma/4\pi r_o)\{[1/(\eta + d)] - [1/(\eta + c)]\}$$

Hence for a pair of finite horseshoe vortices, symmetrically spaced with respect to the axis of the jet, the downwash induced by the boundary, due to the even part, at a point η outside the jet, taking into account the image strength factor, is

$$w_{oj}(\eta) = -[(V_j - V_o)^2/(V_j^2 + V_o^2)](\Gamma/4\pi r_o) \times \{[1/(\eta - c)] - [1/(\eta - d)] + [1/(\eta + d)] - [1/(\eta + c)]\} \quad (4)$$

Odd System—An elementary horseshoe vortex inside the jet will induce a velocity perturbation, the vector potential of which in a uniform flow we represent by $\boldsymbol{A}$. In addition, the requirements of the boundary induce a further flow, the potential of which we represent by ϕ.

The total perturbation velocity $\boldsymbol{v}$ for the odd system (2) of Fig. 4 is thus the sum

$$\boldsymbol{v} = \nabla \times \boldsymbol{A} + \nabla\phi \quad (5)$$

The part of the perturbation velocity due to the horseshoe vortex itself, $\boldsymbol{v_A}$, represented by the vector potential $\boldsymbol{A}$, is known. The part due to the boundary, $\boldsymbol{v_\phi}$, represented by the potential ϕ, is unknown. However, the total perturbation velocity $\boldsymbol{v}$ must satisfy the boundary conditions (1) and (2). Hence we may use these boundary conditions to find the unknown potential ϕ, and from this potential ϕ we may then find the boundary induced downwash for the odd system.

We may represent the potential ϕ conveniently by a series of the form for $\rho < 1$

$$\phi_j = \frac{2\Gamma}{\pi^2}\sum_{p=0}^{\infty}\sin(2p+1)\theta \times \int_0^\infty A_{2p+1}(\lambda) I_{2p+1}(\lambda\rho)\sin\xi\lambda\, d\lambda \quad (6)$$

and for $\rho > 1$

$$\phi_o = \frac{2\Gamma}{\pi^2}\sum_{p=0}^{\infty}\sin(2p+1)\theta \times \int_0^\infty B_{2p+1}(\lambda) K_{2p+1}(\lambda\rho)\sin\xi\lambda d\lambda \quad (7)$$

The potential ϕ is antisymmetric with respect to the xy plane, since the downwash $w = \partial\phi/\partial z$ is symmetric with respect to this plane. Hence for the potential we use only a sine θ series. Also we use only the odd θ terms as the even θ terms are antisymmetric with regard to the z plane, whereas the flow is symmetric about this plane.

Also from Fig. 4, the downwash w in the odd system (2) is seen to be odd with respect to x. Hence ϕ is also odd in x. We may thus represent ϕ by a sine series in x, or in ξ in nondimensionalized form.

With this form of the potential ϕ established, we must find the unknown coefficients $A(\lambda)$ and $B(\lambda)$, employing the known velocity due to the vector potential $\boldsymbol{A}$ of the horseshoe vortex itself.

The relation between the vector potential $\boldsymbol{A}$ and its resulting velocity field $\boldsymbol{v_A}$ is

$$\boldsymbol{v_A} = \nabla \times \boldsymbol{A} = \begin{vmatrix} \boldsymbol{i} & \boldsymbol{j} & \boldsymbol{k} \\ \partial/\partial x & \partial/\partial y & \partial/\partial z \\ A_x & A_y & A_z \end{vmatrix} \quad (8)$$

where A_x, A_y, A_z are the rectangular components of the vector potential $\boldsymbol{A}$. For a rectangular horseshoe vortex lying in the plane $z = 0$ as illustrated in Fig. 4, the potential of the bound vortex is A_y and the potential of the trailing vortex is A_x.

For the bound vortex $A_x = A_z = 0$, and

$$u_{A_{bd}} = \boldsymbol{i}\cdot\boldsymbol{v_A} = -(\partial A_y/\partial z) = -(\partial A_y/\partial r)(\partial r/\partial z) - (\partial A_y/\partial\theta)(\partial\theta/\partial z)$$

or

$$u_A = -(\sin\theta/r_o)(\partial A_y/\partial\rho) - (\cos\theta/r_o\rho)(\partial A_y/\partial\theta) \quad (9)$$

which we write as the total u perturbation due to the vector potential $\boldsymbol{A}$, since the trailing vortex does not contribute to this axial velocity component. Similarly,

$$v_{A_{bd}} = \boldsymbol{j}\cdot\boldsymbol{v_A} = 0$$

and

$$w_{A_{bd}} = \boldsymbol{k}\cdot\boldsymbol{v_A} = \partial A_y/\partial x$$

so

$$u_{r_{A_{bd}}} = w\sin\theta = (\sin\theta/r_o)(\partial A_y/\partial\xi) \quad (10)$$

The radial perturbation velocity component u_{r_A} will also have a contribution from the trailing vortex, for which $A_y = A_z = 0$.
For this case,

$$u_{A_{tr}} = \boldsymbol{i}\cdot\boldsymbol{v_A} = 0$$

$$v_{A_{tr}} = \boldsymbol{j}\cdot\boldsymbol{v_A} = \partial A_x/\partial z = \sin\theta(\partial A_x/\partial r) + (\cos\theta/r)(\partial A_x/\partial\theta)$$

$$w_{A_{tr}} = \boldsymbol{k}\cdot\boldsymbol{v_A} = -\partial A_x/\partial y = -\cos\theta(\partial A_x/\partial r) + (\sin\theta/r)(\partial A_x/\partial\theta)$$

But

$$u_{r_{A_{tr}}} = v\cos\theta + w\sin\theta$$

Hence,

$$u_{r_{A_{tr}}} = (1/r_o\rho)(\partial A_x/\partial\theta) \quad (11)$$

Now combining Eqs. (10) and (11) we have the total radial perturbation velocity due to the vector potential $\boldsymbol{A}$:

$$u_{r_A} = (\sin\theta/r_o)(\partial A_y/\partial\xi) + (1/r_o\rho)(\partial A_x/\partial\theta) \quad (12)$$

These expressions (9) and (12) give the axial and radial velocity perturbations due to the horseshoe vortex whose vector potential is $\boldsymbol{A}$, in terms of the A_y and A_x components of the potential, corresponding to the bound and trailing elements of the horseshoe vortex.

We now proceed to determine these required components of the vector potential.

Bound vortex elements: We consider an elementary horseshoe vortex of strength Γ lying in the plane $z = 0$, of small but finite span extending between two parametric nondimensionalized points c and d. The odd

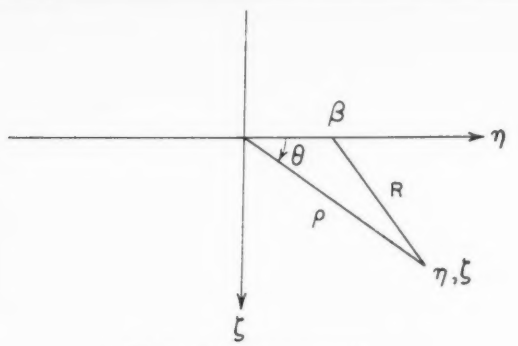

FIG. 6. Cosine law geometry.

part is then of strength $\Gamma/2$. However, as can be seen from Fig. 4, the bound vortex is of full strength Γ.

Now the flow due to a horseshoe vortex of strength Γ may be represented by the vector potential

$$\boldsymbol{A} = (\Gamma/4\pi) \int (d\boldsymbol{l}/R') \tag{13}$$

For a differential element of the bound vortex, $d\boldsymbol{l} = \boldsymbol{j}d\beta$, and $R' = \sqrt{\xi^2 + (\eta - \beta)^2 + \zeta^2}$, $A_x = A_z = 0$, and

$$dA_y = (\Gamma d\beta/4\pi)\,[1/\sqrt{\xi^2 + (\eta - \beta)^2 + \zeta^2}]$$

Now we may represent the reciprocal distance by (see reference 16, p. 75)

$$\frac{1}{R'} = \frac{1}{\sqrt{\xi^2 + (\eta - \beta)^2 + \zeta^2}} = \frac{2}{\pi}\int_0^\infty K_o\,[\lambda\sqrt{(\eta - \beta)^2 + \zeta^2}]\cos\xi\lambda d\lambda$$

Furthermore, from Fig. 6,

$$R = \sqrt{(\eta - \beta)^2 + \zeta^2} = \sqrt{\beta^2 + \rho^2 - 2\beta\rho\cos\theta}$$

Now applying Gegenbauer's addition theorem for $K_o(\lambda R)$ (see reference 16, p. 74, and reference 17, p. 44) for the case inside the jet, where $|\beta| < |\rho|$:

$$K_o(\lambda R) = I_o(\lambda\beta)K_o(\lambda\rho) + 2\sum_{p=1}^{\infty}\cos p\theta\, I_p(\lambda\beta)K_p(\lambda\rho) \tag{14}$$

For $|\rho| < |\beta|$, interchange ρ and β. Thus $|\beta/\rho| < 1$

$$1/R' = (2/\pi)\int_0^\infty I_o(\lambda\beta)K_o(\lambda\rho)\cos\xi\lambda d\lambda + \sum_{p=1}^{\infty}\cos p\theta\cdot(4/\pi)\int_0^\infty I_p(\lambda\beta)K_p(\lambda\rho)\cos\xi\lambda d\lambda$$

For a pair of horseshoe vortices symmetrically spaced with respect to the jet axis, each of span from c to d, the terms for odd p cancel and those for even p combine, so

$$A_y = \frac{\Gamma}{\pi^2}\left[\int_0^\infty\left\{\int_c^d I_o(\lambda\beta)d\beta\right\}K_o(\lambda\rho)\cos\xi\lambda d\lambda + 2\sum_{p=1}^{\infty}\cos 2p\theta\int_0^\infty\left\{\int_c^d I_{2p}(\lambda\beta)d\beta\right\}K_{2p}(\lambda\rho)\cos\xi\lambda d\lambda\right] \tag{15}$$

Trailing vortex elements: Having found A_y, we may determine A_x by noting that the divergence of the vector potential $\boldsymbol{A}$ is zero—i.e.,

$$\nabla\cdot\boldsymbol{A} = 0 \tag{16}$$

Since we are considering a vortex in the plane $z = 0$, $A_z = 0$. Hence, this divergence may be written

$$(\partial A_x/\partial x) + (\partial A_y/\partial y) = 0 \tag{17}$$

The expression obtained above Eq. (15) for A_y may be differentiated with respect to y, and the result integrated with respect to x, adding a constant of integration $f(\rho, \theta)$. The result obtained, after simplification through the use of recurrence relations for the trigonometric and Bessel functions, is

$$A_x = \frac{\Gamma}{\pi^2}\sum_{p=0}^{\infty}\cos(2p+1)\theta\int_0^\infty\left\{\int_c^d [I_{2p}(\lambda\beta) + I_{2p+2}(\lambda\beta)]d\beta\right\}K_{2p+1}(\lambda\rho)\sin\xi\lambda d\lambda \tag{18}$$

In this expression for A_x we have put $f(\rho, \theta) = 0$, since $f(\rho, \theta)$ is even in ξ, whereas A_x is odd in ξ, as seen from Eq. (13) and Fig. 4.

As a verification of this expression for A_x, it can be shown (see reference 1, p. 21) that the radial velocity obtained from it at $\xi = \pm\infty$ approaches the correct value independently obtained from the two-dimensional theory indicated by Fig. 7.

Application of boundary conditions: We now have expressions for A_y and A_x, which are known functions. We have series representations for the potentials ϕ of the flow due to the boundary, unknown to the extent of a coefficient in each of the two expressions. By employing the two boundary conditions (1) and (2), we may determine these two coefficients and hence determine the potentials ϕ for the flow due to the boundary in the two regions.

The first boundary condition which applies on the surface $\rho = 1$ is

$$V_j u_j = V_o u_o \tag{1}$$

which on employing Eq. (9) becomes

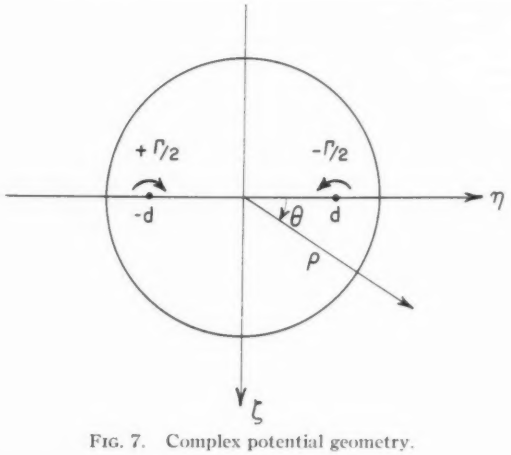

FIG. 7. Complex potential geometry.

$$-V_j[-(\sin\theta/r_o)\,(\partial.1_y/\partial\rho) - (\cos\theta/r_o\rho)\,(\partial.1_y/\partial\theta) + (\partial\phi/r_o\partial\xi)]_j = -V_o[-(\sin\theta/r_o)\,(\partial.1_y/\partial\rho) - (\cos\theta/r_o\rho)\,(\partial.1_y/\partial\theta) + (\partial\phi/r_o\partial\xi)]_o$$

Now, since the form of the vector potential depends only on the location of the real horseshoe vortex and not on the effect region, we may write

$$\{-V_j + V_o\}\,[-(\sin\theta/r_o)\,(\partial.1_y/\partial\rho) - (\cos\theta/r_o\rho)\,(\partial.1_y/\partial\theta)]_j - V_j[\partial\phi/r_o\partial\xi]_j = -V_o[\partial\phi/r_o\partial\xi]_o$$

On substituting the potentials from Eqs. (15), (6), and (7), and putting $\rho = 1$, we have

$$\{-V_j + V_o\}\left[-\frac{\sin\theta}{r_o}\frac{\Gamma}{\pi^2}\int_0^\infty\left\{\int_c^d I_o(\lambda\beta)d\beta\right\}\lambda K_o'(\lambda)\cos\xi\lambda d\lambda - \frac{\sin\theta}{r_o}\frac{\Gamma}{\pi^2}\times 2\sum_{p=1}^\infty\cos 2p\theta\int_0^\infty\left\{\int_c^d I_{2p}(\lambda\beta)d\beta\right\}\lambda K_{2p}'(\lambda)\cos\xi\lambda d\lambda + \frac{\cos\theta}{r_o}\frac{\Gamma}{\pi^2}\cdot 2\sum_{p=1}^\infty(2p)\sin 2p\theta\int_0^\infty\left\{\int_c^d I_{2p}(\lambda\beta)d\beta\right\}\times K_{2p}(\lambda)\cos\xi\lambda d\lambda\right] - V_j\left[\frac{1}{r_o}\frac{2\Gamma}{\pi^2}\sum_{p=0}^\infty\sin(2p+1)\theta\int_0^\infty A_{2p+1}(\lambda)I_{2p+1}(\lambda)\lambda\cos\xi\lambda d\lambda\right] = -V_o\left[\frac{1}{r_o}\frac{2\Gamma}{\pi^2}\sum_{p=0}^\infty\sin(2p+1)\theta\int_0^\infty B_{2p+1}(\lambda)K_{2p+1}(\lambda)\,\lambda\cos\xi\lambda d\lambda\right]$$

Now we divide through by $-(\Gamma/\pi^2 r_o)$, take the Fourier cosine transform with respect to ξ, and divide through by λ. In this expression and the following analysis, the omission of the argument of a Bessel function or the coefficients A and B means the argument is λ:

$$\{V_j - V_o\}\left[-\sin\theta\left\{\int_c^d I_o(\lambda\beta)d\beta\right\}K_o' - 2\sum_{p=1}^\infty\sin\theta\cos 2p\theta\left\{\int_c^d I_{2p}(\lambda\beta)d\beta\right\}K_{2p}' + 2\sum_{p=1}^\infty\cos\theta\sin 2p\theta\left\{\int_c^d I_{2p}(\lambda\beta)d\beta\right\}\frac{2p}{\lambda}K_{2p}\right] + V_j\left[2\sum_{p=0}^\infty\sin(2p+1)\theta.1_{2p+1}I_{2p+1}\right] = V_o\left[2\sum_{p=0}^\infty\sin(2p+1)\theta\,B_{2p+1}K_{2p+1}\right]$$

Recurrence relations among the trigonometric and Bessel functions simplify this expression to

$$\{V_j - V_o\}\frac{2}{\lambda}\sum_{p=0}^\infty(2p+1)\sin(2p+1)\theta K_{2p+1}\int_{c\lambda}^{d\lambda}\frac{I_{2p+1}(\lambda\beta)}{\lambda\beta}d(\lambda\beta) + 2V_j\sum_{p=0}^\infty\sin(2p+1)\theta.1_{2p+1}I_{2p+1} = 2V_o\sum_{p=0}^\infty\sin(2p+1)\theta B_{2p+1}K_{2p+1}$$

This equation must hold for all values of θ, hence we may equate coefficients of $\sin(2p+1)\theta$, where p runs from 0 to ∞. Also, since now all Bessel functions and the functions $.1$ and B are of order $2p+1$, we drop the subscript temporarily:

$$\{V_j - V_o\}\,(2\lambda)\,(2p+1)K\int_{c\lambda}^{d\lambda}[I(\lambda\beta)/\lambda\beta]d(\lambda\beta) + 2V_j.1I = 2V_oBK \tag{19}$$

The second boundary condition which applies on the surface $\rho = 1$ is

$$V_o u_{r_j} = V_j u_{r_o} \tag{2}$$

which on employing Eq. (12) becomes

$$-V_o[(\sin\theta/r_o)\,(\partial.1_y/\partial\xi) + (1/r_o\rho)\,(\partial.1_x/\partial\theta) + (\partial\phi/r_o\partial\rho)]_j = -V_j[(\sin\theta/r_o)\,(\partial.1_y/\partial\xi) + (1/r_o\rho)\,(\partial.1_x\,\partial\theta) + (\partial\phi/r_o\partial\rho)]_o$$

which, as before, may be written

$$\{-V_o + V_j\}\,[(\sin\theta/r_o)\,(\partial.1_y/\partial\xi) + (1/r_o\rho)\,(\partial.1_x/\partial\theta)]_j - V_o[\partial\phi/r_o\partial\rho]_j = -V_j[\partial\phi/r_o\partial\rho]_o$$

On substituting the potentials from Eqs. (15), (18), (6), and (7), and putting $\rho = 1$, we obtain an expression which may be simplified as before, in this case taking the Fourier sine transform with respect to ξ. Further simplification, as previously, yields a second equation for the unknown coefficients

$$\{V_o - V_j\}\,(2\lambda)\,(2p+1)K'\int_{c\lambda}^{d\lambda}[I(\lambda\beta)/\lambda\beta]\,d(\lambda\beta) + 2V_o.1I' = 2V_jBK' \tag{20}$$

Results: We now have two equations—(19) and (20)—which are solved for the two unknown coefficients $.1$ and B, using

$$W = \begin{vmatrix} I & K \\ I' & K' \end{vmatrix} = IK' - I'K = -(1/\lambda)$$

Substituting the values of A and B thus obtained in the expressions for the potentials, Eqs. (6) and (7), for the case of a horseshoe vortex inside a jet, where all Bessel functions are of the $2p + 1$ order,

$$\phi_{jj} = \frac{2\Gamma}{\pi^2} \sum_{p=0}^{\infty} (2p + 1) \sin (2p + 1)\theta \int_0^{\infty} \frac{\{V_j^2 - V_o^2\} KK'I(\lambda\rho)}{V_o^2 I'K - V_j^2 IK'} \frac{\sin \xi\lambda d\lambda}{\lambda} \int_{c\lambda}^{d\lambda} \frac{I(\lambda\beta)}{\lambda\beta} d(\lambda\beta) \quad (6a)$$

$$\phi_{oj} = \frac{2\Gamma}{\pi^2} \sum_{p=0}^{\infty} (2p + 1) \sin (2p + 1)\theta \int_0^{\infty} \left[\frac{V_o V_j}{\lambda} \frac{1}{V_o^2 I'K - V_j^2 IK'} - 1 \right] \frac{K(\lambda\rho) \sin \xi\lambda d\lambda}{\lambda} \int_{c\lambda}^{d\lambda} \frac{I(\lambda\beta)}{\lambda\beta} d(\lambda\beta) \quad (7a)$$

Horseshoe Vortex Outside Jet

The elementary horseshoe vortex outside the jet may be treated in a manner identical to the vortex inside.

Even System—As before, the even system, as illustrated in Fig. 8, is two-dimensional. A similar image system may be used, consisting of image vortices located inside the jet at the inverse points, as illustrated in Fig. 9.

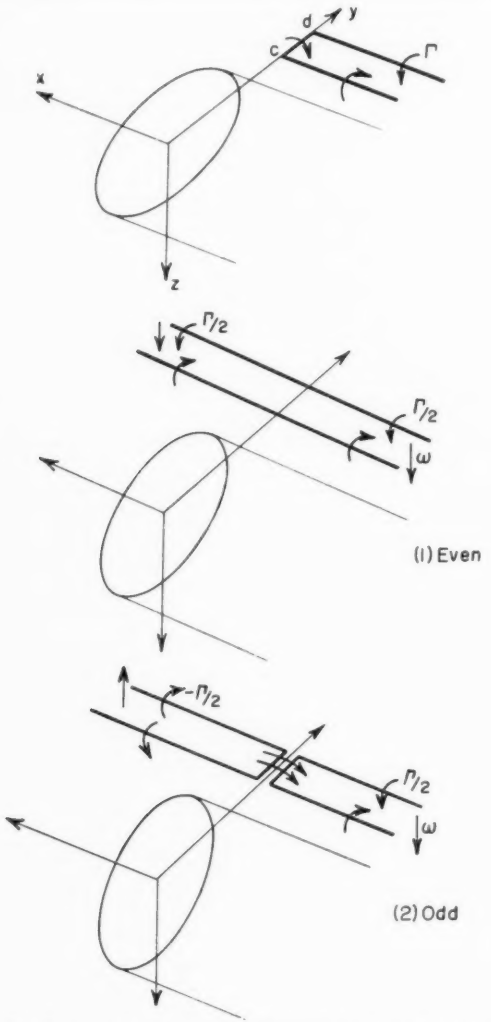

FIG. 8. Even and odd parts of elementary horseshoe vortex outside jet.

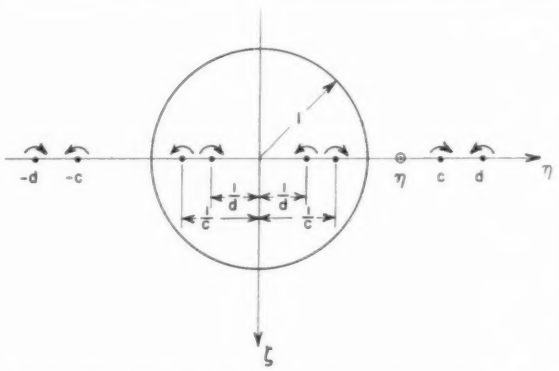

FIG. 9. Two-dimensional vortex system of a pair of symmetrically spaced horseshoe vortices outside jet.

For this case, when a real vortex is located outside the jet, it has been shown (see reference 5, p. 389) that the contribution to the motion outside the jet due to the boundary is that represented by the fictitious image system inside the boundary, modified in intensity by the factor $-[(V_j^2 - V_o^2)/(V_j^2 + V_o^2)]$. Thus when the outer velocity V_o is zero, the image strength is equal in magnitude and opposite in sign to the real vortex outside the jet. As V_o approaches V_j, the image strength vanishes with the boundary.

The contribution of the boundary to the motion inside the jet due to a real vortex located outside the jet, in the presence of a boundary, is that of the real vortex itself, modified in intensity by the factor $-[(V_j - V_o)^2/(V_j^2 + V_o^2)]$. When the outer velocity V_o is zero, this boundary contribution is undiminished, and completely cancels the real vortex outside. As V_o approaches V_j, the boundary vanishes, and the effect of the real vortex outside is undiminished.

Effect inside jet: The downwash induced at a point η inside the jet by the boundary due to a pair of real line vortices of strength $\Gamma/2$ extending to $\pm\infty$ through points c and d is

$$w_{jo}(\eta) = (\Gamma/4\pi r_o) \{[1/(d - \eta)] - [1/(c - \eta)]\}$$

and that induced by the vortex pair at $-c$ and $-d$ is

$$w_{jo}(\eta) = (\Gamma/4\pi r_o) \{[1/(d + \eta)] - [1/(c + \eta)]\}$$

Hence for a pair of finite horseshoe vortices symmetrically spaced with respect to the axis of the jet, the downwash induced by the boundary, due to the even part, at

a point η inside the jet, taking into account the image strength factor, is

$$w_{jo}(\eta) = -[(V_j - V_o)^2/(V_j^2 + V_o^2)]\,(\Gamma/4\pi r_o) \times \{[1/(d-\eta)] - [1/(c-\eta)] + [1/(d+\eta)] - [1/(c+\eta)]\} \quad (21)$$

Effect Outside Jet: For a pair of real line vortices extending to $\pm\infty$ through points c and d, the image line vortices will extend through the inverse points of c and d—namely, $1/c$ and $1/d$, respectively.

The downwash induced at a point η outside the jet due to the image vortex pair located at the inverse points of c and d is

$$w_{oo}(\eta) = (\Gamma/4\pi r_o)\{-1/[\eta - (1/d)] + 1/[\eta - (1/c)]\}$$

and for the image pair located at the inverse points of $-c$ and $-d$,

$$w_{oo}(\eta) = \frac{\Gamma}{4\pi r_o}\left[-\frac{1}{\eta + (1/c)} + \frac{1}{\eta + (1/d)}\right]$$

Hence for a pair of finite horseshoe vortices, symmetrically spaced with respect to the axis of the jet, the downwash due to the image of the even part, induced at a point η outside the jet, taking into account the image strength factor, is

$$w_{oo}(\eta) = -\frac{V_j^2 - V_o^2}{V_j^2 + V_o^2}\frac{\Gamma}{4\pi r_o}\left[-\frac{1}{\eta - (1/d)} + \frac{1}{\eta - (1/c)} - \frac{1}{\eta + (1/c)} + \frac{1}{\eta + (1/d)}\right] \quad (22)$$

Odd System—As before, we represent the total perturbation velocity $\boldsymbol{v}$ for the odd system (2) of Fig. 8 by the sum

$$\boldsymbol{v} = \nabla \times \boldsymbol{A} + \nabla\phi \quad (5)$$

The expressions for the known perturbation velocities due to the vector potential $\boldsymbol{A}$ are unchanged, as given in Eqs. (9) and (12).

Bound vortex elements: We consider the bound vortex as before, interchanging ρ and β in Gegenbauer's addition theorem in Eq. (14). Hence, for $|\beta| > |\rho|$,

$$K_o(\lambda R) = I_o(\lambda\rho)K_o(\lambda\beta) + 2\sum_{p=1}^{\infty}\cos p\theta\, I_p(\lambda\rho)K_p(\lambda\beta) \quad (14a)$$

Thus, for $|\beta/\rho| > 1$,

$$\frac{1}{R'} = \frac{2}{\pi}\int_0^\infty I_o(\lambda\rho)K_o(\lambda\beta)\cos\xi\lambda d\lambda + \sum_{p=1}^{\infty}\cos p\theta \cdot \frac{4}{\pi}\int_0^\infty I_p(\lambda\rho)K_p(\lambda\beta)\cos\xi\lambda d\lambda$$

For a pair of horseshoe vortices symmetrically spaced with respect to the jet axis, each of span from c to d, the terms for odd p cancel and those for even p combine, so

$$A_y = \frac{\Gamma}{\pi^2}\left[\int_0^\infty\left\{\int_c^d K_o(\lambda\beta)d\beta\right\} I_o(\lambda\rho)\cos\xi\lambda d\lambda + 2\sum_{p=1}^{\infty}\cos\xi 2p\theta\int_0^\infty\left\{\int_c^d K_{2p}(\lambda\beta)d\beta\right\} I_{2p}(\lambda\rho)\cos\xi\lambda d\lambda\right] \quad (23)$$

Trailing vortex elements: As before, we obtain A_x from A_y (see reference 1, p. 38), employing the divergence theorem (16) and (17). For the present case of the vortex outside of the jet, we use Eq. (23) for A_y. The result obtained is

$$A_x = -\frac{\Gamma}{\pi^2}\sum_{p=0}^{\infty}\cos(2p+1)\theta\int_0^\infty\left\{\int_c^d [K_{2p}(\lambda\beta) + K_{2p+2}(\lambda\beta)]d\beta\right\} I_{2p+1}(\lambda\rho)\sin\xi\lambda d\lambda \quad (24)$$

This expression has been similarly verified (see reference 1, p. 41) by showing that the radial velocity obtained from it at $\xi = \pm\infty$ approaches the correct two-dimensional value.

Application of boundary conditions: The procedure used above where the horseshoe vortex was inside the jet may now be repeated, using the new expressions for A_y and A_x for the present case of the vortex outside the jet (see reference 1, p. 44). The same boundary conditions (1) and (2) apply, as do the series representations (6) and (7) of the unknown potential ϕ of the boundary induced downwash.

Results: This procedure yields the following expressions for the potentials for the case of a horseshoe vortex outside a jet, where all Bessel functions are of the $2p+1$ order:

$$\phi_{jo} = \frac{2\Gamma}{\pi^2}\sum_{p=0}^{\infty}(2p+1)\sin(2p+1)\theta\int_0^\infty\left[\frac{V_oV_j}{\lambda}\frac{1}{V_o^2I'K - V_j^2IK'} - 1\right]\frac{I(\lambda\rho)\sin\xi\lambda d\lambda}{\lambda}\int_{c\lambda}^{d\lambda}\frac{K(\lambda\beta)}{\lambda\beta}d(\lambda\beta) \quad (6b)$$

$$\phi_{oo} = \frac{2\Gamma}{\pi^2}\sum_{p=0}^{\infty}(2p+1)\sin(2p+1)\theta\int_0^\infty\frac{\{V_j^2 - V_o^2\}II'K(\lambda\rho)}{V_o^2I'K - V_j^2IK'}\frac{\sin\xi\lambda d\lambda}{\lambda}\int_{c\lambda}^{d\lambda}\frac{K(\lambda\beta)}{\lambda\beta}d(\lambda\beta) \quad (7b)$$

Summary of Results

Even System—The previously derived expressions for the downwash induced by the boundary due to the even system are now collected for convenience, writing $V_o/V_j = \mu$, where $0 \le \mu \le 1$. The first index refers to the effect

region, and the second to the location of the horseshoe vortex.

Vortex inside jet

$$w_{jj_{even}}(\eta) = \frac{1-\mu^2}{1+\mu^2}\frac{\Gamma}{4\pi r_o}\left[\frac{1}{(1/d)-\eta} - \frac{1}{(1/c)-\eta} + \frac{1}{(1/d)+\eta} - \frac{1}{(1/c)+\eta}\right] \tag{3a}$$

$$w_{oj_{even}}(\eta) = -\frac{(1-\mu)^2}{1+\mu^2}\frac{\Gamma}{4\pi r_o}\left[\frac{1}{\eta-c} - \frac{1}{\eta-d} + \frac{1}{\eta+d} - \frac{1}{\eta+c}\right] \tag{4a}$$

Vortex outside jet

$$w_{jo_{even}}(\eta) = -\frac{(1-\mu)^2}{1+\mu^2}\frac{\Gamma}{4\pi r_o}\left[\frac{1}{d-\eta} - \frac{1}{c-\eta} + \frac{1}{d+\eta} - \frac{1}{c+\eta}\right] \tag{21a}$$

$$w_{oo_{even}}(\eta) = -\frac{1-\mu^2}{1+\mu^2}\frac{\Gamma}{4\pi r_o}\left[-\frac{1}{\eta-(1/d)} + \frac{1}{\eta-(1/c)} - \frac{1}{\eta+(1/c)} + \frac{1}{\eta+(1/d)}\right] \tag{22a}$$

Odd System—We may now similarly collect the four expressions for the potentials of the flow induced by the boundary due to the odd system. These are designated by ϕ_{vn}, where the first index refers to the location of the effect point, and the second to the location of the horseshoe vortex. All Bessel functions are of the $2p+1$ order, and are of argument λ unless otherwise shown.

Vortex inside jet

$$\phi_{jj} = \frac{2\Gamma}{\pi^2}\sum_{p=0}^{\infty}(2p+1)\sin(2p+1)\theta\int_0^{\infty}\frac{\{V_j^2 - V_o^2\}KK'I(\lambda\rho)}{|\bar{\Gamma}|}\frac{\sin\xi\lambda d\lambda}{\lambda}\int_{c\lambda}^{d\lambda}\frac{I(\lambda\beta)}{\lambda\beta}\,d(\lambda\beta) \tag{6a}$$

$$\phi_{oj} = \frac{2\Gamma}{\pi^2}\sum_{p=0}^{\infty}(2p+1)\sin(2p+1)\theta\int_0^{\infty}\left[\frac{V_oV_j}{\lambda|\bar{\Gamma}|} - 1\right]\frac{K(\lambda\rho)\sin\xi\lambda d\lambda}{\lambda}\int_{c\lambda}^{d\lambda}\frac{I(\lambda\beta)}{\lambda\beta}\,d(\lambda\beta) \tag{7a}$$

Vortex outside jet

$$\phi_{jo} = \frac{2\Gamma}{\pi^2}\sum_{p=0}^{\infty}(2p+1)\sin(2p+1)\theta\int_0^{\infty}\left[\frac{V_oV_j}{\lambda|\bar{\Gamma}|} - 1\right]\frac{I(\lambda\rho)\sin\xi\lambda d\lambda}{\lambda}\int_{c\lambda}^{d\lambda}\frac{K(\lambda\beta)}{\lambda\beta}\,d(\lambda\beta) \tag{6b}$$

$$\phi_{oo} = \frac{2\Gamma}{\pi^2}\sum_{p=0}^{\infty}(2p+1)\sin(2p+1)\theta\int_0^{\infty}\frac{\{V_j^2 - V_o^2\}II'K(\lambda\rho)}{|\bar{\Gamma}|}\frac{\sin\xi\lambda d\lambda}{\lambda}\int_{c\lambda}^{d\lambda}\frac{K(\lambda\beta)}{\lambda\beta}\,d(\lambda\beta) \tag{7b}$$

where

$$|\bar{\Gamma}_{2p+1}(\lambda) = V_o^2I'K - V_j^2IK' \tag{25}$$

The downwash due to the jet boundary, at points in the plane of the airfoil, may be obtained for each of the four potentials by taking the derivatives

$$w_{bdry} = (\partial\phi_{vn}/\partial z) = \pm(\partial\phi_{vn}/r\partial\theta)\begin{bmatrix}+ \text{ when } \theta = 0^\circ\\ - \text{ when } \theta = 180^\circ\end{bmatrix}$$

The derivative with respect to $r\partial\theta$ of the expression in front of the integrals of ϕ_{vn}, which includes the angular function in each case, is

$$(2\Gamma/\pi^2r)\sum_{p=0}^{\infty}(2p+1)^2\cos(2p+1)\theta$$

In the plane of the wing, which we have chosen as the xy plane, θ assumes only the values of 0 and π. For $\theta = 0$, where $\partial\phi/\partial z = +(\partial\phi/r\partial\theta)$, $\cos(2p+1)\theta = +1$ for all p, and this expression in front of the ϕ_{vn} integrals is positive. Similarly for $\theta = \pi$, where $\partial\phi/\partial z = -(\partial\phi/r\partial\theta)$, $\cos(2p+1)\theta = -1$ for all p, and this expression is again positive.

Hence in the plane of the wing, for all p, writing $r = r_o\rho$, and noting that in the plane of the wing $\rho = \eta$, the expression in front of the ϕ_{vn} integra's becomes

$$+(2\Gamma/\pi^2r_o\eta)\sum_{p=0}^{\infty}(2p+1)^2 \tag{26}$$

Employing this result, rearranging the integrand for convenience, and, as before, writing $V_o/V_j = \mu$, we obtain the downwash induced by the boundary due to the odd system:

Vortex inside jet

$$w_{jj_{odd}}(\xi,\eta) = \frac{2\Gamma}{\pi^2r_o\eta}\sum_{p=0}^{\infty}(2p+1)^2\int_0^{\infty}\frac{KK'I(\eta\lambda)}{[1/\lambda\{1/(1/\mu^2)-1\}] - IK'}\frac{\sin\xi\lambda d\lambda}{\lambda}\int_{c\lambda}^{d\lambda}\frac{I(\lambda\beta)}{\lambda\beta}\,d(\lambda\beta) \tag{6c}$$

$$w_{oj_{odd}}(\xi,\eta) = \frac{2\Gamma}{\pi^2r_o\eta}\sum_{p=0}^{\infty}(2p+1)^2\int_0^{\infty}\left[\frac{1}{\mu-\lambda\{1/(1/\mu)-\mu\}IK'} - 1\right]\frac{K(\eta\lambda)\sin\xi\lambda d\lambda}{\lambda}\int_{c\lambda}^{d\lambda}\frac{I(\lambda\beta)}{\lambda\beta}\,d(\lambda\beta) \tag{7c}$$

Vortex outside jet

$$w_{jo_{odd}}(\xi,\eta) = \frac{2\Gamma}{\pi^2r_o\eta}\sum_{p=0}^{\infty}(2p+1)^2\int_0^{\infty}\left[\frac{1}{\mu-\lambda\{1/(1/\mu)-\mu\}IK'} - 1\right]\frac{I(\eta\lambda)\sin\xi\lambda d\lambda}{\lambda}\int_{c\lambda}^{d\lambda}\frac{K(\lambda\beta)}{\lambda\beta}\,d(\lambda\beta) \tag{6d}$$

$$w_{\omega_{odd}}(\xi, \eta) = \frac{2\Gamma}{\pi^2 r_o \eta} \sum_{p=0}^{\infty} (2p+1)^2 \int_0^{\infty} \frac{II'K(\eta\lambda)}{[1/\lambda_1^1(1/\mu^2) - 1_1^1] - IK'} \frac{\sin \xi\lambda d\lambda}{\lambda} \int_{c\lambda}^{d\lambda} \frac{K(\lambda\beta)}{\lambda\beta} d(\lambda\beta) \tag{7d}$$

The four downwash expressions for the odd system may be investigated in the limit as the variable of integration $\lambda \rightarrow \infty$ by use of the asymptotic series for the Bessel functions.

It can be shown (see reference 1, p. 59) that for large λ the integral expression (6c) for w_{jj} will converge at least to the order $1/\lambda^3$ for the case where both the effect point η and the vortex point d are at the jet boundary. The integral will converge exponentially to a stronger degree as either the effect or vortex point is taken farther from the boundary.

The remaining three integrals may be investigated in the limit as $\lambda \rightarrow \infty$ in a similar manner, and in each case they may be shown to converge with the same rapidity.

Asymptotic Correlation of Downwash of Odd and Even Systems—Each of the four expressions for the downwash due to the odd system should in the limit as $\xi \rightarrow \infty$ approach the corresponding expression for the even system. It can be shown (see reference 1, p. 61) that each such integral in the limit does indeed demonstrate this behavior, thus verifying the expressions obtained for the odd system.

Application to an Arbitrary Wing Extending Through a Jet

We have determined a basis for finding the downwash at any point ξ, η in the plane of the wing due to the boundary reaction to a pair of finite horseshoe vortices, symmetrically spaced with respect to the axis of the jet. The total downwash at such a point due to such a pair of horseshoe vortices will then be the sum of this boundary induced downwash and the downwash due to the horseshoe vortices themselves.

The downwash due to a field of finite horseshoe vortices has been conveniently tabulated in several forms,[18, 19] and so facilitates the calculations of span loadings by finite step methods.[14] We will therefore compute the boundary induced downwash in a similar manner so that it may be conveniently combined with the referenced tables for the horseshoe vortices to calculate the span loading for an airfoil extending through a jet.

With the total perturbation downwash thus determined over the entire x-y plane, and in particular over the field aft of the lifting line, any wing problem in principle can be solved by lifting surface methods. As an example, we employ the approximate lifting surface method of Weissinger[15] as a convenient method of calculating the span loading.

The lifting surface method of Weissinger in effect takes into account the linear variation of downwash along the chord. For such a linear variation, the wing characteristics may be predicted exactly for infinite aspect ratio by satisfying the boundary condition on the wing surface at the 3/4 chord point. Such a linear variation of downwash is the case for both a flat plate airfoil and a parabolic arc airfoil, and hence would be expected to be a good approximation for most conventional airfoils.

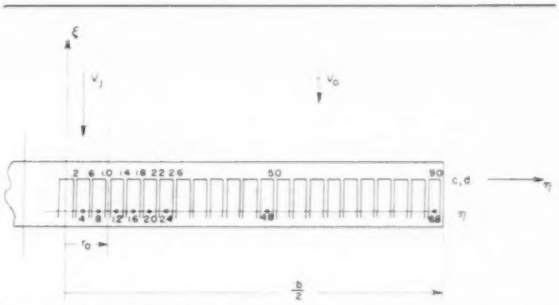

FIG. 10. Arrangement of wing-jet vortex pattern (with notation used to determine jet boundary downwash coefficients).

The lifting line approximation assumes no variation of downwash along the chord. Thus the Weissinger lifting surface theory, in taking into account the linear variation of downwash along the chord, is in effect considering the next term in a Taylor's expansion of downwash around the 1/4 chord. If further accuracy were required, say for a more complex cambered airfoil, a second term representing the curvature of the downwash could be employed.

In references 14 and 19 the wing span is subdivided into a finite number of horseshoe vortices, the spans of which are nondimensionalized with respect to the wing span. For the jet problem, it is more convenient to nondimensionalize the lengths with respect to the jet radius. The wing data and the jet data may thus be conveniently combined when the wing span is an integer multiple of the jet radius; for noninteger multiples the method may be adjusted at the wing tips to provide suitable data there.

To provide a general and flexible method useful for an arbitrary jet-span combination, we arrange the wing as illustrated in Fig. 10 (see also reference 14, Fig. 1, and reference 19, Fig. 6). The wing is replaced by a system of N horseshoe vortices along the quarter-chord line, the spans of which are so chosen that their semispan s is one-fifth of the jet radius r_o. Thus five such horseshoe vortices are located inside the jet.

Sufficient additional horseshoe vortices of the same semispan s are placed outside the jet to completely represent the wing span. Thus any arbitrary ratio of jet diameter to wing span arrangement may be represented, simply by employing a sufficient (odd) number of horseshoe vortices to represent the wing span. Reference 14 includes smaller span vortices at the tips which may be used if a further refinement in accuracy is required.

An equal number of downwash points is taken along the three-quarter chord line, at the midpoint of each elementary horseshoe vortex. The downwash velocity

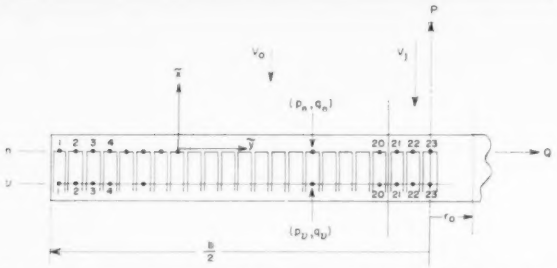

FIG. 11. Arrangement of wing-jet vortex pattern (with notation used to determine lift distribution).

from the total vortex system and the boundary is then equated to the component of local velocity normal to the wing chord at each such downwash point. Application of this tangent flow boundary condition for a symmetrical loading provides a set of $(N + 1)/2$ simultaneous equations in the $(N + 1)/2$ unknown circulation strengths across the span, since the circulation strengths of symmetrical vortex pairs will be identical. Solution of this set of equations provides the span loading.

If the ratio of wing span to the jet diameter is so large as to produce an unwieldy number of simultaneous equations, the number of horseshoe vortex pairs and hence the number of equations may be reduced by employing larger horseshoe vortex spans outboard where their effect on the jet boundary is less pronounced.

Downwash Due to the Wing

The downwash velocity in the plane of a rectangular horseshoe vortex due to the vortex itself is given by the expression

$$w(\bar{x}, \bar{y}) = (\Gamma/4\pi)\ [F(\bar{x}, \bar{y})/s] \tag{27}$$

where F is defined in reference 14, and the $\bar{x}$ and $\bar{y}$ are expressed in horseshoe semispans. The values of $F(\bar{x}, \bar{y})$ are conveniently tabulated in references 18 and 19.

Distributing an odd number N of horseshoe vortices having N downwash points across the wing span (Fig. 10), the downwash velocity at any of the downwash points P_ν resulting from the N horseshoe vortices is

$$w(\bar{x}_\nu, \bar{y}_\nu) = (1/4\pi) \sum_{n=1}^{N} (\Gamma_n/s) F(\bar{x}_\nu, \bar{y}_\nu) \tag{28}$$

where

$$\left.\begin{aligned} \bar{x}_\nu &= p_\nu - p_n \\ \bar{y}_\nu &= q_\nu - q_n \end{aligned}\right\} \tag{29}$$

and the $\bar{x}$, $\bar{y}$, p, q notation, and the ν, n subscript notation, as used in this section, is illustrated in Fig. 11. The ν and n are the effect and vortex points, respectively, counted from the left wing tip.

Since $b/2 = Ns$, we may write (30)

$$w(\bar{x}_\nu, \bar{y}_\nu) = (N/4\pi) \sum_{n=1}^{N} [\Gamma_n/(b/2)] F(\bar{x}_\nu, \bar{y}_\nu) \tag{31}$$

For cases of symmetrical loading and geometry, the downwash at any of the downwash points P_ν becomes

$$w(\bar{x}_\nu, \bar{y}_\nu) = \frac{N}{4\pi} \sum_{n=1}^{(N+1)/2}{}' \frac{\Gamma_n}{b/2} F_{\nu n} \tag{32}$$

with the coefficient $F_{\nu n}$ being given in terms of geometrical distances measured in horseshoe semispans,

$$F_{\nu n} = F[(p_\nu - p_n), (q_\nu - q_n)] + F[(p_\nu - p_n), (q_\nu + q_n)] \tag{33}$$

and the prime on the summation sign indicating that for the $(N + 1)/2$ term, representing the single horseshoe vortex at the center of the wing,

$$F_{\nu[(N+1)/2]} = F[(p_\nu - p_n), (q_\nu - 0)] \tag{34}$$

This condition may be applied at each downwash point to provide a set of $[(N + 1)/2]$ simultaneous equations in the $[(N + 1)/2]$ unknown circulation strengths from Eq. (32):

$$\left[w(\bar{x}_\nu, \bar{y}_\nu) = \frac{N}{4\pi} \sum_{n=1}^{(N+1)/2}{}' \frac{\Gamma_n}{b/2} F_{\nu n} \right]_{\nu = 1, 2, 3 \ldots [(N+1)/2]} \tag{35}$$

Downwash Due to the Jet Boundary

The expressions for the downwash due to the boundary have been obtained as follows, where the first subscript refers to the location of the effect region, the second to the location of the real vortex, and the even or odd notation refers to the component of the horseshoe vortex:

Even System		Odd System	
Expression	Eq. No.	Expression	Eq. No.
w_{jj}	(3a)	w_{jj}	(6c)
w_{oj}	(4a)	w_{oj}	(7c)
w_{jo}	(21a)	w_{jo}	(6d)
w_{oo}	(22a)	w_{oo}	(7d)

These expressions are all nondimensionalized with respect to the jet radius r_o. We may combine this boundary downwash with the horseshoe downwash at any particular point, taking note of the different coordinates of the same point in the two systems, due to their being nondimensionalized on different lengths, and having different origins.

Furthermore, by employing the relation

$$r_o = 5s \tag{36}$$

we may write the boundary downwash expressions in a form where they may be conveniently combined with wing downwash expressions—i.e.,

$$w(\xi, \eta) = (\Gamma/4\pi)\ [G(\xi, \eta)/s] \tag{37}$$

where we write the $G(\xi, \eta)$ as a function of ξ, η to emphasize their being nondimensionalized with respect to the jet radius r_o. By this relationship we define the jet boundary downwash coefficient $G_{\nu n}(\xi, \eta)$ as

$$G_{\nu n}(\xi, \eta) = (4\pi s/\Gamma)\ w_{\nu n}(\xi, \eta) \tag{38}$$

The quantities $G_{\nu n}$ may thus be written in terms of the boundary induced downwash expressions previously derived, with the aid of Eq. (36), as shown below.

The jet boundary downwash coefficients (even system) are

Vortex inside jet

$$G_{jj_{even}}(\eta) = \frac{1}{5}\frac{1-\mu^2}{1+\mu^2}\left[\frac{1}{(1/d)-\eta} - \frac{1}{(1/c)-\eta} + \frac{1}{(1/d)+\eta} - \frac{1}{(1/c)+\eta}\right] \tag{3b}$$

$$G_{oj_{even}} = -(\eta)\,\frac{1}{5}\frac{(1-\mu)^2}{1+\mu^2}\left[\frac{1}{\eta-c} - \frac{1}{\eta-d} + \frac{1}{\eta+d} - \frac{1}{\eta+c}\right] \tag{4b}$$

Vortex outside jet

$$G_{jo_{even}}(\eta) = -\frac{1}{5}\frac{(1-\mu)^2}{1+\mu^2}\left[\frac{1}{d-\eta} - \frac{1}{c-\eta} + \frac{1}{d+\eta} - \frac{1}{c+\eta}\right] \tag{21b}$$

$$G_{oo_{even}}(\eta) = -\frac{1}{5}\frac{1-\mu^2}{1+\mu^2}\left[\frac{1}{\eta-(1/c)} - \frac{1}{\eta-(1/d)} + \frac{1}{\eta+(1/d)} - \frac{1}{\eta+(1/c)}\right] \tag{22b}$$

Note that

$$G_{\cdot o_{even}} = G_{oj_{even}} \tag{39}$$

$$G_{oo_{even}} = -G_{jj_{even}} \tag{40}$$

The jet boundary downwash coefficients (odd system) are

Vortex inside jet

$$G_{jj_{odd}}(\xi,\eta) = \frac{8}{5\pi\eta}\sum_{p=0}^{\infty}(2p+1)^2\int_0^{\infty}\frac{KK'I(\eta\lambda)\sin\xi\lambda\,d\lambda}{[1/\{(1/\mu^2)-1\}] - \lambda IK'}\int_{c\lambda}^{d\lambda}\frac{I(\lambda\beta)}{\lambda\beta}\,d(\lambda\beta) \tag{6e}$$

$$G_{oj_{odd}}(\xi,\eta) = \frac{8}{5\pi\eta}\sum_{p=0}^{\infty}(2p+1)^2\int_0^{\infty}\left[\frac{1}{\mu-\lambda\{(1/\mu)-\mu\}IK'} - 1\right]\frac{K(\eta\lambda)\sin\xi\lambda d\lambda}{\lambda}\int_{c\lambda}^{d\lambda}\frac{I(\lambda\beta)}{\lambda\beta}\,d(\lambda\beta) \tag{7e}$$

Vortex outside jet

$$G_{jo_{odd}}(\xi,\eta) = \frac{8}{5\pi\eta}\sum_{p=0}^{\infty}(2p+1)^2\int_0^{\infty}\left[\frac{1}{\mu-\lambda\{(1/\mu)-\mu\}IK'} - 1\right]\frac{I(\eta\lambda)\sin\xi\lambda d\lambda}{\lambda}\int_{c\lambda}^{d\lambda}\frac{K(\lambda\beta)}{\lambda\beta}\,d(\lambda\beta) \tag{6f}$$

$$G_{oo_{odd}}(\xi,\eta) = \frac{8}{5\pi\eta}\sum_{p=0}^{\infty}(2p+1)^2\int_0^{\infty}\frac{II'K(\eta\lambda)\sin\xi\lambda d\lambda}{[1/\{(1/\mu^2)-1\}] - \lambda IK'}\int_{c\lambda}^{d\lambda}\frac{K(\lambda\beta)}{\lambda\beta}\,d(\lambda\beta) \tag{7f}$$

All Bessel functions are of $2p+1$ order and, unless otherwise shown, are of argument λ.

These jet boundary downwash coefficients may be employed in a manner similar to the wing downwash coefficients. Thus, for an odd number N of horseshoe vortices having N downwash points across the wing span (Fig. 10), the downwash velocity at any of the downwash points P_ν resulting from the boundary reaction to the N horseshoe vortices is

$$w(\xi_\nu,\eta_\nu) = \frac{1}{4\pi}\sum_{n=1}^{(N+1)/2}{}'\frac{\Gamma_n}{s}G_{\nu n} \tag{41}$$

for symmetrical loading, the prime on the summation again indicating the unique character of the center horseshoe vortex. Here the $G_{\nu n}$ is the sum of the even and odd parts. As before, this expression may be written

$$\left[w(\xi_\nu,\eta_\nu) = \frac{N}{4\pi}\sum_{n=1}^{(N+1)/2}{}'\frac{\Gamma_n}{b/2}G_{\nu n}\right]_{\nu=1,2,3\ldots[(N+1)/2]} \tag{42}$$

Total Downwash Due to a Wing Jet Combination

For small angles, the tangent-flow boundary condition

$$w(\tilde{x}_\nu,\tilde{y}_\nu) = V_\nu\sin\alpha_\nu \cong V_\nu\alpha_\nu \tag{43}$$

may be applied at each of the downwash points. Thus, combining Eqs. (35) and (42), and using Eq. (43), we have, as our final set of $(N+1)/2$ simultaneous equations in the $(N+1)/2$ unknown circulation strengths,

$$\left[V_\nu\alpha_\nu = w_\nu = \frac{N}{4\pi}\sum_{n=1}^{(N+1)/2}{}'\frac{\Gamma_n}{b/2}\{F_{\nu n}+G_{\nu n}\}\right]_{\nu=1,2,3\ldots[(N+1)/2]} \tag{44}$$

This set of equations is written in terms of the wing span b, the wing downwash coefficient $F_{\nu n}$ (see reference 14), and the jet boundary downwash coefficient $G_{\nu n}$.

The values of F are obtained from reference 18. The values of G are computed from the formulas for jet boundary downwash coefficients derived in this paper. Both the even and odd G coefficients must be used in the above equations.

To facilitate the employment of the method derived in this paper for the determination of characteristics of an arbitrary wing extending through a jet, the G coefficients, both even and odd, were programed in a parametric manner for computation by electronic data processing equipment. The required coefficients may thus be readily obtained for any arbitrary wing-jet geometry and for any desired jet velocity ratio.

Comparison of Theory With Experiment

General

The present theory provides a means to determine the lift distribution over a wing extending through a circular jet. In order to provide a comparison of the theory with experimental data, measured values of the lift at successive spanwise points must be employed. There is a dearth of such experimental data, particularly at higher values of the jet velocity ratio, where the effect would be expected to be large, and which would accordingly be of interest.

One such set of experiments is that reported by J. Stuper,[10] employing velocity ratios that are fairly low, yet probably adequate to check the theory. Fig. 16 of Stuper's paper shows the experimental results for a jet velocity ratio $\mu = 0.735$, and for several angles of attack, and also shows the comparison with Koning's theory.[5]

Stuper employed a rectangular wing 20 by 80 cm., thus having a geometric aspect ratio of 4. His use of circular end plates 32 cm. in diameter gave his wing an effective aspect ratio of 5.25 (see reference 12, p. 211). The jet was 12 cm. in diameter, so the ratio of jet diameter to wing chord was 0.6, which is thus the aspect ratio of the wing segment immersed in the jet.

Graham (see reference 9, Fig. 5.5) reproduced the data of Stuper's Fig. 16, and included a comparison with slender body theory. As observed previously, within the jet the experimental data seemed to lie between the two limiting theories, lifting line and slender body. Outside of the jet, neither theory represented the experiments very well, both lying below the experimental points. Also neither of these theories gave the sharp discontinuity in loading found experimentally at the jet boundary.

Method of Computation

In order to provide a comparison of the present theory with Stuper's experiment, the Weissinger application of the theory developed in the previous part of this paper was employed. The wing-jet geometry reported in Stuper's paper was represented by the arrangement of horseshoe vortices illustrated here in Fig. 10.

The segment of the wing in the jet was represented by 5 horseshoe vortices. Stuper's effective aspect ratio of 5.25 gave an effective span of 105 cm. Hence,

$$\eta_{tip} = (b/2)_{effective}/r_o = 52.5/6 \cong 8.75 \qquad (45)$$

which determined the spanwise extent of the vortex pattern as shown in Fig. 10, thus representing the wing by a total of $N = 45$ horseshoe vortices.

To use the Weissinger lifting surface method, the downwash due to each of the horseshoe vortices, both from the vortex itself and from the boundary reaction to the vortex, must be determined at the downwash points located at the intersection of the centerline of each such elementary horseshoe vortex and the 3/4 chord line of the wing.

The F downwash coefficients, representing the downwash due to the wing itself, are obtained for the vortex pattern of Fig. 11 from the tables of references 18 and 19. In using these tables, the value of the 3/4 chord line must be expressed in terms of the semiwidth s of the horseshoe vortex used. On this basis,

$$\bar{x} = x/s = \{-10/[(b/2)/45]\} = (-10 \times 45)/52.5 = -8.75 \qquad (46)$$

is the constant value of the 3/4 chord line used in the Stuper experiment.

The required values of the F downwash coefficients at this constant value of $\bar{x}$ are most conveniently obtained from the tables in reference 18. In those tables, the distance in the spanwise direction from the line of symmetry of a given horseshoe vortex, expressed in terms of the semiwidth s of the horseshoe vortex, is

$$\bar{y} = |2(\nu - n)| \qquad (47)$$

The values of the F wing downwash coefficients, for the case $\bar{x} = -8.75$ used in the Stuper experiment, have been taken from reference 18 and are presented in Table 1.

These F downwash coefficients are of the order of unity, and hence were computed in the tables of reference 18 to 3 decimal places, in order to provide accuracies of 3 significant figures. Hence the G downwash coefficients, representing the downwash due to the jet

Table 1
Wing Downwash Coefficients
($\bar{x} = -8.57$, see reference 18)

$\bar{y}$	F	$\bar{y}$	F
0	+4.014	34	−0.002
2	−1.320	36	−0.002
4	−0.255	38	−0.002
6	−0.104	40	−0.002
8	−0.055	42	−0.001
10	−0.033	44	−0.001
12	−0.022	46	−0.001
14	−0.016	48	−0.001
16	−0.012	50	−0.001
18	−0.009	52	−0.001
20	−0.007	54	−0.001
22	−0.006	56	−0.001
24	−0.005	58	−0.001
26	−0.004	60	−0.001
28	−0.003	62	−0.001
30	−0.003	64	−0.001
32	−0.002	66	−0.000

TABLE 2
Jet Boundary Downwash Coefficients
($\xi = -1^2/_3$; $\mu = 0.735$)

η	β	G_{even}	G_{odd}	η	β	G_{even}	G_{odd}
0	0	0.024*	0.021*	2.0	0.8	0.003	0.003
	0.4	0.048	0.042		1.2	−0.015	−0.011 (−0.011)
	0.8	0.048	0.043		1.6	−0.006	−0.004
	1.2	0.005	0.006		2.0	−0.004	−0.002
	1.6	0.003	0.003		2.4	−0.002	−0.001
	2.0	0.002	0.002		2.8	−0.002	−0.001
	2.4	0.001	0.001		3.2	−0.001	—
	2.8	0.001	0.001		3.6	−0.001	—
	3.2	0.001	—		4.0	−0.001	—
	3.6	0.001	—		4.4	−0.001	—
0.4	0	0.024*	0.021*		4.8	−0.001	—
	0.4	0.052	0.047	2.4	0	0.001*	0.001*
	0.8	0.066	0.061		0.4	0.001	0.001
	1.2	0.008	0.009		0.8	0.002	0.002
	1.6	0.004	0.004		1.2	−0.009	−0.006
	2.0	0.002	0.002		1.6	−0.004	−0.002
	2.4	0.001	0.001		2.0	−0.002	−0.001
	2.8	0.001	0.001		2.4	−0.002	−0.001
	3.2	0.001	—		2.8	−0.001	—
	3.6	0.001	—		3.2	−0.001	—
0.8	0	0.025*	0.022*		3.6	−0.001	—
	0.4	0.069	0.064 (0.063)		4.0	−0.001	—
	0.8	0.239	0.238 (0.179)	2.8	0.4	0.001	0.001
	1.2	0.031	0.034 (0.024)		0.8	0.001	0.001
	1.6	0.007	0.007		1.2	−0.006	−0.003
	2.0	0.003	0.003		1.6	−0.003	−0.001
	2.4	0.002	0.002		2.0	−0.002	−0.001
	2.8	0.001	0.001		2.4	−0.001	—
	3.2	0.001	0.001		2.8	−0.001	—
	3.6	0.001	—		3.2	−0.001	—
	4.0	0.001	—	3.2	0.4	0.001	—
1.2	0	0.003*	0.003*		0.8	0.001	0.001
	0.4	0.008	0.009		1.2	−0.004	−0.002
	0.8	0.031	0.033 (0.023)		1.6	−0.002	−0.001
	1.2	−0.180	−0.182 (−0.110)		2.0	−0.001	—
	1.6	−0.033	−0.028 (−0.026)		2.4	−0.001	—
	2.0	−0.015	−0.011		2.8	−0.001	—
	2.4	−0.008	−0.005	3.6	0.4	0.001	—
	2.8	−0.006	−0.003		0.8	0.001	—
	3.2	−0.004	−0.002		1.2	−0.003	−0.001
	3.6	−0.003	−0.001		1.6	−0.002	−0.001
	4.0	−0.002	−0.001		2.0	−0.001	—
	4.4	−0.002	−0.001		2.4	−0.001	—
	4.8	−0.002	−0.001	4.0	0.8	0.001	—
	5.2	−0.001	—		1.2	−0.002	−0.001
	5.6	−0.001	—		1.6	−0.001	—
	6.0	−0.001	—		2.0	−0.001	—
	6.4	−0.001	—		2.4	−0.001	—
	6.8	−0.001	—	4.4	1.2	−0.002	−0.001
	7.2	−0.001	—		1.6	−0.001	—
	7.6	−0.001	—		2.0	−0.001	—
	8.0	−0.001	—	4.8	1.2	−0.002	−0.001
1.6	0	0.001*	0.002*		1.6	−0.001	—
	0.4	0.004	0.004		2.0	−0.001	—
	0.8	0.007	0.007	5.2	1.2	−0.001	—
	1.2	−0.035	−0.030 (−0.028)		1.6	−0.001	—
	1.6	−0.012	−0.009	5.6	1.2	−0.001	—
	2.0	−0.006	−0.004		1.6	−0.001	—
	2.4	−0.004	−0.002	6.0	1.2	−0.001	—
	2.8	−0.003	−0.001		1.6	−0.001	—
	3.2	−0.002	−0.001	6.4	1.2	−0.001	—
	3.6	−0.002	−0.001	6.8	1.2	−0.001	—
	4.0	−0.001	—	7.2	1.2	−0.001	—
	4.4	−0.001	—	7.6	1.2	−0.001	—
	4.8	−0.001	—	8.0	1.2	−0.001	—
	5.2	−0.001	—				
	5.6	−0.001	—				
	6.0	−0.001	—				
2.0	0	0.001*	0.001*				
	0.4	0.002	0.002				

* All values are based on a pair of symmetrically spaced horseshoe vortices of span $\Delta\beta = 0.4$, except for the case $\beta = 0$, where $\Delta\beta = 0.2$. This situation results from the representation of the wing by pairs of symmetrically spaced horseshoe vortices everywhere except at the center of the wing, which is represented by a single unique vortex.

boundary, must similarly be computed to 3 decimal places, as the F and G coefficients are to be summed at each downwash point.

The G downwash coefficients were computed from the expressions derived in this paper. In using these expressions, the value of the 3/4 chord line must be expressed in terms of the jet radius r_o used. On this basis,

$$\xi = x/r_o = (-10/6) = -1^2/_3 \qquad (48)$$

is the constant value of the 3/4 chord line used in the Stuper experiment.

The definite integrals in the G_{odd} functions were evaluated by Filon's Simpson's rule, employing electronic data processing equipment. The computing was programed so that μ, ξ, β, and η were parameters, and in addition the mesh of the variable of integration λ and the upper limit of the integral could be specified. Four values of the summation index p were employed, which included Bessel functions through order seven.

Computations were carried out only for the constant values of $\xi = -1^2/_3$ and $\mu = 0.735$, corresponding to Stuper's experiment.[10] For this case trial runs showed that an interval of $\Delta\lambda = 0.5$, together with an upper limit of λ of about 12, provided sufficiently rapid convergence to give the required accuracy of 3 decimal places, although an upper limit of $\lambda = 25$ was used for the most slowly convergent cases where both the vortex and the effect point were adjacent to the jet boundary.

For the cases where both the effect point and the vortex point were adjacent or close to the jet boundary, the convergence with respect to p was inadequate to give the required accuracy of 3 decimal places for the four values of the summation index p employed. There were eight such cases.

These eight cases were then extended by employing the Aitken ∇^2 process (see reference 20, p. 126) to improve the rate of convergence of the sequence of partial sums of the series. This process was chosen because it is exact for a geometric series, which the present sums of integrals approach asymptotically for large values of the summation index p.

The computed values of the G jet boundary downwash coefficients for the case of $\xi = -1^2/_3$ and $\mu = 0.735$, used in the Stuper experiment, are presented in Table 2. For the eight cases where the G_{odd} coefficients were extended by the Aitken ∇^2 process, the extended values are those presented in the column, and the partial sums of the first four terms from which the extended values were obtained are shown in adjacent parentheses.

The G coefficients of Table 2 were at this point available for addition to the F coefficients of Table 1 in accordance with Eq. (44), to provide a set of linear simultaneous equations from which the unknown circulation strengths Γ_n could be determined.

It will be recalled that the formulation of the problem leading to Eq. (44) was based on symmetrical loading across the wing span. Hence the circulation of symmetrical vortex pairs was identical. This permitted a reduction of the number of unknown circulation strengths from $N = 45$ to $(N + 1)/2 = 23$, the odd number arising from the unique center vortex.

Hence a solution for the symmetrical Stuper wing was obtained by a set of 23 simultaneous equations in the 23 unknown circulation strengths of a half of the wing on one side of the centerline. In constructing these equations, the F coefficients for symmetrical vortex pairs were added together.

The G coefficients were derived for symmetrical vortex pairs, and so are already in the proper form for use in the 23 simultaneous equations. However, the G coefficients were computed separately for their even and odd parts, and so the sum of these two parts was used at each downwash point.

The common factors in Eq. (44) may be transposed to the other side of the equation, giving, for the Stuper wing outside the jet, at 12° angle of attack,

$$[4\pi(b/2)/N]V\alpha = [(4\pi \times 1.722)/45] \times 98.425 \times 0.209 = 9.915 \text{ ft.}^2/\text{sec.} \qquad (49)$$

Inside the jet, where the velocity is increased by a factor of 1.36, this term becomes 13.485 ft.^{2}/sec. Hence Eq. (44), for the case of the Stuper wing at 12° angle of attack, may be written explicitly as

$$\left[\sum_{n=1}^{23} \{F_{\nu n} + G_{\nu n_{even}} + G_{\nu n_{odd}}\}\ \Gamma_n = \begin{matrix} 9.915\ (\nu = 1\text{–}20) \\ 13.485\ (\nu = 21\text{–}23) \end{matrix}\right]_{\nu = 1\text{–}23} \qquad (44a)$$

In this equation the $F_{\nu n}$ coefficients are as defined in Eqs. (33) and (34). Table 1 may be used together with Eq. (47) to provide the F coefficients. Table 2 may be used together with Figs. 10 and 11 to provide the G coefficients.

The 23 simultaneous equations with the 23 unknown circulation strengths Γ_n so constructed were solved by an elimination method. The circulation strengths obtained were converted into local lift coefficients, based on V_o, by the expression

$$c_l = l_{local}/(1/2)\rho V_o^2 c = \rho(V\Gamma)_{local}/(1/2)\rho V_o^2 c \qquad (50)$$

These local lift coefficients, for the wing and jet combination, were computed as outlined above for the case of an angle of attack of 12°. The local lift coefficients were then linearly reduced for the angles of 8° and 4°. From these values, for each angle of attack, were subtracted the local lift coefficients of the wing alone. The differences, which are the increase in local lift coefficients due to the jet, were added to the experimental lift coefficients of the wing alone obtained by Stuper (see reference 10, Fig. 16), and are shown in Fig. 12.

Results

The theory of this paper has been applied to the wing-jet combination investigated experimentally by Stuper in reference 10. The correlation, presented in

Fig. 12, has been found to be excellent for that portion of the data presented by Stuper which is felt to be valid.

The present theory agrees well with the experimental data of Stuper in the jet, which is the region of greatest effect and hence of principal interest. The strong decrease in the experimental lift observed immediately outside of the jet is explained by Stuper as being due to the friction boundary layer of the fan enclosure.

The large increase in lift obtained experimentally in the region farther from the jet may be explained by the test setup shown by Stuper in his Fig. 20. The jet has a free boundary as it passes over the wing, and a free boundary for a distance of one quarter of the chord upstream from the leading edge. But for about the next two chord lengths upstream the jet has a solid boundary, in the form of the fan enclosure. The present theory, as well as Koning's theory,[5] is based on the boundary of a free jet, and would not be expected to agree with the results of a solid boundary.

The effect of this solid boundary upstream will reverse the sense of circulation of the image vortices for the upstream region, and similarly reverse the direction of the downwash induced by such image vortices in their representation of the boundary. From the geometry of the wing-jet arrangement, it is seen that the angle subtended by the fan enclosure, and hence the relative effect of the solid boundary, will have a maximum at about six jet radii outboard from the jet centerline along the 3/4 chord line. The experimental points of Stuper show such a maximum, as seen from Fig. 12.

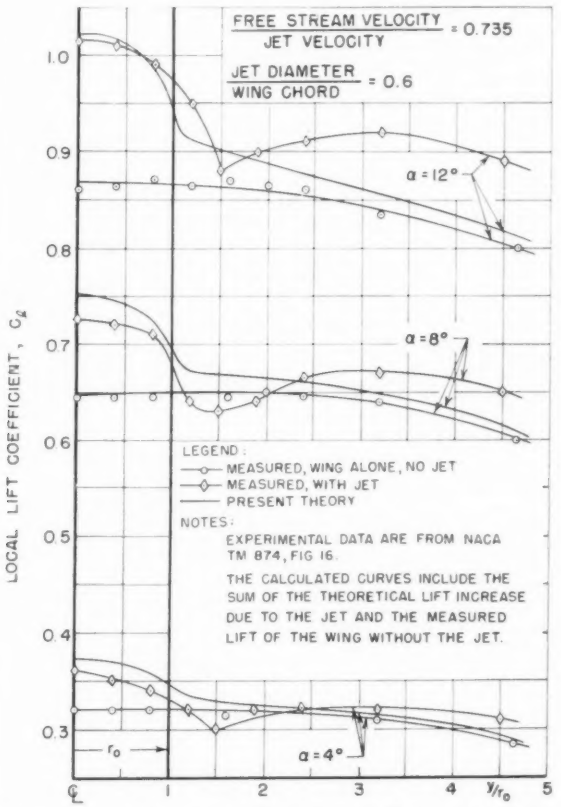
FREE STREAM VELOCITY / JET VELOCITY = 0.735
JET DIAMETER / WING CHORD = 0.6
α = 12°
α = 8°
α = 4°
LEGEND:
MEASURED, WING ALONE, NO JET
MEASURED, WITH JET
PRESENT THEORY
NOTES:
EXPERIMENTAL DATA ARE FROM NACA TM 874, FIG 16.
THE CALCULATED CURVES INCLUDE THE SUM OF THE THEORETICAL LIFT INCREASE DUE TO THE JET AND THE MEASURED LIFT OF THE WING WITHOUT THE JET.
LOCAL LIFT COEFFICIENT, C_ℓ
r_0
y/r_0

FIG. 12. Spanwise lift distribution according to theory and experiment for wing extending through circular jet.

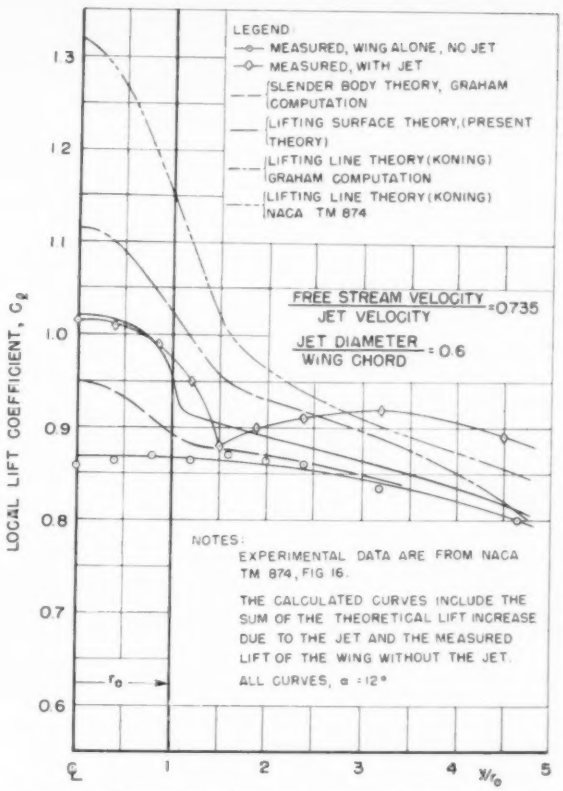
LEGEND:
MEASURED, WING ALONE, NO JET
MEASURED, WITH JET
SLENDER BODY THEORY, GRAHAM COMPUTATION
LIFTING SURFACE THEORY, (PRESENT THEORY)
LIFTING LINE THEORY (KONING) GRAHAM COMPUTATION
LIFTING LINE THEORY (KONING) NACA TM 874
FREE STREAM VELOCITY / JET VELOCITY = 0.735
JET DIAMETER / WING CHORD = 0.6
NOTES:
EXPERIMENTAL DATA ARE FROM NACA TM 874, FIG 16.
THE CALCULATED CURVES INCLUDE THE SUM OF THE THEORETICAL LIFT INCREASE DUE TO THE JET AND THE MEASURED LIFT OF THE WING WITHOUT THE JET.
ALL CURVES, α = 12°
LOCAL LIFT COEFFICIENT, C_ℓ
r_0
y/r_0

FIG. 13. Comparison of various theories with experiment for spanwise lift distribution of wing extending through circular jet.

Furthermore, the lift increment obtained by the theory is the difference of opposing effects. Examination of these individual effects for the present case of the Stuper experiment has shown the lift increment to be a relatively small difference of large effects. Hence the large effects at appreciable distances from the jet boundary obtained experimentally by Stuper are felt to be understandable in view of the experimental test setup he employed.

The strong decrease in experimental lift observed immediately outside of the jet could also be partly caused by the solid boundary upstream, although the dynamic pressure drop in the transition region between the jet and the undisturbed flow caused by the friction boundary layer of the fan enclosure would seem to offer an adequate explanation.

The Koning theory differs from the present theory essentially in that Koning considers only what in this paper has been termed the even part, and disregards the odd part. Hence the difference in the results obtained by the present theory must be attributed to the inclusion of the odd part. The several theories are compared in Fig. 13, which includes Koning's theory, as computed both by Stuper (see reference 10, Fig. 16) and by Graham (see reference 9, Fig. 5.5), as well as

slender body theory, as computed by Graham. It is seen that the present theory is in substantial agreement with the valid experimental points in the jet, and lies between lifting line theory and slender body theory, as expected.

As may be observed in Table 2, for the present case of Stuper's experiment the jet boundary downwash coefficients for the odd part were of the same order as those for the even part, particularly for the spanwise points of major contribution near the jet boundary. Hence the agreement of the present theory with the experimental results of Stuper must be attributed to the inclusion of the odd part.

Conclusions

A strong correlation of the theory with the available experimental data has been demonstrated. The rapid approach of the downwash induced by the jet boundary, caused by the odd parts of horseshoe vortices representing a wing, to its asymptotic even value downstream of the lifting line emphasizes the importance of the odd part in obtaining this correlation.

The wing segment immersed in the jet in the Stuper experiment, used for comparison with the theory, was of aspect ratio = 0.6. For this aspect ratio, and for the spanwise points of major contribution near the jet, the boundary induced downwash at the 3/4 chord points used in the Weissinger analysis was almost the Trefftz plane value. The conclusion is clear that for such low aspect ratio immersed segments the use of lifting line theory introduces serious error, and that an approximate lifting surface theory such as that of Weissinger is required.

For wing segments immersed in the jet of aspect ratio of the order o one, the downwash over the wing, and in particular at the 3/4 chord point, will be in general intermediate between the value at the Trefftz plane and half that value at the lifting line. This variation is large, and the lift distribution predicted by the theory is quite sensitive to the value of the downwash used. The present theory provides a means to determine the proper downwash, and more accurate predictions of lift distribution may be obtained thereby.

References

[1] Rethorst, Scott, *Characteristics of an Airfoil Extending through a Circular Jet*, GALCIT, Ph.D. Thesis, 1956.

[2] Rethorst, Scott, *Lift on a Wing in a Propeller Slipstream as Related to Low-Speed Flight*, Aeronautical Engineering Review, Vol. 15, No. 10, pp. 42–48, October, 1956.

[3] von Kármán, Th., and Tsien, H. S., *Lifting-Line Theory for a Wing in Non-Uniform Flow*, Quarterly of Applied Mathematics, Vol. III, No. 1, pp. 1–11, 1945.

[4] Fejer, Andrew, *Lifting-Line Theory in Linearly Varying Flow*, GALCIT, Ph.D. Thesis, 1945.

[5] Durand, W. F., (Ed.), *Aerodynamic Theory*, Koning, C., "Influence of the Propeller on Other Parts of the Airplane Structure," Vol. IV, J. Springer, Berlin, 1935.

[6] Millikan, Clark B., *The Influence of Running Propellers on Airplane Characteristics*, Journal of the Aeronautical Sciences, Vol. 7, No. 3, pp. 85–106, January, 1940.

[7] Smelt, R., and Davies, H., *Estimation of Increase in Lift Due to Slipstream*, British ARC R&M 1788, 1937.

[8] Weil, J., and Sleeman, W. C., Jr., *Prediction of the Effects of Propeller Operation on the Static Longitudinal Stability of Single-Engine Tractor Monoplanes with Flaps Retracted*, NACA TN 1722, 1948.

[9] Graham, E. W., Lagerstrom, P. A., Licher, R. M., and Beane, B. J., *A Preliminary Theoretical Investigation of the Effects of Propeller Slipstream on Wing Lift*, Douglas Aircraft Co. Report SM-14991, 1953.

[10] Stuper, J., *Einfluss des Schraubenstrahls auf Flugel und Leitwerk*, Luftfahrtforschung, Vol. 15, No. 4, 1938; also published as NACA TM 874, 1938.

[11] Lotz, I., *Korrecktur des Abwindes in Windkanalen mit kreisrunden oder elliptischen Querschnitten*, Luftfahrtforschung, Vol. 12, No. 8, pp. 250–264, December 25, 1935; also published as NACA TM 801, 1936.

[12] Durand, W. F., (Ed.), *Aerodynamic Theory*, von Kármán, Th., and Burgers, J. M., "Influence of Boundaries in the Field of Motion around Airfoil Systems," Vol. II, J. Springer, Berlin, 1935.

[13] Eisenstadt, Bertram J., *Boundary Induced Upwash for Yawed and Swept-Back Wings in Closed Circular Wind Tunnels*, NACA TN 1265, 1947.

[14] Campbell, George S., *A Finite Step Method for the Calculation of Span Loadings of Unusual Plan Forms*, NACA Research Memorandum L50L13, 1951.

[15] Weissinger, J., *Uber die Auftriebsverteilung von Pfeilflugeln*, Forschungsbericht Nr 1553, 1942. Also NACA TM 1120, 1947.

[16] Gray, A., Mathews, G. B., and MacRobert, T. M., *A Treatise on Bessel Functions*, 1931.

[17] Erdelyi, A., *Higher Transcendental Functions*, Vol. 2, 1953.

[18] Staff of the Mathematics Division, *Tables of Complete Downwash Due to a Rectangular Vortex*, British A.R.C. Rep. No. 10754, July 21, 1947; also published as R&M No. 2461, 1953.

[19] Diederich, Franklin W., *Charts and Tables for Use in Calculations of Downwash of Wings of Arbitrary Plan Form*, NACA TN 2353, 1951.

[20] Householder, Alston S., *Principles of Numerical Analysis*, 1953.

The Hydrodynamics and Heat Conduction of a Melting Surface

GEORGE W. SUTTON*
General Electric Company

SUMMARY

In previous investigations of surface melting the assumption is usually made that, upon melting, the molten liquid is immediately removed. In this paper, this assumption is relaxed and the governing differential equations are presented. Solutions are obtained for the aerodynamic melting of Pyrex glass at a stagnation point, giving the velocity and temperature profiles of the molten film, and its thickness. The results indicate that the presence of the film cannot be ignored because the melting rate is more rapid than that predicted by simple theory. In spite of the additional complexity of the model, the melting rate is found to be linearly dependent upon the heat-transfer rate, and this relation is relatively insensitive to Mach Number, altitude, mass-transfer rate, and interface shear stress for the range of values considered.

SYMBOLS

C_p = specific heat at constant pressure
F = similarity stream function
k = coefficient of thermal conductivity
K = density ratio across normal shock wave
m = mass transfer, $-\rho v$
P_r = Prandtl Number, $C_p\mu/k$
p = pressure
q = heat-transfer rate
R_b = stagnation point radius of curvature of body
T = temperature
u, v = fluid velocities
x, y = coordinates
μ = viscosity, $\mu(T)$
τ = shear stress
Θ = dimensionless temperature ratio, $(T - T_0)/T^*$
ϵ = 0 for planar flow
ϵ = 1 for axially symmetric flow
ρ = density
ζ = dimensionless distance

Subscripts and Superscripts

0 = interior of surface material
m = melting point
e = outer edge of gaseous boundary layer
∞ = ahead of normal shock wave
i = gaseous boundary layer - liquid film interface
s = stagnation point
δ = liquid-solid interface
$*$ = reference

INTRODUCTION

A LARGE NUMBER of investigations have been conducted recently to determine the aerodynamic heat transfer to vehicles traveling at high speeds. The results of these studies indicate that at altitudes at which air is continuum—that is, below 250,000 ft.—the aerodynamic heating, especially in the region of the stagnation point, is sufficiently great that some method of heat absorbtion or cooling is required. However, if the flight time is sufficiently short, as is the case for rapid exit or entry into the earth's atmosphere, it may be possible to allow a portion of the surface to melt and vaporize.

In order to design such a system accurately, it is necessary to predict precisely the rate at which the melting surface recedes. Any such theory should consider the effect of the molten liquid film which previous analyses of the problem of surface melting have ignored.[1]

The object of the present paper is to determine quantitatively the effect of such a molten liquid film in laminar flow at a stagnation point. The general equations are presented, and the results of some typical calculations are given in which the viscosity of the melt is allowed to be a function of temperature. The assumption is made that the system is in quasi-steady state; this will not affect the generality of the conclusions.

The coordinate system is shown in Fig. 1; it is attached to the interface between the molten material and the gaseous boundary layer. It is assumed that the rate of change of the vehicle shape due to melting is small.

BOUNDARY CONDITIONS

The assumption is made that the molten surface material is acted upon by aerodynamic heating and skin friction τ_i. In addition, there may be mass transfer into the gaseous boundary layer, caused by evaporation or by pyrolysis of the molten liquid film. In the former case, mass transfer is controlled by the vapor pressure of the material and by diffusion in the boundary layer; in the latter case, the ratio is fixed by the chemistry of the material. It is convenient to choose the following boundary conditions at $y = 0$:

$$v(0) = -m_i/\rho, \quad (\partial u/\partial y)(0) = -\tau_i/\mu_i, \quad T(0) = T_i \tag{1}$$

Two additional boundary conditions are necessary. They may be chosen in the interior of the surface material as follows. For a material with a definite melt-

Received June 6, 1957.

* Research Engineer, Aerophysics Laboratory Operation, Missile and Ordnance Systems Department.

The author wishes to show his appreciation to Dr. Joseph Farber and Dr. Sinclaire M. Scala for their many helpful discussions, and to Mr. Sheldon Blecher for his assistance in carrying out the computations.

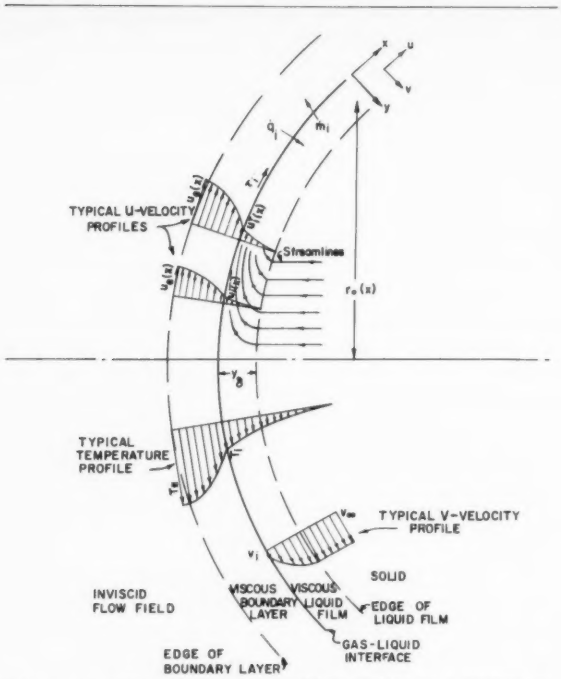

FIG. 1. Coordinate system for melting surface at a stagnation point.

ing point the tangential velocity is zero at the melting point, hence,

$$\text{at} \quad y = y_\delta: \qquad u = 0, \quad T = T_m \tag{2}$$

However some materials, such as glasses, do not exhibit a definite melting point. The boundary conditions for this class of materials are as follows:

$$\lim_{y \to \infty} u(y) = 0, \quad \lim_{y \to \infty} T(y) = T_0 \tag{3}$$

It is implicit in these boundary conditions that the material is semi-infinite.

Governing Equations

If the Reynolds Number based on a typical dimension is large, then the governing equations are identical to the usual laminar boundary-layer equations. These equations are:[2]

Continuity

$$(\partial/\partial x)\,(ur_0^{\epsilon}) + (\partial/\partial y)\,(vr_0^{\epsilon}) = 0 \tag{4}$$

Momentum

$$\left.\begin{aligned} \rho u(\partial u/\partial x) + \rho v(\partial u/\partial y) &= -(\partial p/\partial x) + \\ &\quad (\partial/\partial y)\,[\mu(\partial u/\partial y)] \\ 0 &= \partial p/\partial y \end{aligned}\right\} \tag{5}$$

Energy

$$\rho C_p[u(\partial T/\partial x) + v(\partial T/\partial y)] = u(\partial p/\partial x) + (\partial/\partial y)\,[k(\partial T/\partial y)] + \mu(\partial u/\partial y)^2 \tag{6}$$

If the Reynolds Number is of order of magnitude 1, then the convective terms may be omitted from Eq. (5); however, the convective terms remain in Eq. (6) if the Prandtl Number of the molten liquid film is large. For most materials, and especially the example considered herein, the variations in density, specific heat, and thermal conductivity are small in comparison to the variation of viscosity with temperature—hence, they are assumed constant. Thus, the Prandtl Number will vary with temperature. The following incompressible transforms which include the Manger transform[3] are next used to convert Eqs. (5) and (6) into ordinary differential equations:

$$\tilde{s} = \rho\mu^* \int_0^x u_e(x) r_0^{2\epsilon}(x)\,dx \tag{7}$$

$$\zeta = [\rho/(2\tilde{s})^{1/2}]\,u_e(x) r_0^{\epsilon}(x)\,y \tag{8}$$

The following is used as the stream function:

$$\psi = (2\tilde{s})^{1/2} F(\zeta) \tag{9}$$

$$\text{where} \quad \rho u r_0^{\epsilon} = \partial\psi/\partial y, \quad \rho v r_0^{\epsilon} = -(\partial\psi/\partial x) \tag{10}$$

$$\text{Also, let} \qquad \Theta = (T - T_0)/T^* \tag{11}$$

Eqs. (5) and (6) then become

Momentum

$$[(\mu/\mu^*)F_{\zeta\zeta}]_\zeta + F_{\zeta\zeta} + \beta[(\rho_e/\rho) - F_\zeta^2] = 0 \tag{12}$$

Energy

$$F\Theta_\zeta + (k/C_F\mu^*)\Theta_{\zeta\zeta} + (u_e^2/C_pT^*) \times [(\mu/\mu^*)F_{\zeta\zeta}^2 - \beta(\rho_e/\rho)F_\zeta] = 0 \tag{13}$$

where $\beta \equiv 2\tilde{s}\,(\partial u_e/\partial \tilde{s})_s/u_e$ is $1/2$ at an axially symmetric stagnation point and is zero for zero pressure gradient. For stagnation point calculations, the last term in Eq. (13) may be neglected because $u_e^2 \ll C_pT^*$. In the remainder of this note, only stagnation point flow on a blunt body will be considered for two reasons: (1) it is of foremost technical interest, and (2) the flow is most likely to be laminar at this point. The relations between the physical variables and the dimensionless variables at a stagnation point are given by the following relations:

$$F = -[(\epsilon + 1)\mu^*(\partial u_e/\partial x)_s\rho^{-1}]^{-1/2} v \tag{14}$$

$$F_\zeta = u/u_e \tag{15}$$

$$F_{\zeta\zeta} = -(\mu^*/\mu)\,[(\epsilon + 1)\mu^*\rho(\partial u_e/\partial x)_s^3]^{-1/2}(\partial\tau/\partial x) \tag{16}$$

$$\Theta = (T - T_0)/T^* \tag{17}$$

$$\Theta_\zeta = -(1/kT^*)\,[(\epsilon + 1)\rho(\partial u_e/\partial x)_s\mu^{*-1}]^{-1/2} q \tag{18}$$

$$\zeta = [(\epsilon + 1)\rho(\partial u_e/\partial x)_s\mu^{*-1}]^{1/2} y \tag{19}$$

The appropriate boundary conditions for Eqs. (12) and (13) are obtained by the substitution of Eqs. (1), (2), and (3) into Eqs. (14)–(18). The melting rate is given by $\lim_{y \to \infty} v(y)$.

Application to a Particular Case—The Melting of Pyrex Glass

It is obvious that one has an almost endless variety of materials which may be analyzed. However, for the

purpose of analysis, they are characterized by the Prandtl Number at some reference temperature, and the manner in which the viscosity varies with temperature. Thus, one is still faced with an infinite set of parameters. However, if one is satisfied with knowledge concerning the *effect* of the film, then only three cases need be analyzed—Prandtl Number much greater than unity, equal to unity, and much less than unity. The viscosity behavior of most liquids resembles an Arrhenius function and is, therefore, not a major determining factor.

Since it is the purpose of this paper to determine the maximum effect of the molten film, a material which possesses a large Prandtl Number in the range of temperatures of interest and with no definite melting point was sought as the example. Due to the availability of data concerning its high-temperature properties, Pyrex glass (Corning 7740 glass) was chosen. Its thermal conductivity was estimated from the theory of normal liquids[4] as $k = 1.71 \times 10^{-3}$ B.t.u./ft. °F. sec.

For the viscosity, it was found that the following expression fitted published data[5] quite well:

$$\mu = 0.0672e^{(8720/T)^{1.612}} \text{ lb./ft.-sec.} \qquad (20)$$

The density was taken as 131 lb./ft.^{3} and the specific heat as 0.29 B.t.u./lb. In the case of Pyrex, evaporation or pyrolysis of its constituents represents the mass transfer.

The equations were solved by means of a REAC differential analyzer. Preliminary results indicated that the terms F_ξ^2 and $FF_{\xi\xi}$ were negligible, and these terms were then omitted from the momentum equation.

Two more parameters must be chosen. The density ratio ρ_e/ρ was taken as 1.37×10^{-4}; this corresponds precisely to Mach 18 at 90,000 ft. altitude. At this altitude, the density ratio does not vary appreciably

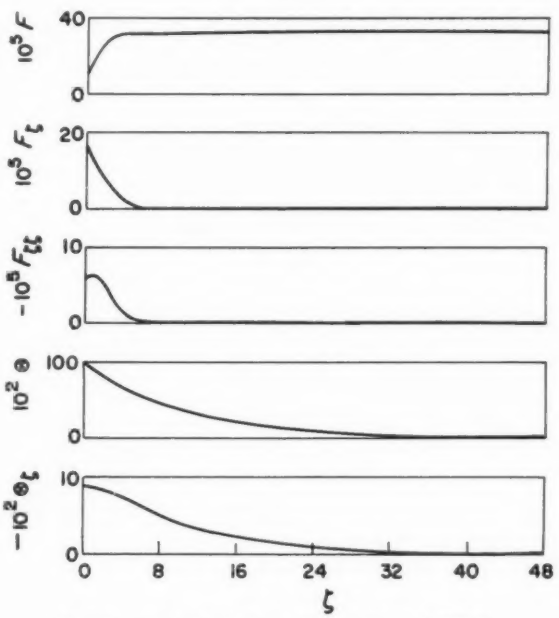

FIG. 2. Typical set of profiles for $T_i = 4{,}000$°F.

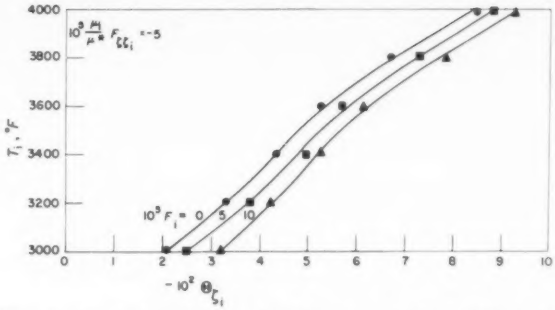

FIG. 3. Typical variation of surface temperature with nondimensional heat-transfer rate.

with Mach Number; hence the example may be considered to be hypersonic flight at that altitude. The temperature in the interior of the glass, T_0, is assumed to be zero. T^* has been taken as 4,000°F., but this does not affect the results; any value could have been chosen.

The equations were solved for the following boundary conditions at the interface:

$$T_i = 4{,}000,\ 3{,}800,\ 3{,}600,\ 3{,}400,\ 3{,}200,\ 3{,}000°\text{F.}$$

$$(\mu_i/\mu^*)F_{\xi\xi_i} = 0,\ -5 \times 10^{-5},\ -10 \times 10^{-5}$$

$$F_i = 0,\ 5 \times 10^{-5},\ 10 \times 10^{-5}$$

RESULTS

A typical set of profiles are shown in Fig. 2. One immediately notices that all of the curves, except $F_{\xi\xi}$ resemble exponential functions. This is to be expected from the nature of the equations. It is also interesting to note that the thickness of the molten flowing region is about one-tenth that of the heated region. Notice also that, at the point where $F_\xi = 0$, the value of Θ_ξ is only 70 per cent of its value at the interface. This means that only 70 per cent of the energy originally transferred to the interface is conducted into the nonflowing solid interior. Thus the presence of the liquid film cannot be ignored in this case.

For the conditions investigated it was found that, as expected, the interface temperature increased monotonically with interphase energy transfer, but varied slightly with interface shear stress and interphase mass transfer. A typical set of curves showing the interface temperature is shown in Fig. 3 in terms of the dimensionless variables.

Now a high interface temperature has the effect of markedly decreasing the viscosity of the glass so that the liquid film flows more readily under the action of a given pressure gradient and shear stress. The decrease in viscosity thus causes the surface to recede at a faster rate, as shown in Fig. 4. Hence, as the heat transfer to the surface is increased, the rate at which the surface recedes is increased. This effect is shown in Fig. 5, where it is seen that the relation between heat-transfer and melting rate is almost linear. Note that the surface shear or interphase mass transfer have negligible effect on the melting rate for the range of values investi-

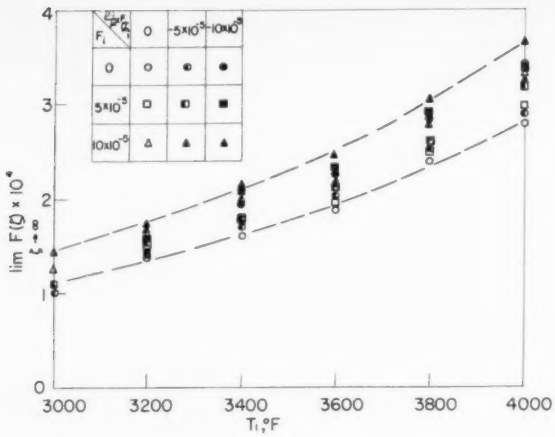

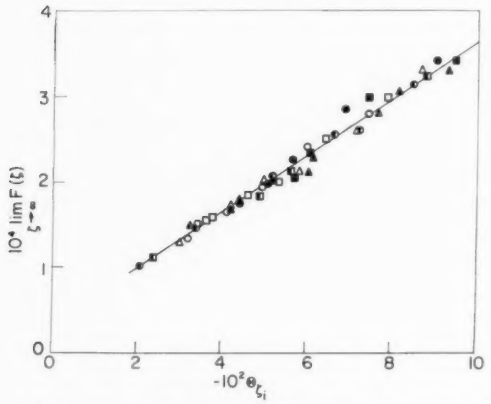

FIG. 4 (*top*). Variation of nondimensional melting rate with surface temperature.
FIG. 5 (*bottom*). Variation of melting rate with heat-transfer rate.

gated. It is not known whether this is merely coincidental for this particular material or if this effect is general. The maximum value of the tangential velocity component was about $2 \times 10^{-4}\ u_e$. The nondimensional film thickness was almost constant, 5.5 ± 10 per cent. The local tangential shear stress increases linearly with y from its value at the gas-liquid interface. Of course, this is meaningless beyond y_δ, for in that region the equations of elasticity apply, not the Navier-Stokes equations.

Calculations were also performed for hypersonic flight speed at altitudes of 70,000, 120,000, and 160,000 ft. At each of these altitudes, the relation between melting rate and heat-transfer rate was also nearly linear, and was also insensitive to the interface shear stress. The linear relation for each altitude was almost identical to that shown in Fig. 5.

The calculations were repeated for common lime glass, whose high temperature viscosity is much less than Pyrex. For this glass, it was found that the melting rates, as given by $\lim_{y\to\infty} v(y)$, were five times greater than for Pyrex for the same energy flux to the interface. Thus, viscosity plays an extremely important role in determining the melting rate.

Asymptotic Form of Energy Equation

For ζ greater than ζ_δ, the value of F is virtually constant. Hence, let

$$F(\zeta > \zeta_\delta) = \lim_{\zeta\to\infty} F(\zeta) \equiv F_\infty \tag{21}$$

The energy equation then becomes

$$F_\infty \Theta_\zeta + (1/P_r^*)\Theta_{\zeta\zeta} = 0 \tag{22}$$

This equation is easily solved for $\Theta(\zeta)$ and $\Theta_\zeta(\zeta)$ in terms of a multiplicative constant. Their ratios are given by

$$\Theta_\zeta(\zeta)/\Theta(\zeta) = -F_\infty P_r^* \quad (\zeta > \zeta_\delta) \tag{23}$$

Now, at ζ_δ it was found that $\Theta(\zeta_\delta)$ was equal to 0.62 ± 3 per cent. In addition, F_∞ is nearly proportional to Θ_{ζ_i} from Fig. 5. Thus, the ratio $\Theta_\zeta(\zeta_\delta)/\Theta_{\zeta_i}$ is almost a constant. The value of the constant was 0.75 ± 0.05. Thus, the heat conducted into the unmelted solid is an almost constant fraction of that conducted into the molten film at the gas-liquid interface.

Discussion

It is of interest to compare the results to the simple melting theory,[1] which may be expressed as follows:

$$\lim_{y\to\infty} v(y) = -[q_i/C_p\rho(T_i - T_0)] \tag{24}$$

or, in terms of the dimensionless variables,

$$\lim_{\zeta\to\infty} F(\zeta) = -(T^*\Theta_{\zeta_i}/P_r^* T_i) \tag{25}$$

Eq. (24) cannot be applied to this example, because it does not predict the interface temperature T_i. Even when the correct values of T_i is inserted into Eq. (24), it predicts a value of $\lim_{\zeta\to\infty} F(\zeta)$ which is too small by 23 per cent for T_i = 3,000°F. and 28 per cent too small for T_i = 4,000°F. This is to be expected since most of the material which flows has a temperature less than T_i. If, on the other hand, one uses T_δ instead of T_i in Eq. (25), then the melting rate predicted by the simple theory is larger than that predicted by the present analysis.

Eq. (19) shows that the thickness of the liquid film varies with $(\partial u_e/\partial x)_s^{-1/2}$. Since[6]

$$(\partial u_e/\partial x)_s = (v_\infty/R_b)\ [2K(1 - K)]^{1/2} \tag{26}$$

the thickness of liquid film depends on the Mach Number, altitude, and size. For a melting test of a model in a rocket exhaust the predicted thickness of melt is about 0.016 in., which compares favorably with experiment; the corresponding value for a vehicle for which the Mach Number is 18 and R_b = 1 ft. is 0.071 in. at 90,000 ft. altitude.

In the above problem it has been assumed that the system is in a quasi-steady state so that all time derivatives are zero. In an actual vehicle the surface shear stress, pressure gradient, and heat flux may vary with time. However, for a heating rate of 1,000

(*Continued on page 36*)

Incompressible Potential Flow About Axially Symmetric Bodies in Ducts*

PHILIP LEVINE**

Wright Air Development Center, ARDC

SUMMARY

The velocity potentials and stream functions for a point source, doublet, ring source, ring doublet, disc source, disc doublet, and ring vortex are derived for the case of axially symmetric incompressible potential flow in an infinitely long duct of constant diameter. Several examples are carried out to illustrate the nature of the flow about simple body shapes.

SYMBOLS

a	= radius of a ring or disc source, sink, or doublet
e	= natural logarithm base
ψ	= stream function
j	= eigenvalue
J, Y	= Bessel functions of the first and second kind, respectively
m	= strength of a source or sink form
M	= strength of a doublet form
r	= dimensionless radial coordinate; ratio of radial distance to duct radius
S	= ratio of $2m/U$
U	= superimposed uniform flow velocity
z	= dimension'ess axial coordinate; ratio of axial distance to duct radius
ϕ	= velocity potential
ϕ_z, ϕ_r	= axial and radial velocity components, respectively
$\|\ \|$	= absolute value sign

Subscripts

r	= partial differentiation with respect to r
z	= partial differentiation with respect to z

INTRODUCTION

THE PROBLEM of determining the complete flow field about axially symmetric bodies in ducts occurs widely. Typical instances are the design and analysis of the performance of axisymmetric nozzles and diffusers utilizing center-bodies, axisymmetric wind-tunnel arrangements, ring-type flame holders, and turbomachinery elements generally. In view of the numerous practical applications, it was decided to initiate a study of the problem for the case of incompressible flow.

Received May 14, 1957.

* This work was done at the Fluid Dynamics Research Branch, of the Aeronautical Research Laboratory, Directorate of Research, Wright Air Development Center, under Task 70151, Project 3066, and was presented in partial fulfillment of the requirements for the degree of Master of Science at the Ohio State University. The author wishes to acknowledge the assistance of Prof. A. N. Tifford of Ohio State University and Dr. G. Guderley of WADC for stimulating discussions.

** Formerly Task Scientist, Fluid Dynamics Research Branch, WADC. Now Senior Scientist, Avco Research and Advanced Development Division, Lawrence, Mass.

Little theoretical work has been published concerning the flow about axisymmetric bodies which fill a sizable portion of the cross-sectional area of a duct. A solution for a point source in an infinitely long duct of constant diameter has recently been published.[1] However, a numerical error occurs in the expression for the velocity potential of a point source. The expression is rederived here, as it forms the basis for the development of a general approach to the study of the flow about axisymmetric bodies in ducts.

ANALYSIS

The problem to be considered is the case of steady, incompressible and potential flow about axisymmetric bodies located on the axis of an infinitely long tube of constant diameter.

The differential equation for the velocity potential of an axisymmetric incompressible flow is well known, and may be written as[2]

$$\phi_{rr} + (1/r)\phi_r + \phi_{zz} = 0 \qquad (1)$$

Fortunately, this equation is amenable to solution by the method of separation of variables. Since Eq. (1) is linear, solutions can be built up by superposition.

Point Source on the Tube Axis

An expression for the velocity potential of a point source will be developed first. Once it is in hand, the solutions for a sink and doublet follow directly.

Consider a source of strength m, as shown in Fig. 1, located at $z = r = 0$. The boundary conditions which must be satisfied are:

(I)	$z = \pm\infty$;	$\phi_r = 0$
(II)	$z = +\infty$;	$\phi_z = 2m$
	$z = -\infty$;	$\phi_z = -2m$
(III)	$r = 1$;	$\phi_r = 0$
(IV)	$z = 0$;	$\phi_z = 0$ for $r \neq 0$

(For detailed discussions of the boundary conditions and other aspects of the following text, the reader is referred to references 1, 3, 4, and 5.)

Proceeding by the method of separation of variables, a solution to Eq. (1) exists in the form

$$\phi = 2mz + (A_1 e^{-jz} + A_2 e^{zj}) \times [B_1 J_0(jr) + B_2 Y_0(jr)] \qquad (2)$$

To satisfy conditions (I) and (II), it is apparent that either A_1 or A_2 is zero (depending on whether z is

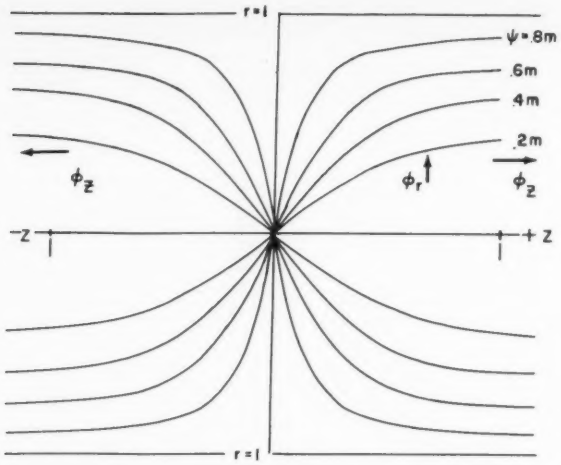

FIG. 1. Coordinate system and streamlines of a point source.

positive or negative), and $B_2 = 0$. Condition (III) requires that

$$J_1(j) = 0; \quad j \neq 0$$

Therefore, the values of (j) are the nth-ordered roots of J_1, where J_1 is the Bessel function of the first kind of first order. To satisfy condition (IV), let

$$\phi = \pm 2mz + \sum_{n=1}^{\infty} A_n e^{-j_n|z|} J_0(j_n r) \tag{3}$$

Introducing condition (IV) and the orthogonality property of Bessel functions, one can solve for the coefficients,

$$A_m = \frac{-2}{j_m J_0^2(j_m)} \int_0^1 (\phi_z)_{z=0} r J_0(j_m r) dr$$

Taking the size of the source to be very small (close to a mathematical point), and utilizing the Gauss theorem, the coefficients can be reduced to

$$A_m = (-2m)/j_m J_0^2(j_m) \tag{4}$$

Substituting Eq. (4) into Eq. (3) yields the velocity potential for a point source,

$$\phi = \pm 2mz - 2m \sum_{n=1}^{\infty} \frac{e^{-j_n|z|}}{j_n J_0^2(j_n)} J_0(j_n r) \tag{5}$$

The stream function corresponding to the above velocity potential is

$$\psi = \pm mr^2 \pm 2mr \sum_{n=1}^{\infty} \frac{e^{-j_n|z|}}{j_n J_0^2(j_n)} J_1(j_n r) \tag{6}$$

sign convention: (+) for $z > 0$
(−) for $z < 0$

At $z = 0$, the stream function is discontinuous, so that approaching $z = 0$ from the left (see Fig. 1), $\psi = -m$, while approaching $z = 0$ from the right, $\psi = +m$.

Doublet on the Tube Axis

To derive the velocity potential for a doublet, one has only to place a source and sink of the same strength a small distance apart on the axis, and find the resultant potential under the condition that

$$M = \lim_{\Delta z \to 0} m \, \Delta z$$

where M is the strength of the doublet. The velocity potential for a doublet is then

$$\phi = 2M + 2M \sum_{n=1}^{\infty} \frac{e^{-j_n|z|}}{J_0^2(j_n)} J_0(j_n r) \tag{7}$$

The corresponding stream function is

$$\psi = -2Mr \sum_{n=1}^{\infty} \frac{e^{-j_n|z|}}{J_0^2(j_n)} J_1(j_n r) \tag{8}$$

Ring Source

The velocity potential of a ring source can be found by using the same approach as taken for a point source. The boundary conditions put forth for the point source are valid in this case also, except condition (IV), which must be modified as follows:

(IVa) $z = 0; \quad \phi_z = 0$ for $r \neq a$

The total strength m of the ring source is taken to be uniformly distributed about the circumference, so that the source flow emitted by the ring is $4\pi m$. Therefore, Eq. (3) is valid for a ring source as well as a point source. To obtain the coefficients A_n, condition (IVa) and the Gauss theorem must be utilized, finally yielding

$$A_m = [(-2)/j_m J_0^2(j_m)] J_0(j_m a)$$

The velocity potential for a ring source is

$$\phi = \pm 2mz - 2m \sum_{n=1}^{\infty} \frac{e^{-j_n|z|}}{j_n J_0^2(j_n)} J_0(j_n r) J_0(j_n a) \tag{9}$$

The corresponding stream function is

$$\psi = \pm mr^2 \pm 2mr \sum_{n=1}^{\infty} \frac{e^{-j_n|z|}}{j_n J_0^2(j_n)} J_1(j_n r) J_0(j_n a) \tag{10}$$

sign convention: (+) for $z > 0$
(−) for $z < 0$

At $z = 0$, $\psi = \pm m$, depending on whether the plane of the ring source is approached from the right or left.

Ring Doublet

The velocity potential for a ring doublet and the corresponding stream function can be obtained by the same technique as used for the point doublet. The resultant expressions are

$$\phi = 2M + 2M \sum_{n=1}^{\infty} \frac{e^{-j_n|z|}}{J_0^2(j_n)} J_0(j_n r) J_0(j_n a) \tag{11}$$

$$\psi = -2Mr \sum_{n=1}^{\infty} \frac{e^{-j_n|z|}}{J_0^2(j_n)} J_1(j_n r) J_0(j_n a) \tag{12}$$

Disc Source

The boundary conditions for the velocity potential of a disc source are the same as for the point source, ex-

cept condition (IV), which is now

(IVb) $z = 0; \quad \phi_z = 0 \quad$ for $\quad r > a$

The total strength m of the disc source is taken to be uniformly distributed over the disc, so that the source flow emitted by the disc is $4\pi m$. Eq. (3) is valid for this case also, and the coefficients A_n evaluated using condition (IVb) take the form

$$A_m = [(-4m)/aj_m^2 J_0^2(j_m)]J_1(j_m a)$$

The velocity potential and stream function are as follows:

$$\phi = \pm 2mz - \frac{4m}{a} \sum_{n=1}^{\infty} \frac{e^{-j_n|z|}}{j_n^2 J_0^2(j_n)} J_0(j_n r) J_1(j_n a) \quad (13)$$

$$\psi = \pm mr^2 \pm \frac{4mr}{a} \sum_{n=1}^{\infty} \frac{e^{-j_n|z|}}{j_n^2 J_0^2(j_n)} J_1(j_n r) J_1(j_n a) \quad (14)$$

sign convention: $(+)$ for $z > 0$
$(-)$ for $z < 0$

At $z = 0$, $\psi = \pm m$, depending on whether the plane of the disc source is approached from the right or left.

Disc Doublet

Following the approach for the point doublet, the velocity potential and corresponding stream function for a disc doublet are

$$\phi = 2M + 2M \sum_{n=1}^{\infty} \frac{e^{-j_n|z|}}{j_n J_0^2(j_n)} J_0(j_n r) J_1(j_n a) \quad (15)$$

$$\psi = \frac{-4Mr}{a} \sum_{n=1}^{\infty} \frac{e^{-j_n|z|}}{j_n J_0^2(j_n)} J_1(j_n r) J_1(j_n a) \quad (16)$$

Ring Vortex

The velocity potential for a ring vortex is readily obtained by employing the property that a ring vortex is equivalent to a uniform distribution of doublets over the surface bounded by it.[2] The axes of the doublets are taken normal to the surface everywhere, and the

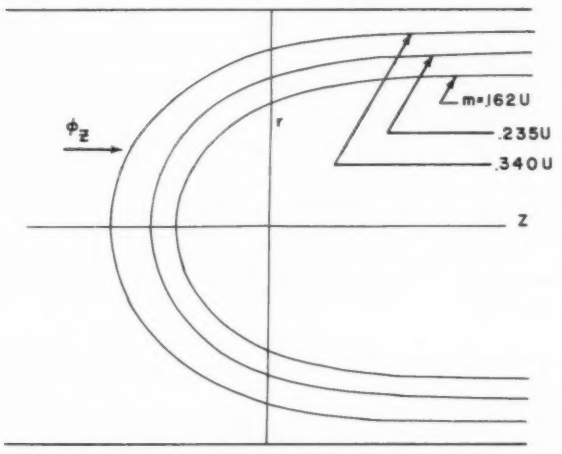

FIG. 2. Point sources in a uniform flow.

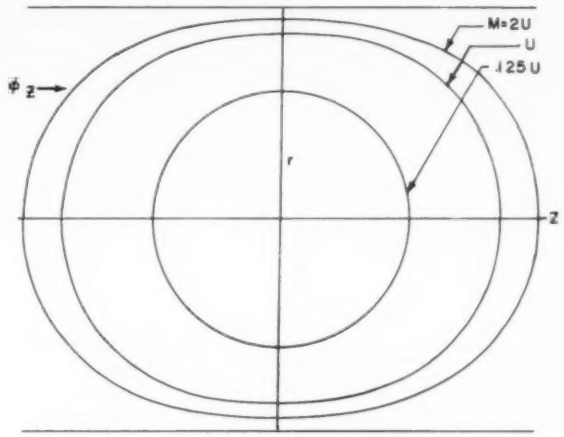

FIG. 3. Doublets in a uniform flow.

density of the distribution is equal to the strength of the vortex. Thus, by Eq. (15), one has

$$\phi = 2\pi a^2 K + 4\pi a K \sum_{n=1}^{\infty} \frac{e^{-j_n|z|}}{j_n J_0^2(j_n)} J_0(j_n r) J_1(j_n a) \quad (17)$$

$$\psi = 4\pi a K r \sum_{n=1}^{\infty} \frac{e^{-j_n|z|}}{j_n J_0^2(j_n)} J_1(j_n r) J_1(j_n a) \quad (18)$$

where K is the strength of the vortex.

APPLICATIONS

To facilitate the application of some of the results obtained above, the velocity components and stream function for a point source of one-half unit strength have been evaluated and tabulated in reference 3. The tables of $J_0(jr)$ and $J_1(jr)$ of reference 6 expedite the evaluation of the series for the other source-sink forms.

Point Source in a Uniform Flow

The velocity potential of a point source in a uniform flow in a duct is found by adding the velocity potential Uz for a uniform flow to Eq. (5). To obtain the corresponding stream function, one has to add the term $Ur^2/2$ to Eq. (6). When dealing with semi-infinite bodies, a constant $2m$ must be subtracted from the stream function downstream of the source in order to maintain the usual convention that $\psi = 0$ is the body streamline.

Bodies were calculated for several values of U/m, and are shown in Fig. 2. Important features of the body shape can be found quickly by employing the continuity equation. In the plane of the source, one has, by continuity,

$$U - 2m = U(1 - r_0^2)$$

so that

$$r_0^2 = 2m/U$$

The radius of the body downstream at $z = +\infty$ can also be found through continuity as

$$r_\infty^2 = 2r_0^2/(1 + r_0^2)$$

$$r_\infty^2 = (4m/U)/[1 + (2m/U)]$$

It should be noted that there is a departure from the usual result that the velocity upstream at infinity is just that due to the uniform flow superimposed on the source flow. In this case the upstream velocity is less than the superimposed value by $2m$. Similarly, the velocity downstream at infinity is greater by $2m$.

Doublet in Uniform Flow

The velocity potential for a doublet in a uniform flow can be obtained by adding the velocity potential Uz for a uniform flow to Eq. (7) and the corresponding stream function is found by adding $Ur^2/2$ to Eq. (8).

Bodies calculated for several values of M/U are shown in Fig. 3.

Concluding Discussion

The examples presented above serve to illustrate the forms of bodies obtained by using sources or doublets in a uniform ducted flow. Application of the results obtained to complex body shapes is discussed in reference 3. A preliminary attempt to incorporate the velocity distributions found from a body identical in shape to that of the hub of an axial flow compressor indicates that these results can be used to estimate the inlet velocity profile, hub blockage effects, and other three-dimensional effects.

In building up bodies of arbitrary shape, one can of course utilize any or all of the above source-sink distributions through superposition. However, it should be pointed out that the results above can easily be extended to include the case of varying duct wall contour, by using source-sink forms with $a = 1$ [see Eqs. (9) and (10)]. Thus, many forms of nozzles, diffusers, and ducted bodies can be studied.

References

[1] Barua, S. N., *A Source in a Rotating Fluid*, The Quarterly Journal of Mechanics and Applied Mathematics, Vol. VIII, Part 1, Clarendon Press, Oxford, March, 1955.

[2] Lamb, H., Hydrodynamics, 6th Ed., Dover Publications, New York, 1945.

[3] Levine, P., *Incompressible Potential Flow About Axially Symmetric Ducted Bodies*, WADC TN 57-287, August, 1957.

[4] Smyth, W. R., *Static and Dynamic Electricity*, 1st Ed., McGraw-Hill Book Company, Inc., New York, 1939.

[5] Watson, G. N., *Theory of Bessel Functions*, 2nd Ed., The MacMillan Company, New York, 1945.

[6] Harvard Computation Laboratory, *Design and Operation of Digital Calculating Machinery—Progress Report #41*, Cambridge, Mass, August, 1955.

Hydrodynamics and Heat Conduction of a Melting Surface

(*Continued from page 32*)

B.t.u./ft.^{2}-sec., simple melting theory indicates that close to steady-state melting is achieved one to two seconds after the start of melting; this has been verified experimentally. Hence the method can be used for the case of slowly varying external conditions.

In order to apply the results to an actual case, m_i, u_i, T_i, q_i, and τ_i must be matched with the boundary-layer solution. However, calculations have been performed which employed estimates of the aerodynamic heat-transfer rate. The results indicate that the melting rate is sufficiently small so that this method of surface protection may be practical for certain applications.

Conclusions

For the case considered, it appears necessary to include the effect of the liquid film in order to accurately determine the rate at which a surface recedes due to melting from aerodynamic heating. Additional solutions are required to determine the general behavior of melting films in order to solve the transient case, which is the one of greatest technical interest.

References

[1] Landau, H. G., *Heat Conduction in a Melting Solid*, Q. Appl. Math, Vol. 8, No. 1, pp. 81–94, January, 1950.

[2] Pai, S., *Viscous Flow Theory—I Laminar Flow*, D. Van Nostrand Co., Princeton, 1956.

[3] Lees, Lester, *Laminar Heat Transfer Over Blunt-Nosed Bodies at Hypersonic Flight Speeds*, Jet Propulsion, Vol. 26, No. 4, pp. 259–269, 274, April, 1956

[4] Tsien, H. S., *Notes on Physical Mechanics*, California Institute of Technology, 1954.

[5] *Properties of Selected Commercial Glasses*, Corning Glass Works, Bulletin B-83, 1949.

[6] Li, Ting-Yi, and Geiger, R. E., *Stagnation Point of a Blunt Body in Hypersonic Flow*, Journal of the Aeronautical Sciences, Vol. 24, No. 1, pp. 25–32, January, 1957.

The Crippling Strength of Compression Elements

GEORGE GERARD**
New York University

SUMMARY

This paper consists of a review, primarily for the air-frame designer and stress analyst, of a new method of crippling strength analysis. Available test data on various aluminum, magnesium, and titanium alloys and steels are presented in terms of generalized parameters, based on the overall geometric configuration of the element and two mechanical properties of the material—the elastic modulus and compressive yield strength. The method applies to both formed and extruded elements and stiffened panels.

The predictions of the method are checked by available test data on short-time crippling at elevated temperatures. Similarly, the method is extended to the creep crippling problem by a suitable definition of the time-dependent yield strength under creep conditions.

Finally, the efficiencies of various materials in crippling applications under elevated temperature conditions are reviewed and simple test methods are proposed for rapidly determining the crippling strength of new materials under various environmental conditions.

SYMBOLS

Wrought Alloy Designation*

Alloy	Former	New
Aluminum	14S	2014
	R301	2014
	17S	2017
	24S	2024
	52S	5052
	61S	6061
	75S	7075
Magnesium	FS-1, FS1	AZ31B
	0-1, 01	AZ80A

Temper Designations*

Alloy	Former	New	Conditioning
Aluminum	-0	-0	annealed
	-T	-T3	heat treated
	-T	-T4	extruded and heat treated
	-T	-T6	heat treated and aged
	-RT	-T36	heat treated and rolled
	-1/4 H	-H32	one-quarter hard
Magnesium	h	-H24	hard rolled
	HTA	-T5	extruded and aged

* NOTE: The alloy and temper designations used herein refer to the designation in use at the time the test data were obtained.

Notation

A = area of element; area of stiffener plus sheet of width, b_s, in.^{2}
b = total width of stiffened panel, in.
b_s = width of sheet between stiffeners, in.
b_w = web width, in.
E = modulus of elasticity, psi
f = cladding thickness as a fraction of total plate thickness; form factor
g = number of cuts plus flanges
m = exponent
N = compressive loading, lbs./in.
R = radius, in.
t = thickness, in.
t_f = time for creep crippling, hours
$[t]$ = function of time
w = weight per unit length, lbs./in.
α = crippling coefficient
β = crippling coefficient for two corner elements
β_g = generalized crippling coefficient based on g
$\bar{\eta}$ = cladding reduction factor; $\bar{\eta} = [1 + 3(\sigma_{cl}/\sigma_{cr})f]/(1 + 3f)$
$\bar{\sigma}_a$ = applied creep stress, ksi
σ_{cl} = cladding yield strength, ksi
σ_{cr} = buckling stress, ksi
σ_{cy} = compressive yield strength, ksi
$\bar{\sigma}_f$ = crippling strength, ksi
φ = density, pci

Subscripts and Superscripts

s = skin
w = stiffener web
$\bar{}$ = effective or weighted value

INTRODUCTION

THE INTRODUCTION and proper selection of many new materials in air-frame design under room temperature conditions and both short time and creep conditions under elevated temperatures has placed an urgent requirement on the acquisition of strength data. One of the most basic of these data in air-frame analysis and design is crippling strength. Consequently, it appeared that a fruitful approach would be a comprehensive review of available test data to arrive at a semiempirical method of sufficient generality and simplicity that it could be applied with reasonable confidence to the prediction of the crippling strength of materials, both old and new, under various conditions of temperature and time.

The purpose of this paper is to review a new method of crippling strength analysis which has resulted from an extensive investigation of room temperature crippling data on flanges, plates, angles, Z, channels and multicorner sections and stiffened panels, both formed and extruded.[1, 2, 3] The review herein consists primarily of a presentation of the test data in terms of certain generalized parameters which reflect the overall geometric configuration of the element and only two mechanical properties of the material, E and σ_{cy}.

Received May 7, 1957.

** Assistant Director, Research Division, College of Engineering.

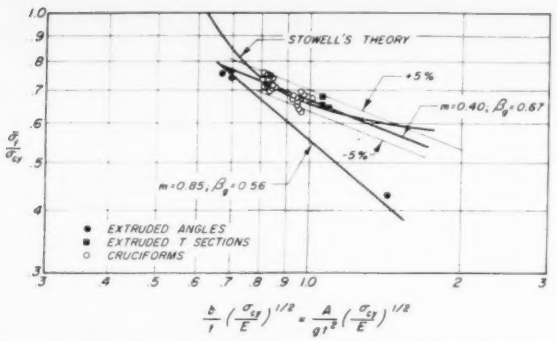

FIG. 1. Crippling data on 24S-T flange elements (references 4, 8, 9).

The aim is to present the method and data for use of the designer and stress analyst and therefore the details of the development of the method are omitted. In cases where the development is of interest, refer to references 1 and 2.

Most crippling methods in current use involve subdivision of the cross section of the formed section into a series of plates[4] or angle sections.[5] The crippling strength of the section is obtained as a weighted average of the crippling strengths of the subdivided elements. The method described herein is empirical in nature, as are the other methods, but does not require the subdivision of the cross section into elements for analysis. The only geometric parameter required for the analysis is the developed length-thickness ratio, A/t^2. In a sense, the method is a generalization of the work of Schuette,[6] Gallaher,[7] and Needham[5] on formed sections.

(1) ROOM TEMPERATURE

THEORY AND EXPERIMENTS ON FLANGES AND PLATES

It is a well known phenomenon that the failing strength of a flat plate can appreciably exceed the buckling stress when the latter occurs in the elastic range. This behavior results from the boundary constraints at the unloaded edges of the plate which permit significant tension stresses to develop in the plane of the plate after buckling.

Crippling of Flanges

A hinged flange is the simplest element, from the standpoint of analysis, which can carry loads considerably in excess of the elastic buckling load. As compared to a column which is unsupported along the unloaded edges and thus deflects appreciably at buckling, the flange is supported along one unloaded edge. This boundary constraint tends to stiffen the flange during postbuckling rotation and permits postcritical loads to be carried.

Because of the nonlinearity of the postcritical behavior and the additional nonlinearities of plasticity, failure analyses of buckled elements are complex. Fortunately, Stowell[8] has succeeded in conducting a failure analysis of a flange with a simply supported, straight unloaded edge. These results are of considerable importance because they supply quantitative data as to the failure mechanism. Furthermore, the analysis provides a reference frame from which semiempirical methods can be devised to treat other cases of failure for which complete analyses do not exist.

TABLE 1
Test Data on Extruded Angle and T-Sections

Ref.	Shape	A/t^2	σ_{cy}	$\bar{\sigma}_f/\sigma_{cy}$	$.1\left(\frac{\sigma_{cy}}{E}\right)^{1/2}/gt^2$
Angle Sections[a]					
4	LS 208	21	43 ksi	0.754	0.67
4	LS 209	22	43	0.737	0.70
4	LS 210	22	43	0.764	0.70
9	6	46.1	42.4	0.43[b]	1.44
T-Sections[a]					
4	LS 236	38.5	43	0.721	0.82
4	LS 247	50	43	0.680	1.06
4	LS 248	50	43	0.652	1.06
4	LS 249	39	43	0.750	0.83
9	7	49.6	40.4	0.65[b]	1.09

[a] In the extrusion fillets for angles, $0 < R/t < 1/2$; for T-sections, $1/2 < R/t < 1$.
[b] Values of $\bar{\sigma}_f/\sigma_{cy}$ correspond to an $L'/\rho = 20$.

The very significant physical fact which is brought out by this analysis is that the edge stress is intimately associated with failure. Apparently failure occurs when the stress intensity at the edge reaches a value approximately equal to the compressive yield strength. This is indicated by Stowell's analysis where it is shown that, for eight widely different hinged flanges, the edge stress intensity is a constant within one per cent of the compressive yield strength.

The results of the analysis which are important from a design standpoint are shown in Fig. 1. It can be observed that Stowell's theoretical curve is in good agreement with test data on 24S-T4 aluminum alloy cruciform extrusions. In such sections, the opposed flanges constrain the simply supported unloaded edges to remain straight. For equal flange angles, however, the simply supported unloaded edges warp in the plane of the flange after buckling. Consequently, the test data for extruded angles given in Table 1 lie below Stowell's theoretical line which pertains to an undistorted unloaded edge. The test data for extruded T-sections given in Table 1 and shown in Fig. 1 follow the trend line for the cruciform sections.

The choice of parameters used for the coordinates of Fig. 1 is given in some detail in references 1 and 2. For purposes of completeness however, a brief development follows. Schuette[6] has shown quite convincingly that the results of crippling tests on Z, channel, and H extrusions may be represented in the following form:

$$\bar{\sigma}_f/\sigma_{cr} = \alpha\,(\sigma_{cy}/\sigma_{cr})^n \qquad (1)$$

In fact, Stowell utilized the stress parameters of Eq. (1), $\bar{\sigma}_f/\sigma_{cr}$ and σ_{cy}/σ_{cr} in plotting the results of his theory.

By using the relation for the critical stress

$$\sigma_{cr} = KE\,(t/b)^2 \tag{2}$$

Eq. (1) can be converted into

$$\bar{\sigma}_f/\sigma_{cy} = \alpha K^{1-n}[(t/b)\,(E/\sigma_{cy})^{1/2}]^{2(1-n)} \tag{3}$$

In a simplified form

$$\bar{\sigma}_f/\sigma_{cy} = \beta[(t/b)\,(E/\sigma_{cy})^{1/2}]^m \tag{4}$$

Eq. (4) contains the parameters used in Fig. 1 and gives the crippling strength directly in terms of the geometric properties and mechanical properties of the section.

From Fig. 1, the following values are obtained for flange elements for $\bar{\sigma}_f/\sigma_{cy} \leq 0.8$:

unloaded edge	m	β
straight	0.40	0.67
distorted	0.85	0.56

(5)

The empirical values for the straight unloaded edge flange fit the theory and test data reasonably well. The values selected for the distorted edge case are based on the few test data for angles as well as considerable other evidence presented in the subsequent sections.

For flanges that cripple in the inelastic range $\bar{\sigma}_f/\sigma_{cy} > 0.8$, test data[6] conclusively indicate that buckling and failure are essentially coincident. Therefore,

$$\bar{\sigma}_f = \sigma_{cr}; \quad \text{for} \quad \bar{\sigma}_f/\sigma_{cy} > 0.8 \tag{6}$$

Crippling of Plates

As indicated previously, the failure analysis of buckled plates is mathematically complex. By use of variational principles in conjunction with calculations performed on an electronic computer, Mayers and Budiansky[10] were able to obtain results related to failure of buckled plates.

The load-carrying capacities of flat plates with unloaded edges constrained to remain straight were computed for 24S-T3 plates that buckle elastically at prescribed fractions of the compressive yield strength. Although the average compressive stress did not have a maximum value in the range of end shortening considered, the curves were very flat from a strain of approximately 0.006 on. Thus, the average compressive stress at a strain of 0.010 was taken as an indication of failure.

The results of this analysis, together with experimental data on failure of flat plates, are shown in Fig. 2. A very significant fact brought out by the theoretical analysis is that the load-carrying ability of plates with straight unloaded edges may be significantly higher than plates with unloaded edges which are free to warp.

In discussing the failure of flat plates and flanges, it is necessary to identify differences in boundary conditions which by themselves may not cause a difference in buckling stress: (a) the unloaded edges do not warp and remain straight in the plane of the plate (v = const., Fig. 3a), and (b) the unloaded edges are free to warp in the plane of the plate ($\sigma_y = 0$, Fig. 3b).

Plates tested in V-groove supporting fixtures are free to warp. In addition, out-of-plane displacements at the unloaded edges are not entirely prevented after buckling due to lateral shortening in the central region of the plates, as shown in Fig. 3. Similarly, the post-buckling behavior of compressed square tubes closely follows that of plates tested in V-groove supports. For the tubes, both warping and out-of-plane displacements of the corners are evident after failure.

The parameters used in Fig. 2 are the same as those used in Fig. 1 with the exception that the g term is introduced in the abscissa coordinate. As illustrated in Fig. 4, g represents the number of flanges and cuts required to reduce the section to a series of flange elements. This scheme is quite arbitrary and has the virtue that results on many different sections can be reduced to one crippling equation by its use, as will be shown herein.

The results for angle sections when presented in terms of b/t are already in the desired form, since, for the flange,

$$b/t = A/2t^2 = A/gt^2 \tag{7}$$

Thus, Eq. (4) becomes

$$\bar{\sigma}_f/\sigma_{cy} = \beta_g[(gt^2/A)\,(E/\sigma_{cy})^{1/2}]^m \tag{8}$$

The values for m and β given in Eq. (5) now apply for the flange for the g-correlation scheme.

For the V-groove plates and square tubes, $g = 3$ and 12, respectively, as shown in Fig. 4. The results shown in Fig. 2 indicate the following values for plate elements:

unloaded edges	m	β_g
straight	0.40	0.65
distorted	0.85	0.56

(9)

It can be observed that these values for plate elements are in substantially good agreement with the values given by Eq. (5) for flange elements.

Crippling of H Sections

Rather extensive test data on H extrusions of four aluminum alloys and one magnesium alloy[6, 12] are available to test further the g-correlation scheme. As shown in Fig. 4, $g = 7$ for an H extrusion. The test data correlated according to the parameter A/gt^2 are illustrated in Fig. 5. It can be observed that satisfactory correlation with Eq. (8) is obtained by utilizing the β_g value for cruciform, Eq. (5) straight unloaded edges, for $\bar{\sigma}_f/\sigma_{cy} \leq 0.8$. As discussed previously, beyond this cutoff Eq. (6) applies.

The value of $m = 0.40$ obtained for the H sections is the same as that for flanges and flat plates with straight unloaded edges. Evidently, the opposed flanges of the H section prevent any warping of the flanges at the corner.

From the results presented in Figs. 1, 2, and 5, it appears that the g-correlation scheme permits an integrated approach to the crippling strength analysis of

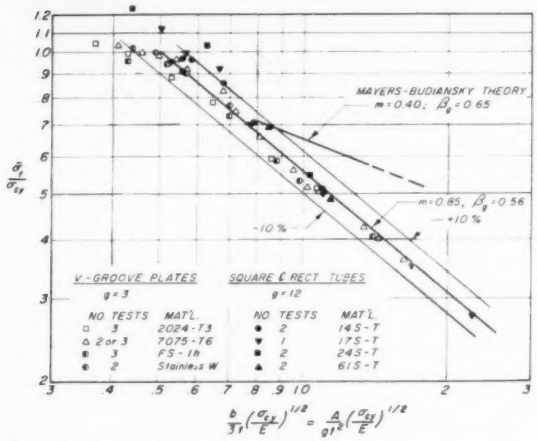

FIG. 2. Crippling data on plate elements (reference 1).

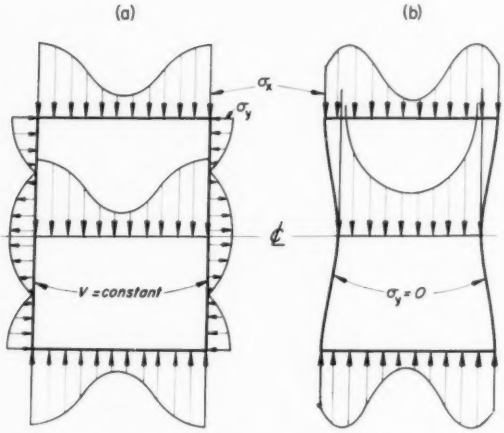

FIG. 3. Stresses and displacements of flat plates after buckling under conditions of uniform end shortening (reference 11). (a) Straight unloaded edges, (b) stress free unloaded edges free to warp in the plane of the plate.

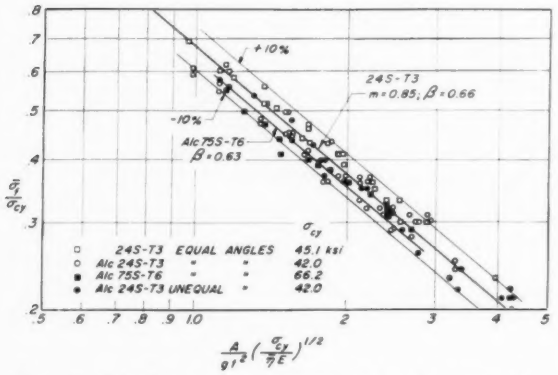

FIG. 6. Crippling data on formed angles (reference 5).

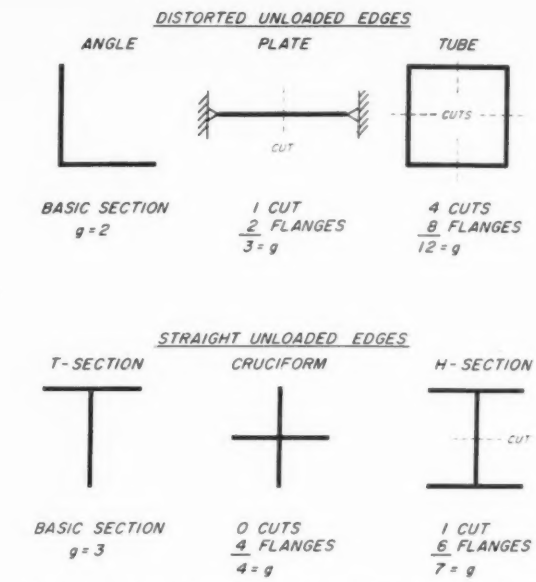

FIG. 4. Method of cutting simple elements to determine g.

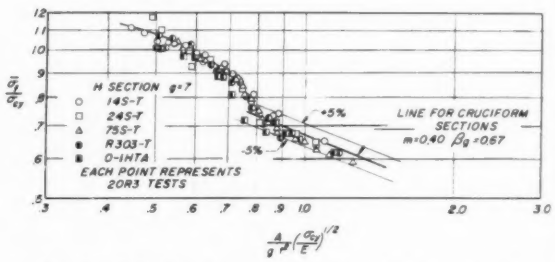

FIG. 5. Crippling data on H extrusions (references 6, 12).

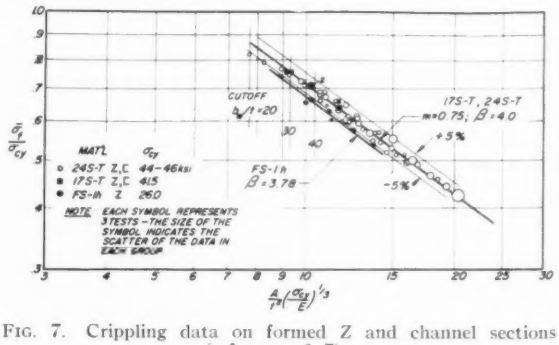

FIG. 7. Crippling data on formed Z and channel sections (references 6, 7).

the extruded and machined flanges and plate elements considered.

Formed and Extruded Sections

The crippling strength of formed and extruded sections is associated with the short column region (L'/ρ approximately less than 20) where the strength does not vary significantly with the length of the stiffener. The various factors influencing crippling of flange and plate elements also pertain to formed sections. Additional factors such as the increased stress-strain characteristics in the corner region as a result of forming influence the crippling strength of formed sections. Also, sections are often formed of Alclad sheet and it is necessary to consider the effect of the cladding upon the crippling strength.

Formed Angles

Needham[5] has conducted tests on crippling of equal flange angles formed in the -T condition to an inside radius approximately equal to $3t$, and the test data are shown in Fig. 6 according to the parameters of Eq. (8). The empirical constants for Eq. (8) which fit the data within ±10 per cent limits are

material	m	β_g	
24S-T3	0.85	0.66	
Alclad 24S-T3	0.85	0.66	(10)
Alclad 75S-T6	0.85	0.63	

The β_g values differ somewhat due to different strain-hardening characteristics in the formed corners; an effect discussed in a subsequent section.

Two Corner Sections

For two corner sections such as Z and channel sections, the buckling coefficient is a function of b_f/b_w. Consequently, it was found[1] that the development leading to Eqs. (4) and (8) does not hold for two corner sections where the flange elements apparently influence significantly the crippling strength. The analysis of a large mass of test data presented in reference 1 indicate that the following form of Eq. (8) applies for two corner sections:

$$\bar{\sigma}_f/\sigma_{cy} = \beta \left[\frac{t^2}{A}\left(\frac{\bar{\eta}E}{\sigma_{cy}}\right)^{1/3}\right]^{0.75} \qquad (11)$$

The test data for several materials[6, 7] correlated according to Eq. (11) are shown in Fig. 7. The following values of the crippling coefficient, β, fit these data within ±5 per cent limits:

material	β	
17S-T	4.00	
24S-T	4.00	(12)
FS-1h	3.78	

The lower value of β for the FS-1h magnesium alloy is attributed to lower strain hardening characteristics in the formed corners, as discussed subsequently. Beyond the cutoffs shown in Fig. 7, Eq. (6) applies.

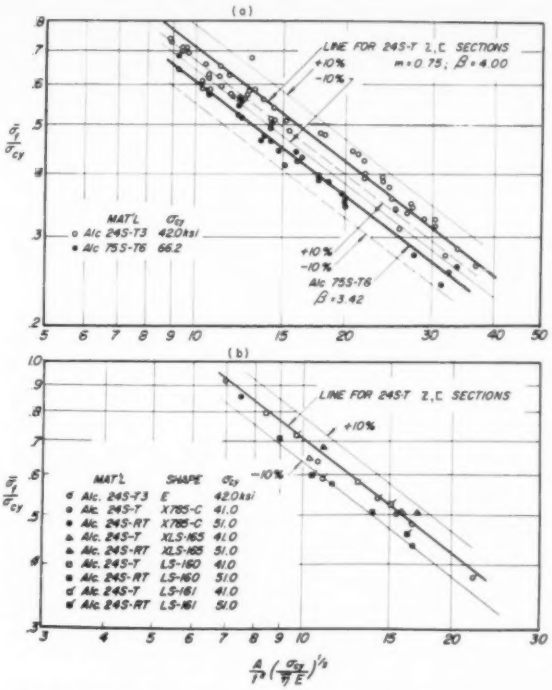

FIG. 8. Crippling data on formed Z and channel sections (references 4, 5). (a) Alclad sections, (b) unequal flanged Z and J sections.

In reference 1 a mass of test data on extruded Z and channel sections with filleted corners of $R/t = 1$ correlated according to Eq. (11) with $\beta = 3.64$. The corner fillet apparently influences the crippling strength somewhat by delaying the extension of the buckles through the corners which occurs at failure.

TABLE 2
Test Data on Two-Corner Elements

Ref.	Shape	t	A/t^2	σ_{cy}	$\bar{\sigma}_f/\sigma_{cy}$	$\frac{A}{t^2}\left(\frac{\sigma_{cy}}{\bar{\eta}E}\right)^{1/2}$
5	E1	0.0252 in.	136.7	42 ksi	0.376	22.10
	E2	0.0253	87.2	42	0.538	14.10
	E3	0.0504	67.6	42	0.588	10.92
	E4	0.0255	95.5	42	0.500	15.45
4	X785-C	0.025	103	41	0.478	16.52
		0.040	64.5	41	0.639	10.68
		0.064	40.3	41	0.920	6.93
		0.025	103	51	0.431	16.67
		0.040	64.5	51	0.573	11.47
		0.064	40.3	51	0.853	7.45
4	XLS-165	0.025	99.4	41	0.505	15.94
		0.040	62.1	41	0.648	10.28
		0.025	99.4	51	0.502	17.12
		0.040	62.1	51	0.680	11.02
4	LS-160	0.025	80.8	41	0.578	12.97
		0.040	50.5	41	0.790	8.36
		0.025	80.8	51	0.507	13.92
		0.040	50.5	51	0.704	8.98
4	LS-161	0.025	93.6	41	0.525	15.03
		0.040	58.5	41	0.715	9.68
		0.025	93.6	51	0.455	16.15
		0.040	58.5	51	0.596	10.40

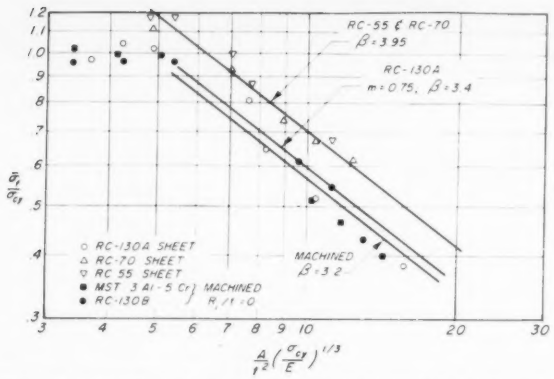

FIG. 9. Crippling data on formed and machined channels (reference 16).

Alclad Correction

The cladding which may be present on formed sections acts to reduce the value of the buckling stress and therefore its principal effect is reflected in the cladding reduction factor, $\bar{\eta}$. Needham[5] has presented a considerable amount of test data on Alclad channel sections and thus the data of Fig. 7 on 24S-T Z and channel sections can be used as a standard of comparison with Needham's Alclad 24S-T3 data to substantiate the method of correcting for the cladding.

The cladding correction factor $\bar{\eta}$ can be computed from the following formula, given in reference 1:

$$\bar{\eta} = [1 + 3(\sigma_{cl}/\sigma_{cr})f]/(1 + 3f) \qquad (13)$$

where f is the ratio of total cladding thickness to total thickness ($f = 0.10$ for Alclad 24S-T3 and $f = 0.08$ for Alclad 75S-T6).

Needham's test data are presented in the upper portion of Fig. 8 and compared with the value of $\beta = 4.00$ obtained from the 24S-T data of Fig. 7. It can be seen that the data fall within the ±10 per cent scatter band. Inasmuch as Needham's data scattered within ±10 per cent limits (Figs. 6 and 8) the method of correcting for the Alclad coating appears to be satisfactory.

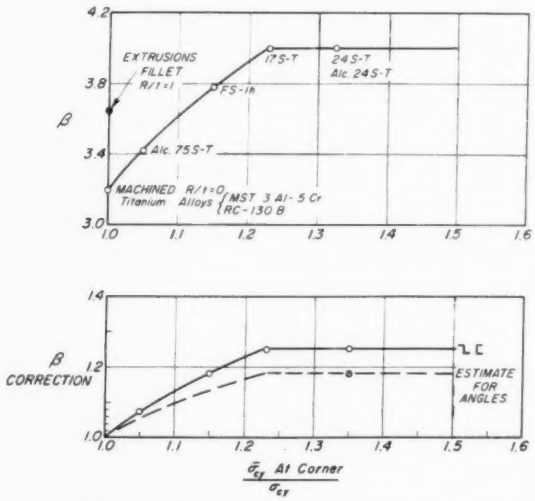

FIG. 10. Influence of $\bar{\sigma}_{cy}$ at corner upon β for formed Z and channel sections.

TABLE 3
Variation of β With $\bar{\sigma}_{cy}/\sigma_{cy}$ Effect

Material	R/t	$\bar{\sigma}_{cy}/\sigma_{cy}$	β	$\beta/3.2$	Source
Z and Channel Sections					
Machined MST 3A1-5Cr RC-130B	0	1.00	3.20	1.00	Fig. 9
All extrusions	1 fillet	1.00	3.64	1.14	Ref. 1
Alc. 75S-T6	3	1.05 (est.)	3.42	1.07	Fig. 8
FS-1h	4.3	1.15	3.78	1.18	Fig. 7
17S-T	3	1.23	4.00	1.25	Fig. 7
24S-T	3	1.35	4.00	1.25	Fig. 7
Alc. 24S-T3	3	1.35 (est.)	4.00	1.25	Fig. 8
RC-130A	3		3.40		Fig. 9
C-110M	4		3.54		Fig. 19
RC-55	3		3.95		Fig. 9
RC-70	3		3.95		Fig. 9
Angles	R/t	$\bar{\sigma}_{cy}/\sigma_{cy}$	β_g	$\beta_g/0.56$	
24S-T extrusions	0–1/2 fillet	1.00	0.56	1.00	Fig. 1
24S-T3	3	1.35 (est.)	0.66	1.18	Fig. 6
Alc. 24S-T3	3	1.35 (est.)	0.66	1.18	Fig. 6
Alc. 75S-T6	3		0.63		Fig. 6
C-110M	4		0.63		Fig. 18

The Alclad 75S-T6 data in Fig. 8 fall consistently below the Alclad 24S-T3 data. These data are fitted within ±10 per cent limits by Eq. (11) with a value of $\beta = 3.42$. The lower strain hardening characteristics of Alclad 75S-T6 appear to be responsible for the lower value of β.

In the lower portion of Fig. 8, test data of Table 2 on unequal flange channels[5] and J sections[4] are presented in terms of the parameters of Eq. (11). It can be observed that the available data correlate within ±10 per cent limits with the line for equal flange Z and channel sections of Fig. 7. Although this relatively simple method of analysis requires substantiation by considerably more test data than presented, the available test data indicate that two corner elements tend to behave in the same manner regardless of their shape.

Increased Corner Properties

The increased corner properties of sections which are formed in the -T condition have been discussed briefly at various points. Now that the values of β in Eq. (11) have been established for formed Z and channel sections of several different materials, it is possible to examine quantitatively the effects of the increased corner properties on crippling.

The average compressive yield strength, $\bar{\sigma}_{cy}$, of the corners of Z and channel sections as compared to the unformed sheet has been investigated by Heimerl and Roy[13] for 17S-T, Heimerl and Woods[14, 15] for 24S-T and Alclad 75S-T, and Gallaher[7] for FS-1h. The ratios of the average compressive yield strength of the corner, $\bar{\sigma}_{cy}$, for these materials are presented in Table 3, together with the value of β obtained herein on formed and extruded sections.

Also given in Table 3 are some recent test data on titanium alloy channel sections as presented in Fig. 9. These data are particularly valuable since they include machined channel sections with no fillet radius in the corner, which then serve as a lower bound for the corner effect.

It can be observed that all of the β values for two corner sections given in Table 3 lie between 3.2 and 4.0. The data are plotted as a function of $\bar{\sigma}_{cy}/\sigma_{cy}$ in Fig. 10 and indicate a fairly consistent trend. By using $\beta = 3.2$ as a lower limit, a correction factor for the corner effect is also given in Fig. 10. The increased properties in the formed corners can apparently raise the value of β for two corner sections by as much as 25 per cent.

Also given in Table 3 are the available data for angles. The data are too few to provide other than the estimate for the corner effect given in Fig. 10.

The raised yield effect in the corners of formed sections can result in significant increases in crippling strength. If this effect is considered to be of importance in design, a systematic test program should be conducted to investigate the influence of forming and heat treatment upon the β value.

It has been observed that the corner fillet in extrusions can result in an increase in β. This also requires a systematic investigation.

Multicorner Elements

For convenience, all sections with more than two corners are designated as multicorner elements. Available test data of Needham[5] on multicorner sections of Alclad 24S-T3 formed in the T-condition, and of Crockett[4] on formed Alclad 24S-T and Alclad 24S-RT, are given in Table 4. The available test data are shown in Fig. 11. Lines of slope, $m = 0.85$, fit the data well according to Eq. (8) and the value of $\beta_g = 0.55$ is in close agreement with that obtained for angles, V-groove plates and square tubes. The data are only for the 24S-T material and therefore no conclusions concerning the raised yield effects in the corner can be drawn.

TABLE 4
Test Data on Multicorner Sections

Ref.	Shape	σ_{cy}	$\bar{\sigma}_f/\sigma_{cy}$	$\frac{A}{gt^2}\left(\frac{\sigma_{cy}}{\bar{\eta}E}\right)^{1/2}$	g
5	A1	42 ksi	0.624	0.913	8
	A2	42	0.545	1.028	
	F3	42	0.839	0.615	
	G1	42	0.624	0.916	
	G2	42	0.424	1.445	
5	C1	42	0.412	1.478	11
	C2	42	0.574	0.950	
	C3	42	0.655	0.760	
	C4	42	0.748	0.664	
	C5	42	0.571	0.940	
	F1	42	0.569	0.942	
	F2	42	0.567	0.980	
	D1	42	0.414	1.428	
	D2	42	0.671	0.798	
	D3	42	0.555	0.961	
	D4	42	0.452	1.188	
5	D5	42	0.659	0.793	
4	X 785-D	41	0.537	0.975	
4	X 785-D	51	0.760	0.639	
4	X 785-D	41	0.477	1.088	
4	X 785-D	51	0.710	0.712	
5	H	42	0.595	0.928	14
4	LS-152	51	0.775	0.678	
4	LS-153	51	0.864	0.554	
5	B1	42	0.495	1.128	17
5	B2	42	0.645	0.806	

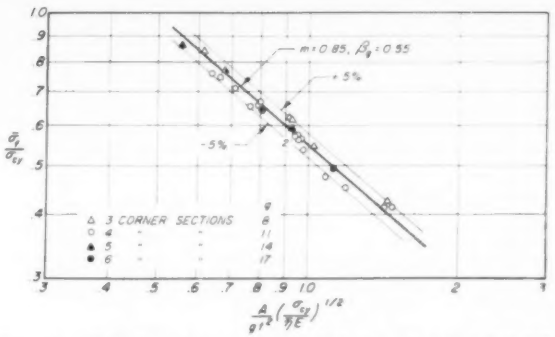

FIG. 11. Crippling data on Alclad 24S-T and Alclad 24S-RT formed multicorner sections (references 4, 5).

STIFFENED PANELS

In analyzing the crippling strength of stiffened panels which consist of formed Z and hat or extruded Y sections attached to a flat sheet, certain additional considerations arise beyond those encountered in the analysis of the stiffener section alone. To avoid consideration of the method of attachment of sheet to stiffeners, it is assumed that the panel is monolithic. Rivet strength requirements to achieve this condition are presented in reference 2.

Z-Stiffened Panels

Test data on the crippling strength of flat stiffened panels with Z-section stiffeners were obtained from three different sets of data listed in Table 5. In the first set, there was a systematic variation in the parameter t_w/t_s. In the second set, nine different materials were used covering a wide range of E and σ_{cy} values. The third group covers potential strength estimates of the highest obtainable crippling strength of a large group of riveted panels. The potential strength of a riveted panel corresponds essentially to the strength of a monolithic panel. In all tests the slenderness ratio of the panel $L'/\rho = 20$.

The cross-sectional area of a stiffened panel is taken as the area of the stiffener plus the area of sheet corresponding to the stiffener spacing. To account for the t_w/t_s variation in the most simple and direct manner, the parameter A/gt^2 for the formed element is replaced by A/gt_wt_s for the stiffened panel. Again this procedure is somewhat arbitrary. It is relatively simple to introduce some weighting factors which may result in a more realistic evaluation of the A/gt^2 parameter for stiffened panels. However, such factors lead to additional complexity and do not improve the correlation sufficiently to warrant their use.

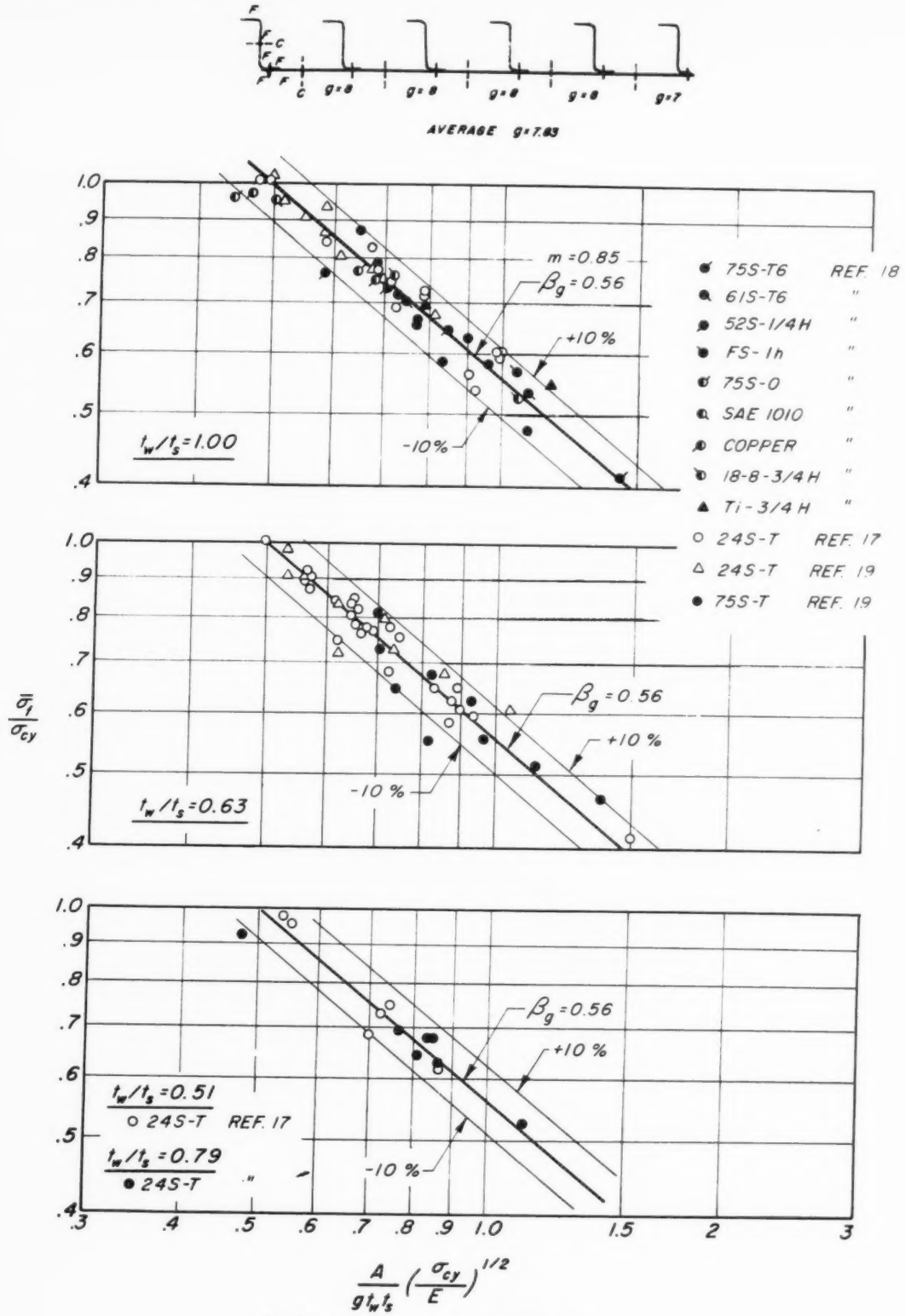

FIG. 12. Crippling data on Z-stiffened panels.

TABLE 5
Crippling Strength Test Data on Stiffened Panels

Ref.	Material	Stiffener	t_w/t_s variation	Remarks
17	24S-T	Z	1.00, 0.79, 0.63, 0.51	strongly riveted panels
18	75S-T6 61S-T6 52S-1/4H 75S-O SAE 1010 Copper FS-1h 18-8-3/4H Ti-1/4H	Z	1.00	data for panels identified as 25-50-20 and 37.5-75-20 used since other panels indicated evidence of wrinkling.
19	24S-T3 75S-T6	Z	1.00, 0.63	potential strength estimates
20	24S-T	hat	1.25, 1.00, 0.63, 0.39	b_h/b_w range of 0.6 to 1.2
21	24S-T 75S-T	Y	1.00, 0.63, 0.40	

The available data on the monolithic crippling strength of formed Z-stiffened panels are shown in Fig. 12 and represent the data from the three sources listed in Table 5 according to t_w/t_s values. Satisfactory correlation is obtained with Eq. (8) in all cases using $g = 7.83$ and $\beta_g = 0.56$. This correlation holds up to values of $\bar{\sigma}_f/\sigma_{cy} = 1$.

Hat-Stiffened Panels

The crippling strength analysis of formed hat-stiffened panels is essentially the same as that used for the Z-stiffened panels. The test data of reference 20 cover a range of b_h/b_w values (b_h = width of top web, b_w = height of side webs) between 0.6 and 1.2 and a range of t_w/t_s as given in Table 5.

The test data for each value of t_w/t_s are shown in Fig. 13. All data correlate well with Eq. (8), although there is a small systematic variation of the β_g value with the parameter t_w/t_s that may be due to the closed form of the hat section.

For the particular riveting used for the hat-stiffened panels there is some evidence of wrinkling at $\bar{\sigma}_f/\sigma_{cy}$ values greater than 0.8, as shown by the dotted lines in Fig. 13. This may account for the somewhat anomalous behavior of the data shown in which the β_g value for the $b_s/t_s = 75$ group is somewhat higher than for the b_s/t_s group of 25, 35, and 50. Because of the suspicion of wrinkling, it is recommended that a cutoff of $\bar{\sigma}_f/\sigma_{cy} = 0.8$ be placed on Eq. (8) for hat-stiffened panels and that caution be exercised in using this equation for $t_w/t_s = 0.39$ panels.

Y-Stiffened Panels

In analyzing the crippling strength of monolithic stiffened panels utilizing extruded Y stringers, certain additional considerations are encountered which have not arisen previously. For the particular Y extrusion used in reference 21, the thickness of the horizontally opposed flanges at the top of the section as shown in Fig. 14 is greater than the other elements in the cross section. Consequently, in determining the effective thickness of the stiffener $\bar{t}_w$, the following method of weighting was used:

$$\bar{t}_w = \Sigma b_i t_i / \Sigma b_i \tag{14}$$

In Eq. (14), b_i and t_i refer to the length and thickness, respectively, of the cross-sectional elements.

Similarly, for the 75S-T panels, the compressive yield strength of the stiffener ($\sigma_{cy} = 78$ ksi) was significantly higher than that of the sheet ($\sigma_{cy_s} = 67$ ksi). The following weighting procedure was used:

$$\bar{\sigma}_{cy} = \{\sigma_{cy_s} + \sigma_{cy_w}[(\bar{t}/t_s) - 1]\}/(\bar{t}/t_s) \tag{15}$$

where $\bar{t}$ is the effective thickness of the stiffened panel.

As a consequence of these weighting procedures, the generalized crippling relation for the Y-stiffened panel has the form

$$\bar{\sigma}_f/\bar{\sigma}_{cy} = \beta_g[(g\bar{t}_w t_s/A)\ (E/\bar{\sigma}_{cy})^{1/2}]^m \tag{16}$$

The test data of reference 21 for the 24S-T and 75S-T panels listed in Table 5 correlated according to the parameters of Eq. (16) for three different $\bar{t}_w/t_s$ ratios as shown in Fig. 14. As for the hat-stiffened panels, the β_g values vary somewhat with the $\bar{t}_w/t_s$ parameter.

In view of the desirability of having one method of crippling analysis as far as possible, the results of the previous sections of this paper are summarized for all elements analyzed according to Eq. (8). All β_g values are given in Table 6, from which it can be observed that they are in substantially good agreement at $\bar{t}_w/t_s = 1.0$. The variation of β_g for hat- and Y-stiffened panels with $\bar{t}_w/t_s$ values other than unity are summarized in Fig. 15 in terms of a β_g correction. It can be observed that the correction is substantially the same for the hat- and Y-stiffened panels.

TABLE 6
Summary of Empirical Values of β_g for Flange and Plate Elements and Stiffened Panels

Element	g		β_g
Distorted Unloaded Edges, $m = 0.85$			
(1) extruded angles	2		0.56[c]
(2) V-groove plates	3		0.56
(3) extruded tubes	12		0.56
(4) formed multicorner sections	8–17		0.55
(5) formed Z panels	7.83		0.56
(6) formed hat panels	16.83	t_w/t_s	
		1.25	0.59[a]
		1.00	0.56[a]
		0.63	0.50[a]
		0.39	0.48[a], [b]
(7) extruded Y panels	18.83	$\bar{t}_w/t_s$	
		1.16	0.56
		0.732	0.51
		0.464	0.48
Straight Unloaded Edges, $m = 0.40$			
(8) straight edge plates (theory)	3		0.65[c]
(9) extruded T	3		0.67[c]
(10) extruded cruciform	4		0.67[c]
(11) extruded H	7		0.67[a]

[a] For $\bar{\sigma}_f/\sigma_{cy} \leq 0.8$.
[b] For $b_s/t_s \leq 50$.
[c] Tentatively, for lack of sufficient test data, for $\bar{\sigma}_f/\sigma_{cy} \leq 0.8$.

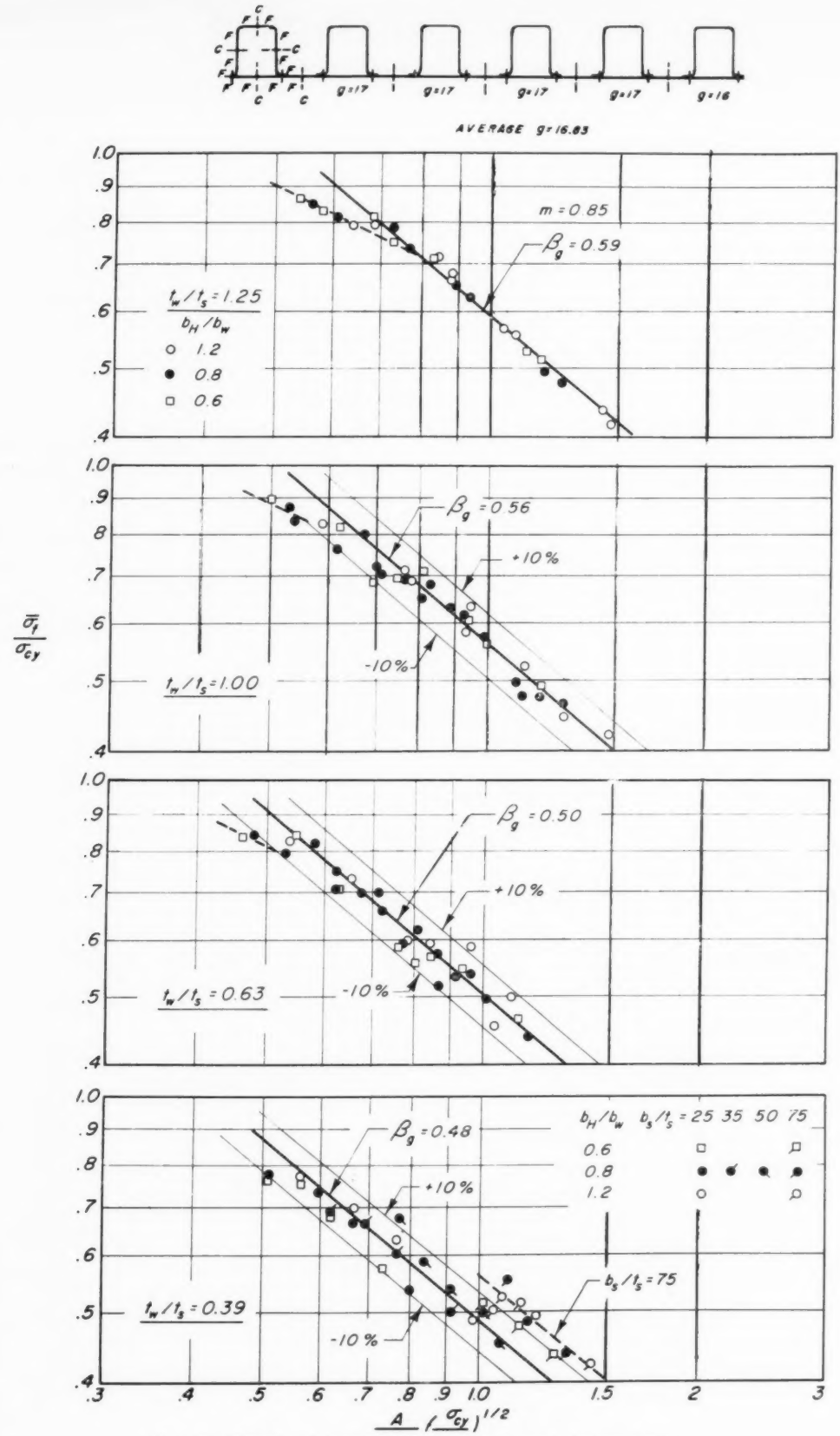

FIG. 13. Crippling data on 24S-T hat-stiffened panels (reference 20).

(2) ELEVATED TEMPERATURES

Short Time Crippling Strength

The rather general method of crippling strength analysis presented in Part (1) apparently is applicable to a wide variety of shapes and materials at room temperature. Because of thermal flight considerations, it is of interest to determine whether the method of analysis can be applied to predicting the crippling strength of various sections under elevated temperature conditions. At such temperatures, time is an important variable and, therefore, it is necessary to consider

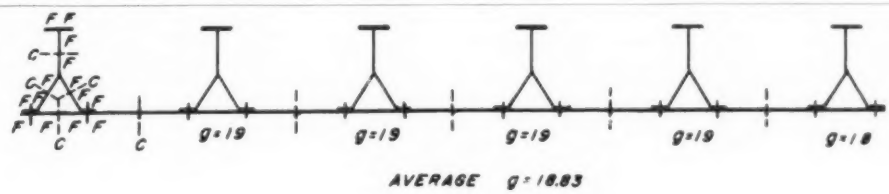

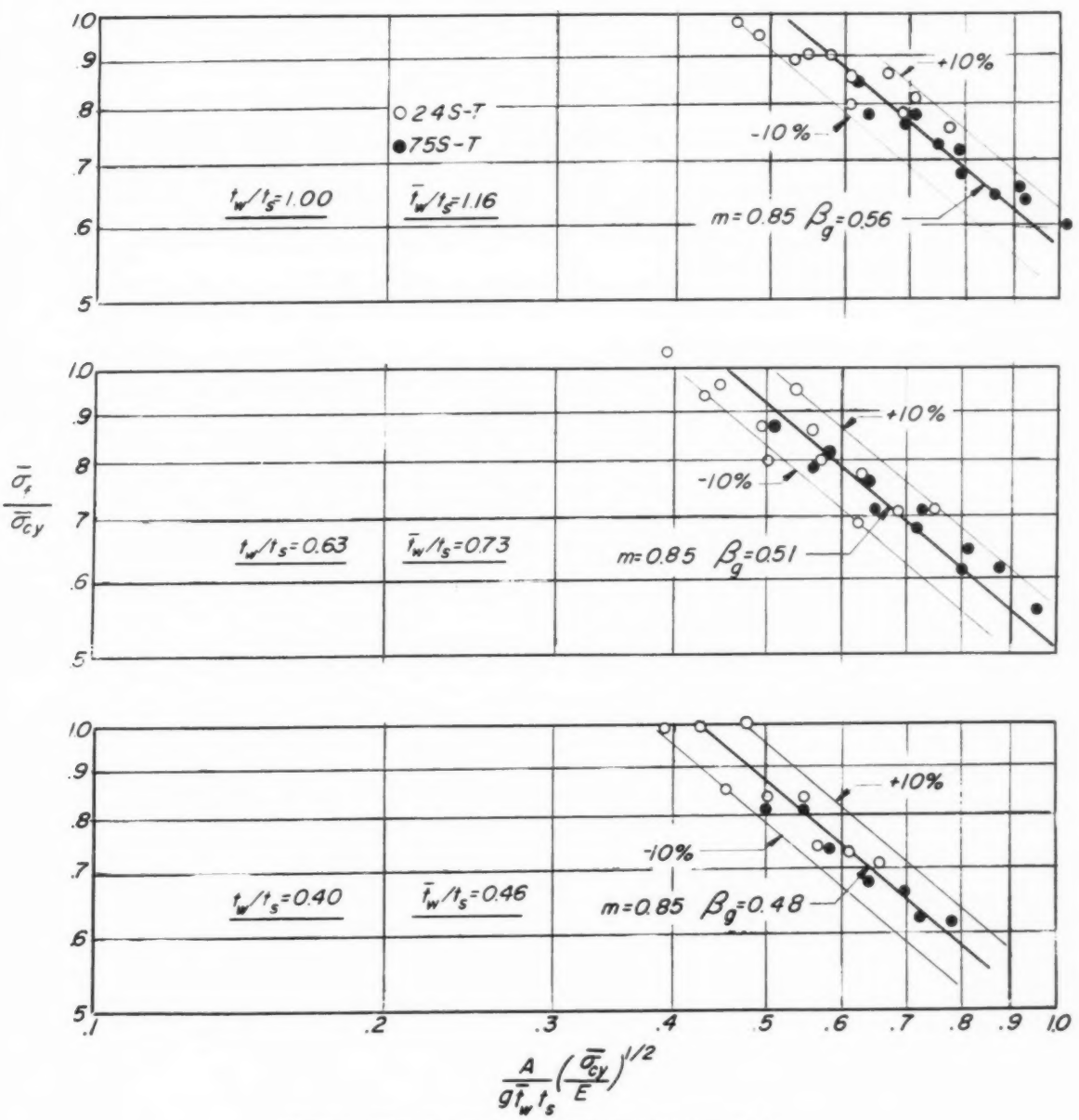

FIG. 14. Crippling data on Y-stiffened panels (reference 21).

short-time crippling strength as well as crippling under creep conditions, or "creep crippling."

Flanges and Plates

A small amount of test data on short-time crippling of H extrusions at elevated temperatures were presented by Heimerl and Roberts.[22] These data are shown in Fig. 16 in terms of the parameters of Eq. (8). Also shown is the line representing the room temperature behavior obtained from Fig. 5 and it can be observed that there is no significant difference in the elevated temperature behavior of the H extrusion in this case.

Some recent test data on the short-time crippling strength of 2024-T3 V-groove plates at elevated temperatures were presented by Mathauser and Deveikis.[23] These data are shown in Fig. 17 in terms of the parameters of Eq. (8) and it is important to observe that there is no significant difference between the elevated temperature and room temperature data.

However, when the value of $\beta_g = 0.56$ obtained from Fig. 2 on other V-groove plates is used, a considerable number of test points fall below the -10 per cent limit. This is particularly true of the room temperature test points which should check with $\beta_g = 0.56$ since this empirical value was established from other V-groove plate tests on 2024-T3. This suggests possibly some defect in the test jig or technique.

A value of $\beta_g = 0.52$ agrees well with the data and all points fall within the 10 per cent limits. Aside from a possible discrepancy resulting from the test technique, it may be concluded that there is no significant difference between the room and elevated temperature test data.

Formed Sections

Short-time crippling data on formed titanium alloy C-110M angles and channel sections are shown in Figs. 18 and 19 in terms of the parameters of Eqs. (8) and (11), respectively. These data were obtained by the Boeing Airplane Company and are given in reference 16.

It can be noted that the room and elevated temperature data follow the same trend. The β_g and β values obtained from Figs. 18 and 19 are listed in Table 3 and it can be observed that the values for C-110M lie within the limits of the β_g and β value obtained for other materials. It is not possible to correlate these data according to the raised yield effect in the formed corners because of the absence of $\bar{\sigma}_{cy}/\sigma_{cy}$ data for these sections. These sections were stress relieved after forming and therefore the raised yield effect is probably small in this case.

Stiffened Panels

Mathauser and Deveikis[24] have recently obtained some data on the short-time crippling strength of Z-stiffened panels of $t_w/t_s = 1.0$ at elevated temperatures. These data are shown in Fig. 20 and again it can be observed that there is no significant difference between the room and elevated temperature data as correlated according to the parameters of Eq. (8). Also shown in Fig. 20 is the room temperature value of $\beta_g = 0.56$ obtained from Fig. 12.

Creep Crippling

The creep crippling phenomenon is concerned with the time required for failure or collapse under a constant creep stress of the various compression elements considered herein. It is distinct from creep buckling in the same sense that short-time crippling is different than short-time buckling when the latter occurs elastically.

It would be desirable if the methods of crippling analysis developed for room temperature, which appear to be applicable under short-time elevated temperature conditions, could be applied to creep crippling. This requires a time-dependent strength property of the material which plays the same role in creep crippling that σ_{cy} does in short-time crippling. Furthermore, in creep crippling, the applied constant creep stress, $\bar{\sigma}_a$, replaces the short-time crippling strength $\bar{\sigma}_f$ and the dependent variable is now the time for failure, t_f.

Method of Analysis

In Part (1), Stowell's analysis of the crippling of flanges indicate that failure occurs when the stress intensity reaches σ_{cy} or a permanent strain of 0.002 in./in. This apparently holds for various types of sections on the basis of the correlation obtained herein using σ_{cy}. Therefore, in the creep crippling analysis, use will be made of this behavior to define a time-dependent strength property to replace σ_{cy}.

An empirical equation which has been used to represent the creep behavior of 2024-T3 aluminum alloy is of the following form:[23]

$$\epsilon = \sigma/E + Ae^{B\sigma}t^K \tag{17}$$

The terms A, B, and K are empirical constants at a given temperature. Denoting the creep stress corresponding to a permanent strain of 0.002 in./in. as $\sigma_{cy}[t]$, as suggested by Mathauser and Deveikis,[23] and noting that, under this condition,

$$\epsilon - \sigma/E = 0.002 \tag{18}$$

Eq. (17) can be transformed into

$$\sigma_{cy}[t] = (1/B) \ln (0.002/At^K) \tag{19}$$

For creep crippling, Eq. (8) becomes

$$\bar{\sigma}_a/\sigma_{cy}[t] = \beta_g \{(gt^2/A)\,(E/\sigma_{cy}[t])^{1/2}\}^m \tag{20}$$

In Eq. (20), $\bar{\sigma}_a$ is the applied creep stress and $\sigma_{cy}[t]$ is obtained from Eq. (19) or from any other creep equation at a permanent strain of 0.002 in./in. at the time for creep crippling, t_f. In a similar manner, Eq. (11) for two corner sections can be derived.

V-Groove Plates

Mathauser and Deveikis[23] have conducted tests on creep crippling of 2024-T3 V-groove plates. Their

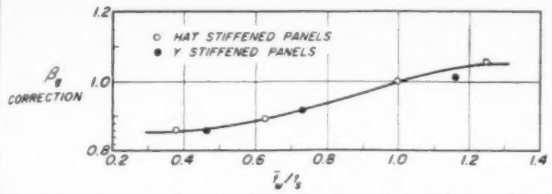

FIG. 15. β_g correction for $\bar{l}_w/l_s$ effect on Y- or hat-stiffened panels.

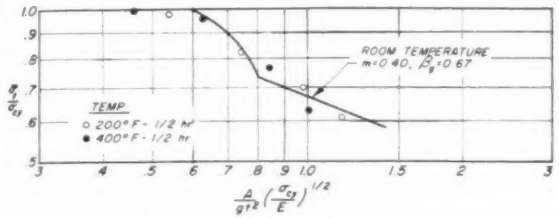

FIG. 16. Crippling data on 75S-T6 H extrusions at elevated temperatures for short times (reference 22).

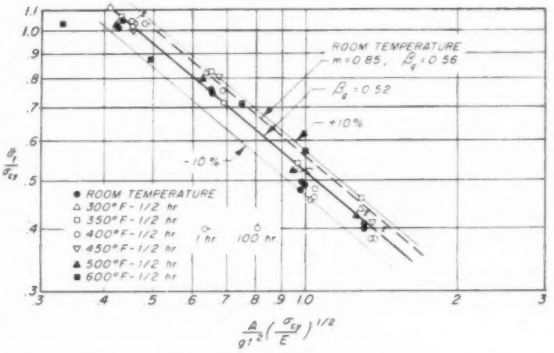

FIG. 17. Crippling data on 2024-T3 V-groove plates at elevated temperatures for short times (reference 23).

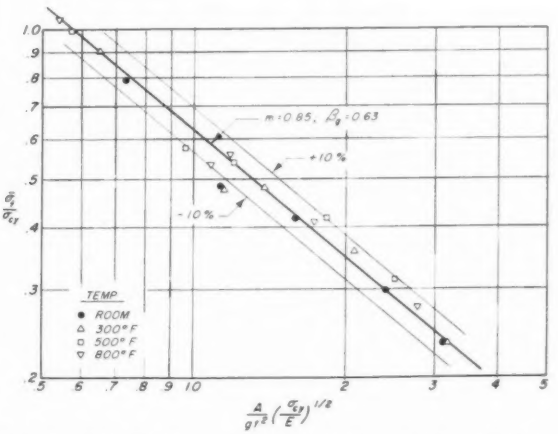

FIG. 18. Crippling data on C-110M titanium alloy formed angles at elevated temperatures for short times (reference 16).

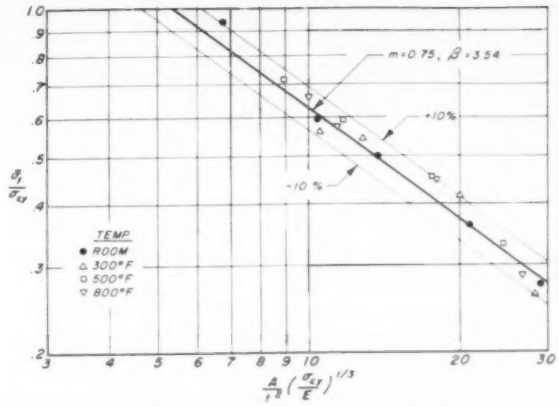

FIG. 19. Crippling data on C-110M titanium alloy formed channels at elevated temperatures for short times (reference 16).

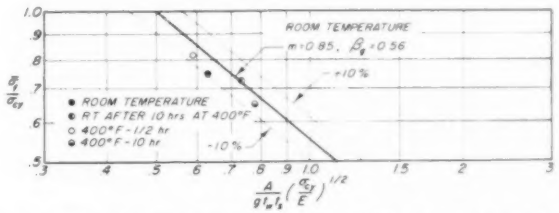

FIG. 20. Crippling data on 2024-T3 Z-stiffened panels at elevated temperatures for short times (reference 24).

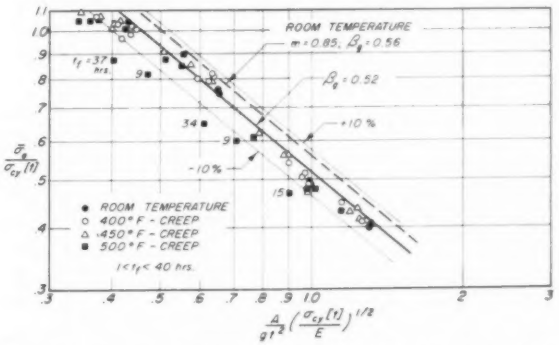

FIG. 21. Creep crippling data on 2024-T3 V-groove plates (reference 23).

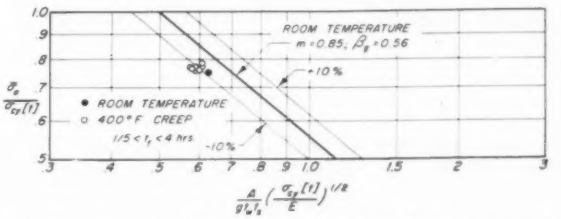

FIG. 22. Creep crippling data on 2024-T3, 4 Z-stiffened panels (reference 24).

test data include $\bar{\sigma}_a$ and the observed t_f for individual plates as well as the pertinent values for the constants A, B, E, and K in Eq. (17). The data are shown in Fig. 21 in terms of the parameters of Eq. (20).

With the exception of the numbered points on the left (the number indicates t_f), there is no significant difference among the creep buckling data and the room temperature test points. The several 500°F. points which are low are for crippling times of 9 hours or more. It is not known whether this discrepancy is due to Eq. (20) or possible inaccuracies in Eq. (17) at 500°F. for times greater than 9 hours.

The value of $\beta_g = 0.52$ in Fig. 21 is directly comparable with that obtained in the short-time crippling tests shown in Fig. 21 using the same test procedures. Thus, the remarks concerning the discrepancy between the room temperature data of Fig. 21 as compared to Fig. 2 pertain here also.

Stiffened Panels

In Fig. 22, some data on creep crippling of Z-stiffened panels tested by Mathauser and Deveikis[24] are shown according to the parameters of Eq. (20). Again it can be observed that there is no significant difference between the room temperature and creep crippling data. Also shown is the room temperature value of $\beta_g = 0.56$ obtained from Fig. 12.

(3) SIGNIFICANCE OF RESULTS IN DESIGN

After having analyzed a relatively large mass of data on various shapes and materials under various environmental conditions, it appears pertinent to summarize the essential results and view them from the broader aspects of the air-frame structure rather than as individual elements.

The values of the crippling coefficients given in the following formulas do not include raised yield effects in the corners of formed sections or fillet effects in extrusion corners. The crippling coefficients are the lowest β and β_g room temperature values presented in Tables 3 and 6. For the sections with distorted unloaded edges considered herein—angles, tubes, V-groove plates, multicorner sections and stiffened panels of $_w/t_s = 1$—the following crippling equation applies within ±10 per cent limits:

$$\bar{\sigma}_f/\sigma_{cy} = 0.56[(gt^2/A)\ (E/\sigma_{cy})^{1/2}]^{0.85} \qquad (21)$$

For the sections with straight unloaded edges considered herein—plates, T, cruciform, and H sections—the following applies within ±5 per cent limits for $\bar{\sigma}_f/\sigma_{cy} \leq 0.8$:

$$\bar{\sigma}_f/\sigma_{cy} = 0.67[(gt^2/A)\ (E/\sigma_{cy})^{1/2}]^{0.40} \qquad (22)$$

For two corner sections—Z, J, and channel sections—the following applies within ±10 per cent limits up to the values of $\bar{\sigma}_f/\sigma_{cy}$ shown in Figs. 7, 8, and 9:

$$\bar{\sigma}_f/\sigma_{cy} = 3.2[(t^2/A)\ (E/\sigma_{cy})^{1/3}]^{0.75} \qquad (23)$$

Beyond the cutoff values of $\bar{\sigma}_f/\sigma_{cy}$, plastic buckling generally occurs, and, therefore,

$$\bar{\sigma}_f = \sigma_{cr} \qquad (24)$$

Corrections for Alclad materials are given by Eq. (13) and β-corrections for the raised yield effect in the corners of two corner sections are given in Fig. 10. For multicorner sections and stiffened panels, the raised yield effect does not appear to be of any significance in the data analyzed herein. For the $_w/t_s$ effect on Y- and hat-stiffened panels, β_g correction factors are given in Fig. 15. In creep crippling problems, σ_{cy} is the creep stress at a permanent strain of 0.002 in./in.

Crippling in Air-Frame Structures

In an air-frame structure, various stiffener shapes are invariably attached to skins, and, therefore, crippling strength estimates such as given by Eq. (23) for two-corner sections are of little practical value. The really significant crippling strength estimate is that of the stiffened panel or V-groove plate which is represented by Eq. (21). This difference in the behavior of a two-corner section when tested alone as compared to when used in a stiffened panel, points up the fact that far too great an emphasis has been placed on crippling tests of Z and channel sections as representative of the crippling behavior of the air-frame structure.

Multicorner sections, square tubes, V-groove plates, and stiffened panels of $_w/t_s = 1$ cripple according to Eq. (21). Thus, it would appear that use of a multicorner section, such as a hat section or a V-groove plate, to determine the crippling strength of a particular material would be much more representative of the air-frame structure than use of a two-corner section.

In addition, test data on the former elements indicate little, if any, $\bar{\sigma}_{cy}/\sigma_{cy}$ effect. In a practical sense, it is generally not possible to take advantage of this effect in design since stiffened sections are either extruded or formed in the annealed or as-quenched condition prior to aging, or else hot formed. These techniques tend to wash out the $\bar{\sigma}_{cy}/\sigma_{cy}$ effect as compared to cold forming in the fully heat-treated condition.

From these considerations, it would appear that, in the design sense, only Eq. (21) is of significance. Since it applies to crippling of V-groove plates and stiffened plates as well as multicorner sections, tests on V-groove plates or simple hat sections would appear to have application to a wide variety of structural applications at room temperature as well as for short-time and creep crippling at elevated temperatures. Since the method is empirical in nature, the value of β_g may possibly vary somewhat from the value of 0.56 for materials and environmental conditions other than those considered herein. Eq. (21) offers the possibility that room temperature data may be extended to various materials and elevated temperature environments and thus reduce the exhaustive tests associated with new materials and environments.

Comparative Crippling Efficiencies

The remarks of the previous section focus particular attention upon Eq. (21) for structural design applications. In such applications, the comparative crippling efficiencies of various configurations and materials particularly at elevated temperatures are of interest. This concluding section, therefore, is devoted to a brief study of crippling efficiencies based on an extension of the methods of references 25 and 26 which were devoted to crippling of plates and multicorner sections.

For efficiency studies, it is necessary to transform Eq. (21) so that it contains the structural index N/b applicable to the crippling strength of V-groove plates and stiffened panels. By use of the following relationships:

$$A = b_s\bar{t}, \quad \bar{t} = N/\sigma_f \tag{25}$$

Eq. (21) can be transformed into

$$\bar{\sigma}_f = (\beta_g\sigma_{cy})^{0.54}\,[f(N/b)\,(E/\sigma_{cy})^{1/2}]^{0.46} \tag{26}$$

where

$$f = g(t_w/t_s)\,(t_s/\bar{t})^2\,(b/b_s) \tag{27}$$

The coefficient f is a form factor where, for a V-groove plate, $f = g$. It can be observed from Eq. (26) that the form factor represents the efficiency of the cross-sectional configuration of stiffened panels in crippling applications.

The weight per unit length of a stiffened panel or plate is simply

$$w = \varphi b\bar{t} \tag{28}$$

By use of Eq. (25), Eq. (26) may be written as

$$wf/b^2 = \varphi[(N/b)/\bar{\sigma}_f] \tag{29}$$

Upon substituting Eq. (26) into Eq. (29), the following weight equation is obtained:

$$wf/b^2 = [(fN/b)/\beta_g]^{0.54}\,(\varphi/E^{0.54})\,(E/\sigma_{cy})^{0.31} \tag{30}$$

If the allowable strength is limited to σ_{cy}, then the following weight equation applies:

$$wf/b^2 = f(N/b)\,(\varphi/\sigma_{cy}); \quad \text{for} \quad \bar{\sigma}_f \geq \sigma_{cy} \tag{31}$$

It can be noted that the weight equations contain the loading index, N/b, and the form factor, f, which are loading and geometric properties. The pertinent material properties are φ, E, and σ_{cy} for crippling strength [see Eq. (30)], and φ and σ_{cy} for compressive strength [see Eq. (31)].

By employing the procedures presented in reference 26 for optimum stiffened panels, a wide variety of magnesium, aluminum, and titanium alloys and precipitation hardened stainless steels have been investigated for crippling efficiencies. By considering the best material in its temperature range for a given alloy class, results are obtained which are representative of the best currently available properties. As discussed in reference 26, an idealized stress strain relation is used in this analysis for which Eq. (30) applies in the elastic range and Eq. (31) in the yield region.

The results of this analysis are shown in Fig. 23, from which it can be seen that the aluminum alloys have a

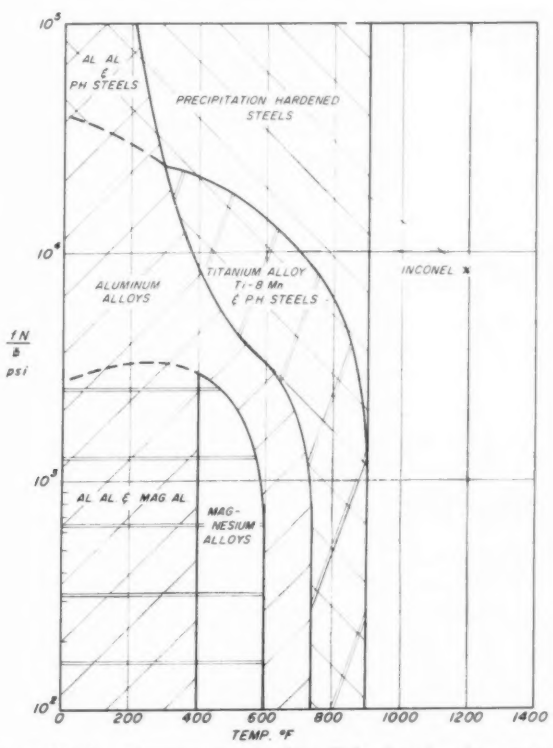

FIG. 23 (*Left*). Comparative crippling efficiencies of various material classes at elevated temperatures for short times.

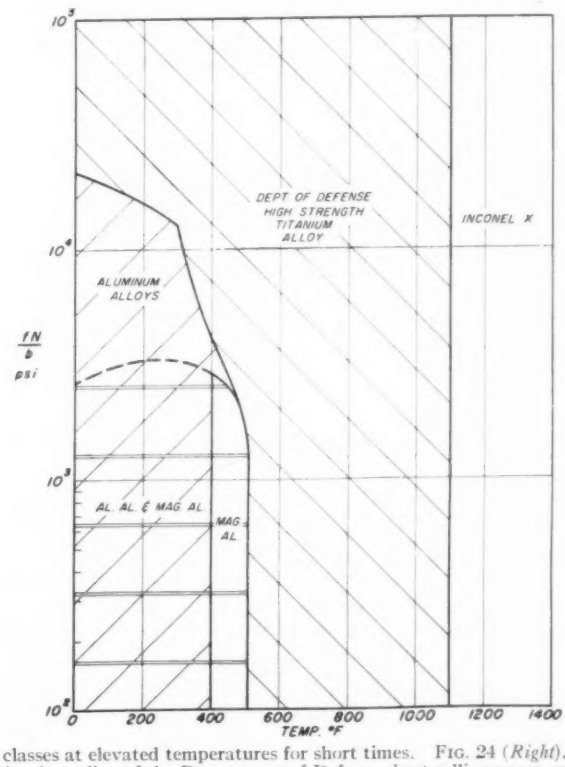

FIG. 24 (*Right*). Potential crippling efficiencies of the new high-strength heat-treatable titanium alloy of the Department of Defense sheet rolling program for short times at elevated temperatures.

wide range of efficient crippling application up to approximately 400°F. Beyond 400°F., particularly at the higher values of the index fN/b, the titanium alloy Ti-8Mn and the precipitation hardened stainless steels are of equal efficiency, except in the highest fN/b range where the precipitation hardened stainless steels are the most efficient.

In Fig. 24, the target properties for high-strength heat-treatable titanium alloy sheet of the Department of Defense Titanium Sheet Rolling Program were used in place of the Ti-8Mn titanium alloy. It can be seen that such an alloy if it can be obtained has a wide range of efficient crippling application particularly above 400°F.

References

[1] Gerard, G., *Handbook of Structural Stability, Part IV—Failure of Plates and Composite Elements*, NACA TN 3784, August, 1957.

[2] Gerard, G., *Handbook of Structural Stability, Part V—Compressive Strength of Flat Stiffened Panels*, NACA TN 3785, August, 1957.

[3] Gerard, G., *Generalized Crippling Analysis of Formed Sections*, Journal of the Aeronautical Sciences, Vol. 23, No. 1, pp. 88–90, January, 1956.

[4] Crockett, H. B., *Predicting Stiffener and Stiffened Panel Crippling Stresses*, Journal of the Aeronautical Sciences, Vol. 9, No. 13, pp. 501–509, November, 1942.

[5] Needham, A., *The Ultimate Strength of Aluminum-Alloy Formed Structural Shapes in Compression*, Journal of the Aeronautical Sciences, Vol. 21, No. 4, pp. 217–229, April, 1954.

[6] Schuette, E. H., *Observations of the Maximum Average Stress of Flat Plates Buckled in Edge Compression*, NACA TN 1625, February, 1949.

[7] Gallaher, G. L., *Plate Compressive Strength of FS-1h Magnesium Alloy Sheet and a Maximum Strength Formula for Magnesium-Alloy and Aluminum-Alloy Formed Sections*, NACA TN 1714, October, 1948.

[8] Stowell, E. Z., *Compressive Strength of Flanges*, NACA TN 2020, January, 1950.

[9] Ramberg, W., and Levy, S., *Instability of Extrusions Under Compressive Loads*, Journal of the Aeronautical Sciences, Vol. 12, No. 4, pp. 485–498, October, 1945.

[10] Mayers, J., and Budiansky, B., *Analysis of Behavior of Simply Supported Flat Plates Compressed Beyond the Buckling Load into the Plastic Range*, NACA TN 3368, February, 1955.

[11] Coan, J. M., *Large-Deflection Theory for Plates with Small Initial Curvature Loaded in Edge Compression*, *J. Appl. Mech.*, Vol. 18, No. 2, pp. 143–151, June, 1951.

[12] Heimerl, G. J., *Determination of Plate Compressive Strengths*, NACA TN 1480, December, 1948.

[13] Heimerl, G. J., and Roy, J. A., *Column and Plate Compressive Strengths of Aircraft Structural Materials—17S-T Aluminum-Alloy Sheet*, NACA ARR No. L5F08, 1945.

[14] Heimerl, G. J., and Woods, W., *Effect of Brake Forming on the Strength of 24S-T Aluminum Alloy Sheet*, NACA TN 1072, May, 1946.

[15] Woods, W., and Heimerl, G. J., *Effect of Brake Forming in Various Tempers on the Strength of Alclad 75S-T Aluminum-Alloy Sheet*, NACA TN 1162, January, 1947.

[16] Jackson, L. R., and Gordon, S. A., *The Application of a New Structural Index to Compare Titanium Alloys with Other Materials in Airframe Structures*, *Trans. ASME*, Vol. 79, No. 5, pp. 949–958, July, 1957.

[17] Gallaher, G. L., and Boughan, R. B., *A Method of Calculating the Compressive Strength of Z-Stiffened Panels that Develop Local Instability*, NACA TN 1482, 1947.

[18] Dow, N. F., Hickman, A., and Rosen, B. W., *Data on the Compressive Strength of Skin-Stringer Panels of Various Materials*, NACA TN 3064, 1954.

[19] Dow, N. F., and Hickman, W. A., *Effect of Variation in Rivet Diameter and Pitch on the Average Stress at Maximum Load for 24S-T3 and 75S-T6 Aluminum-Alloy, Flat, Z-Stiffened Panels That Fail by Local Instability*, NACA TN 2139, 1950.

[20] Hickman, W. A., and Dow, N. F., *Compressive Strength of 24S-T Aluminum-Alloy Flat Panels with Longitudinal Formed Hat-Section Stiffeners Having Four Ratios of Stiffener Thickness to Skin Thickness*, NACA TN 1553, 1948.

[21] Dow, N. F., and Hickman, W. A., *Design Charts for Flat Compression Panels Having Longitudinal Extruded Y-Section Stiffeners and Comparison with Panels Having Formed Z-Section Stiffeners*, NACA TN 1389, 1947.

[22] Heimerl, G. J., and Roberts, W. M., *Determination of Plate Compressive Strengths at Elevated Temperatures*, NACA TN 1806, February, 1949.

[23] Mathauser, E. E., and Deveikis, W. D., *Investigation of the Compressive Strength and Creep Lifetime of 2024-T3 Aluminum-Alloy Plates at Elevated Temperatures*, NACA TN 3552, January, 1956.

[24] Mathauser, E. E., and Deveikis, W. D., *Investigation of the Compressive Strength and Creep Lifetime of 2024-T Aluminum-Alloy Skin-Stringer Panels at Elevated Temperatures*, NACA TN 3647, May, 1956.

[25] Gerard, G., *Buckling Efficiencies of Plate Materials at Elevated Temperatures*, Journal of the Aeronautical Sciences, Vol. 22, No. 3, pp. 194–196, March, 1955.

[26] Gerard, G., *Thermostructural Efficiencies of Compression Elements and Materials*, *Trans. ASME*, Vol. 79, No. 5, pp. 967–973, July, 1957.

Notice to Contributors

Manuscripts submitted for publication *must* be double- or triple-spaced originals. There should be wide margins on all sides of the sheets and triple spacing around formulas to allow for the marking of directions to the printer.

Original drawings (jet black India ink on white paper or tracing cloth) should accompany the manuscript. *(Blueprints are not acceptable.)* Photographs *must* be on glossy white paper. The smallest lettering on 8- by 10-in. figures should be no less than 1/4 in. high.

Formulas should be typewritten or carefully written in pen and ink. The difference between capital and lower-case letters and Greek symbols should be clearly distinguished.

See Inside Back Cover of this issue for further details

The Characteristics of Two-Dimensional Sails in Hypersonic Flow

WALTER DASKIN* AND LEWIS FELDMAN**

Gruen Applied Science Laboratories, Inc.

Summary

The aerodynamic and geometric characteristics of two-dimensional sails in a hypersonic flow are investigated in this paper. These surfaces would have very large lift and drag per unit weight. Therefore, they appear attractive wherever large values of the parameters C_LA/W or C_DA/W are needed. Simple closed expressions are derived for the sail shape and the corresponding lift, drag, and moment coefficients. Charts of these quantities are presented for the entire useful design range. The results can also be applied to two-dimensional parachutes.

Symbols

A = sail, area, sq.ft.
B = total length of sail, ft.
C = chord of sail, ft.
C_D = drag coefficient
C_L = lift coefficient
C_M = moment coefficient
D = drag, lbs.
L = lift, lbs.
M = pitching moment, ft.lbs.
M_∞ = free-stream Mach Number
p = pressure, lbs. per sq.ft.
p_0 = stagnation pressure behind normal shock, lbs. per sq.ft.
q = dynamic pressure, $(1/2)\rho V^2$, lbs per sq.ft.
S = length along sail, ft.
T = tension per unit span, lbs. per ft.
V = velocity, ft. per sec.
W = weight, lbs.
x = longitudinal coordinate (Fig. 1), ft.
y = normal coordinate (Fig. 1), ft.
α = angle of attack, rad., degree
θ = local angle of sail, rad., degree
ν = arbitrary family designation (Eq. 13), degree
ρ = density, slugs per cu.ft.

Subscripts

T = trailing edge
L = leading edge
∞ = conditions far upstream of sail

Introduction

IT IS DESIRABLE, in a number of supersonic and hypersonic problems, to construct surfaces having large values of lift and/or drag per unit weight. The possibility of using a sail of woven wire cloth seems attractive since such a device would have extremely small weight per unit area and could presumably be made of a material that could withstand the high temperatures to which it would be exposed in hypersonic flight. The aerodynamic characteristics of such a two-dimensional sail in a hypersonic flow are investigated in this paper.

The problem originally arose as a simplification of the incompressible sail problem which will be reported elsewhere by Lewis Feldman.

Analysis

Consider the coordinate system of Fig. 1, with uniform flow in the direction of the x axis. If we have a high aspect ratio flexible sheet of uniform chord stretched with very high tension in the direction normal to the paper (or if this sheet is stiff in the direction normal to the paper but flexible in the plane of the paper), we reduce the problem to a two-dimensional one. If p is the local pressure difference across the flexible sheet, and θ the local angle of inclination, then

$$p \cos\theta \, ds = T \, d(\sin\theta) \quad \text{or} \quad p = T(d\theta/dS) \tag{1}$$

where T is the tension per unit span and dS is the differential arc length of the sail.

Taking the modified Newtonian approximation[1] for the pressure on the lower surfaces,

$$p_{\text{lower}} = p_0 \sin^2\theta + p_\infty \cos^2\theta \tag{2a}$$

In order to simplify the algebra and to make the resulting sail shapes independent of Mach Number, it is convenient to set $p_{\text{upper}} = p_\infty \cos^2\theta$.

This gives the required zero pressure difference at $\theta = 0$ and it is a good approximation when $\theta \neq 0$ because the upper surface pressure is much smaller than p_0, and $p_\infty \ll p_0$. Then the local pressure difference across the sail is

$$p = p_0 \sin^2\theta \tag{2b}*$$

Equating (1) and (2b) we have

$$p_0 \sin^2\theta = T(d\theta/dS) \tag{3}$$

the basic equation of equilibrium of sail elements under tension and hypersonic loading.

This is integrated to

Received April 29, 1957. Revised and received August 19, 1957.

* Senior Scientist.

** Project Scientist.

* Had the unmodified Newtonian pressure equation been used instead at Eq. (2) or (3), the normalization quantity for lengths in all subsequent equations would have been $2q/T$ instead of p_0/T, and the factor 2 would have appeared in the aerodynamic coefficients in place of p_0/q. Inclusion of an added term to correct for the finite-density ratio across the shock would have added no further difficulty. Use of the "Newtonian plus centrifugal" form would have resulted in an integro-differential equation.

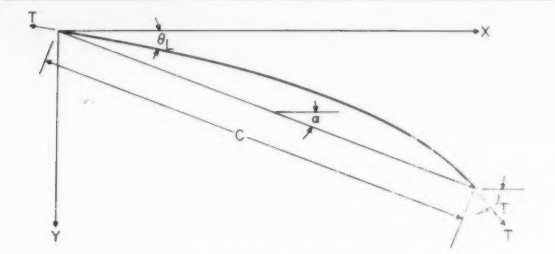

FIG. 1. Illustration of sail nomenclature.

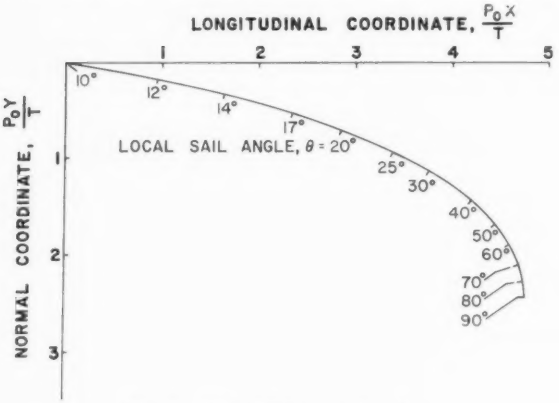

FIG. 2. Shape of hypersonic sails.

$$p_0 S/T = \int_L (d\theta/\sin^2\theta) = \cot\theta_L - \cot\theta \qquad (4)$$

where S is the arc length of sail measured from the leading edge and θ_L is the leading-edge angle.

The total length of the sail, B, is given by

$$(p_0 B/T) = \cot\theta_L - \cot\theta_T \qquad (5)$$

where θ_T is the trailing-edge angle.

The x and y coordinates are, respectively,

$$\left.\begin{aligned} p_0 x/T &= [(1/\sin\theta_L) - (1/\sin\theta)] \\ p_0 y/T &= \ln[\tan(\theta/2)/\tan(\theta_L/2)] \end{aligned}\right\} \qquad (6)$$

giving the coordinates of the trailing edge as

$$\left.\begin{aligned} p_0 x_T/T &= (1/\sin\theta_L) - (1/\sin\theta_T) \\ p_0 y_T/T &= \ln[\tan(\theta_T/2)/\tan(\theta_L/2)] \end{aligned}\right\} \qquad (7)$$

The chord, C, of the sail is then

$$p_0 C/T = \sqrt{(p_0 x_T/T)^2 + (p_0 y_T/T)^2} \qquad (8)$$

and the geometrical angle of attack, α, is given by

$$\alpha = \tan^{-1}[(p_0 y_T/T)/(p_0 x_T/T)] \qquad (9)$$

The shape of any such sail can be completely deduced from Eq. (6). This universal shape is plotted in Fig. 2. Superimposed on the actual sail shape are its local angles of inclination, θ. One can therefore determine the shape of any sail, given its leading- and trailing-edge angles, by simply using that portion of the universal curve between these two angles. The chord may be drawn between these two points, and the geometrical angle of attack measured directly. The complete shape for sails with trailing-edge angles greater than 90° may be determined by reflecting the curve of Fig. 2 about a line parallel to the x axis passing through the point $\theta = 90°$. Thus, one could conceivably find the shape of slack two-dimensional sails which are secured through a fairlead or even two-dimensional parachutes, although it is doubtful whether the approximation of Eq. (3) is valid for such a shape if it is not ventilated near the region of its vertical slope.

One can also use Fig. 2 to determine the leading- and tailing-edge angles of a sail with fixed geometrical angle of attack and various values of tension by moving a line representing the chord at the given angle of attack closer to the curve as the tension increases, until the curve and chord are tangent at the condition of infinite tension.

Although the origin of the figure is at the leading edge of a 10° sail, it should be noted that this is quite arbitrary, and the origin could be shifted to any other point on the curve. Since, with the aerodynamic force normal to the surface the tension is uniform, we can find the total lift, drag, and leading-edge moment by simply considering the attaching forces and their angles at the leading and trailing edges. The results, identical with those found by integration of the pressure, are

$$\left.\begin{aligned} L &= T(\sin\theta_T - \sin\theta_L) \\ D &= T(\cos\theta_L - \cos\theta_T) \\ M &= T(y_T\cos\theta_T - x_T\sin\theta_T) \end{aligned}\right\} \qquad (10)$$

and the corresponding coefficients are

$$\left.\begin{aligned} C_L &= L/(1/2)\rho V^2 C = (p_0/q)[(\sin\theta_T - \sin\theta_L)/(p_0 C/T)] \\ C_D &= D/(1/2)\rho V^2 C = (p_0/q) \times [(\cos\theta_L - \cos\theta_T)/(p_0 C/T)] \\ C_M &= M/(1/2)\rho V^2 C^2 = (p_0/q)\{[(p_0 y_T/T) \times \cos\theta_T - (p_0 x_T/T)\sin\theta_T]/(p_0 C/T)^2\} \\ C_L/C_D &= L/D = [(\sin\theta_T - \sin\theta_L) \div (\cos\theta_L - \cos\theta_T)] \end{aligned}\right\} \qquad (11)$$

It should be noted that for the infinite tension (flat plate) case, these expressions reduce to

$$\left.\begin{aligned} C_L &= (p_0/q)\sin^2\theta\cos\theta, \qquad C_D = (p_0/q)\sin^3\theta \\ C_M &= -(p_0/q)(\sin^2\theta/2), \qquad L/D = \cot\theta \end{aligned}\right\} \qquad (12)$$

The value of p_0/q is virtually independent of Mach Number for hypersonic flow, and therefore, as expected, the coefficients are independent of Mach Number. The value $p_0/q = 1.839$ corresponding to infinite Mach Number, and a specific heat ratio of 1.4 was used in all of the calculations. It can be shown that the results do not vary significantly for $5/3 \geq \gamma \geq 1.2$.

Table 1 lists the value of p_0/q as a function of the free-stream Mach Number, M_∞, for a perfect gas with specific heat ratio 1.4. It is seen that the asymptotic value is essentially reached for Mach Numbers in excess of 4.*

*The values in Table 1 may be used as Mach Number corrections for the coefficients plotted in Figs. 3 and 4.

TABLE 1
Effect of Mach Number on p_0/q for $\gamma = 1.4$

M_∞	2	3	4	5	6	8	10	15	20	∞
p_0/q	2.014	1.914	1.882	1.866	1.858	1.850	1.847	1.842	1.841	1.839
$(p_0/q)/(p_0/q)_{M_\infty=\infty}$	1.095	1.041	1.023	1.014	1.010	1.006	1.004	1.001	1.001	1.000

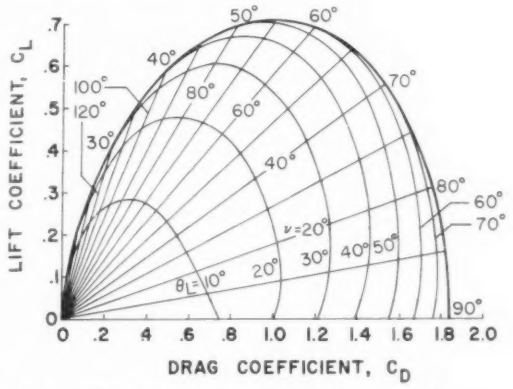

FIG. 3. Lift and drag characteristics of hypersonic sails.

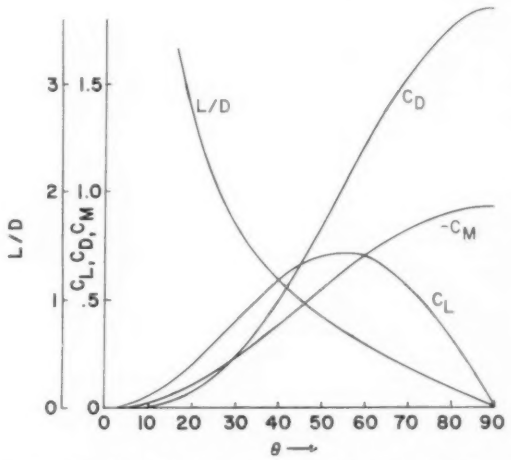

FIG. 4. Aerodynamic characteristics of hypersonic sails with infinite tension.

One may choose, as independent variables, either θ_L and θ_T or any other pair of independent variables, such as chord p_0C/T and angle of attack α. For convenience, the leading- and trailing-edge angles were chosen as the independent variables in the calculations.

RESULTS OF CALCULATIONS

The dimensionless lengths p_0x/T, p_0y/C, and p_0C/T, the lift, drag, and moment coefficients and the lift-drag ratio were computed for the entire range of values of θ_L and θ_T which might be encountered. θ_L was taken from 10° to 90° in 10° increments, and θ_T was taken in 10° increments from θ_L to its complement.

The results for C_L and C_D are best represented by the lift-drag polar, Fig. 3. The envelope of the curve represents the flat plate (infinite tension sail). Two families of curves appear in the figure, those of constant leading-edge angle and those of constant angle ν, where ν is defined by $\theta_T = 180° - \theta_L - \nu$.

The figure is considerably less confusing when plotted in terms of ν rather than θ_T, since the families plotted in this manner tend to intersect each other at relatively large angles, while the θ_T method of plotting results in curves which are tangent, or nearly so, all along the envelope.

Fig. 3 shows the value of ν which maximizes the lift for each leading-edge angle. The angles on the envelope of the curve represent the slope of the infinite tension sail at each point on the envelope. As can be seen from the figure, values of L/D in excess of unity can be achieved for relatively tight sails with small leading-edge angles, even when moderate friction drag coefficients are added to the drag coefficients here computed.

Fig. 4 shows the aerodynamic characteristics of flat plates (infinite tension sails) as computed by Eqs. (12). These values do not, of course, include the usual corrections due to the hypersonic boundary layer. Such corrections would be most important at low angles of attack and would result in an appreciable decrease of the computed values of L/D. Nevertheless, Fig. 4 is included as representing the characteristics of the elemental portions of the sails used in the calculations.

Values of W/A have been computed for several sail configurations using woven-wire cloth or uniform sheet material under tension. The configurations investigated included swept-back delta as well as two-dimensional high and low aspect ratio sails. The weight estimates included the weight of spars necessary to properly support the sail. These sail weights were compared with the estimated weights of conventional wing structures, using accepted wing-weight estimating techniques. For identical materials, stress levels, and plan forms, the sail weights were 1/5 to 1/10 of the weights of the conventional wing structures. This significant decrease in weight is primarily due to the fact that the sail structure carries its load primarily in tension, while the conventional wing must be designed for bending loads. It should be noted that the weight of the sail itself was negligible in most of the cases investigated, the bulk of the weight of the sail structure being in the spars.

Since the lift and drag coefficients of sails are roughly equal to those which can be expected from conventional surfaces at hypersonic speeds, (see Fig. 3) and the sail weights per unit area are significantly less than conventional W/A values, the use of sails will result in large values of the parameters C_LA/W and C_DA/W. Large values of these parameters are often required in hypersonic flight.

REFERENCE

[1] Lees, L., *Laminar Heat Transfer Over Blunt Nosed Bodies at Hypersonic Flight Speeds*, Jet Prop., Vol. 26, No. 4, April, 1956.

Readers' Forum

BRIEF REPORTS of investigations in the aeronautical sciences and discussions of papers published in the JOURNAL are presented in this special department. Entries must be restricted to a maximum of 1,300 words or the equivalent of one JOURNAL page including formulas and illustrations. Publication is completed as soon as possible after receipt of the material. The Editorial Committee does not hold itself responsible for the opinions expressed by the correspondents.

Contents

On Optimum Nose Curves for Missiles in the Superaerodynamic Regime ..... H. S. TAN 56

On Optimum Nose Shapes for Missiles in the Superaerodynamic Region ..... I. D. CHANG 57

Supersonic Flow Around Blunt Bodies ..... HYMAN SERBIN 58

Marin's Strength Hypothesis ..... A. D. TOPPING 59
Author's Reply ..... JOSEPH MARIN 60

A Finite Vortex Method for Slender Wing-Body Combinations ..... GEORGE S. CAMPBELL 60

Calculation of Local Heat-Transfer Coefficients on Slender Surfaces of Revolution by the Mangler Transformation ..... SHAO-YEN KO 62

Thermal Stresses in a Circular Bulkhead Subjected to a Radial Temperature Distribution ..... MARVIN FORRAY AND MELVIN ZAID 63

Boundary-Layer Correction in Supersonic Nozzle Scaling ..... ABRAHAM KOGAN 64

Hypersonic Flow Around a Sphere ..... R. D. LINNELL 65

Creep Buckling of Tubes in Torsion ..... IAIN FINNIE 66

On the Stream Functions in Nonsteady Three-Dimensional Flow ..... M. Z. v. KRZYWOBLOCKI 67

Mass Transfer Cooling at Mach Number 4.8 ..... B. M. LEADON, C. J. SCOTT, AND G. E. ANDERSON 67

Boundary-Layer Slip Solutions for a Flat Plate ..... HIDENORI HASIMOTO 68

A Simple Graphical Method for Constructing Two-Dimensional Supersonic Flows by Means of a Drafting Machine ..... F. EDWARD EHLERS 69

Note on the Reflection of Sound Waves at an Oblique Shock ..... C. T. CHANG 70

Application of Görtler's Series Method to the Boundary-Layer Energy Equation ..... E. M. SPARROW 71

On Optimum Nose Curves for Missiles in the Superaerodynamic Regime

H. S. Tan

Professor of Aeronautical Engineering, University of Detroit, Detroit, Mich.

July 15, 1957

IN REFERENCE 1, it was shown that for a missile with a smooth surface in the superaerodynamic regime, the consideration of specular molecular reflection results in the following differential equation for the determination of optimum (minimum drag) shape of the meridian nose curve

$$y'' = -(y'^2/y)\,[(1 + y'^2)/(k - y'^2)] \tag{1}$$

where $k = 3$ for regular reflection and $k = 2$ for random reflection.

It was pointed out that there is little hope of finding an analytic solution to Eq. (1), and so, numerical integration was resorted to.

It is interesting to note, however, that a first integral of Eq. (1) can readily be obtained as follows: Noting $y'' = y'dy'/dy$, Eq. (1) can be written

$$ydy'/dy = -y'(1 + y'^2)/(k - y'^2)$$

for example,

$$-dy/y = [k/y' - (k + 1)y'/(1 + y'^2)]dy' \tag{2}$$

Now Eq. (2) can be integrated once to give

$$yy'^k/(1 + y'^2)^{(k+1)/2} = C \tag{3}$$

where C is the integration constant.

The analytic behavior of the optimum nose curve can then be qualitatively discussed, based on Eq. (3), as follows.

If the curve ever crosses the axis $y = 0$, or if its slope vanishes anywhere, then C must be identically zero. This results in the trivial case of

$$y = 0, \text{ or constant} \tag{4}$$

which is physically evident, but has no practical interest.

Contributors Please Note

Readers' Forum items must be confined to the equivalent of one page in the *Journal*. Contributions that exceed this limit will be returned to the authors for condensation and rewrite. To avoid inconvenience and delay, please adhere to the following specifications:

(1) Five, double-spaced, typewritten, manuscript pages ($8^1/_2$ by 11 in.), including wide margins, formulas, and headings equal one printed page.

(2) For every illustration, deduct at least one-half or as much as one manuscript page, depending on the size of the illustration.

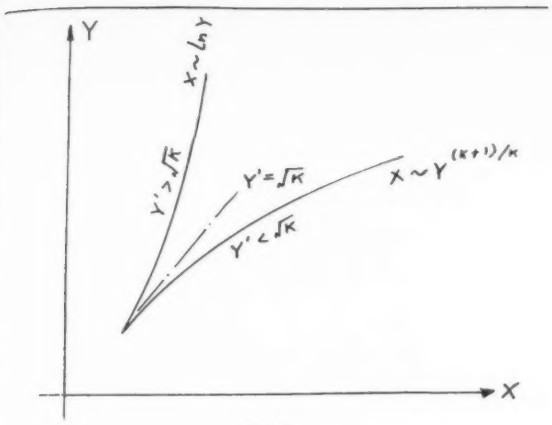

FIG. 1.

If C does not vanish, then the curve cannot reach the axis $y = 0$ but can be made to approach the axis as closely as we like.

From Eq. (1), it is evident that the curve has a cusp at $y' = \sqrt{k}$. Now writing Eq. (3) in the form

$$y = C(1 + y'^2)^{(k+1)/2}/y'^k \tag{5}$$

and considering y' as a parameter, we can differentiate Eq. (5) with respect to y'. To obtain an extremum value of y, we must solve the equation

$$dy/dy' = 0 \tag{6}$$

Substitution of Eq. (5) into Eq. (6) yields the solution

$$y' = \pm\sqrt{k} \tag{7}$$

Thus it is seen that at $y' = \sqrt{k}$, y has, indeed, an extremum. Moreover, at $y' = \sqrt{k}$, the curve branches into two separate portions—one for which $y' < \sqrt{k}$, and the other for which $y' > \sqrt{k}$.

The asymptotic shapes of these two branches of the curve can further be obtained. For the branch with $y' < \sqrt{k}$, when $y' \ll 1$, we have

$$dy/dx = y' \doteq (C/y)^{1/k} \tag{8}$$

Upon integration, this gives

$$x \doteq C_1 y^{(k+1)/k} + C_2, \quad C_1 = k/(k+1)C^{1/k} \tag{9}$$

For the branch with $y' > \sqrt{k}$, when $y' \gg 1$, we have

$$dy/dx = y' \doteq y/C \tag{10}$$

Upon integration, this gives

$$x \doteq C \ln y + C_3 \tag{11}$$

C_2, C_3 are both integration constants.

Since the differential Eq. (1) is of second order, two conditions can be imposed on an initial point of the curve. By choosing for $x = x_0$,

$$y = y_0, \quad y' = 1 \tag{12}$$

C is uniquely specified, and a numerical integration can be readily carried out using Eq. (3).

The two branches of curve have been qualitatively indicated in Fig. 1. It is interesting to note that the branch of the curve shown in reference 1 for which $y' > \sqrt{k}$ is incorrect. But since this branch has no physical significance itself, validity of the result is not affected. On the other hand, the resulting curve for $y' < \sqrt{k}$ obtained by numerical integration should be checked for its asymptotic behavior—i.e., Eq. (9).

REFERENCE

[1] Carter, W. J., *Optimum Nose Shapes for Missiles in the Superaerodynamic Region*, Journal of the Aeronautical Sciences, Vol. 24, No. 7, pp. 527–532, July, 1957.

On Optimum Nose Shapes for Missiles in the Superaerodynamic Region

I. D. Chang
Graduate Student, Department of Aeronautics, California Institute of Technology, Pasadena, Calif.
July 15, 1957

IN A RECENT PAPER in this JOURNAL,[1] W. J. Carter made a study of the optimum nose shapes for missiles in the superaerodynamic region. He found that for the case of specular molecular reflection from a smooth surface, the optimum nose shape is given by the equation

$$y'' = -(y'^2/y)\,[(y'^2 + 1)(3 - y'^2)] \tag{1}$$

where y is the radius of the nose about the longitudinal axis. We want to point out that Eq. (1) can be readily integrated in term of simple functions.

Multiplying both sides of Eq. (1) by $p = dy/dx$, we get

$$p(dp/dx) = -(p^2/y)\,[(p^2 + 1)/(3 - p^2)]\,(dy/dx)$$

which may be written as

$$dy/y = (p^2 - 3)dp/p(p^2 + 1) = \{[4p/(p^2 + 1)] - (3/p)\}dp$$

integrating,

$$y = c_1(p^2 + 1)^2/p^3 \quad (c_1 = \text{const.}) \tag{2}$$

Also, from $dx = dy/p$, using the result of Eq. (2),

$$dx = c_1(p^4 - 2p^2 - 3)dp/p^5$$

Hence

$$x = c_1[\log p + p^{-2} + (3/4)p^{-4}] + c_2 \tag{3}$$

Eqs. (2) and (3) give the solution for Eq. (1) in parametric form. For the case calculated by Carter, $c_1 = 2.50$ and $c_2 = -0.235$. Eqs. (2) and (3) then give the values for x and y shown in Table 1.

As shown in Fig. 1, the curve $y(x)$ has two branches, separated by a cusp at which $y' = \sqrt{3}$. For the case calculated here, this point corresponds to $x = 2.18$ and $y = 7.70$.

TABLE 1

x	y	y'	x	y	y'
168.184	82.251	0.335	2.203	7.735	1.600
75.296	48.064	0.415	2.181	7.700	1.700
15.511	18.681	0.645	2.180	7.698	1.732
7.691	13.133	0.800	2.180	7.699	1.750
4.722	10.566	0.949	2.185	7.706	1.800
4.140	10.000	1.000	2.206	7.746	1.900
3.697	9.546	1.050	2.240	7.813	2.000
3.077	8.867	1.150	2.504	8.410	2.500
2.557	8.234	1.300	2.812	9.259	3.000
2.260	7.824	1.500	3.892	13.520	5.000

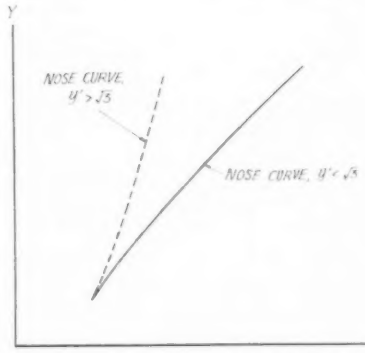

FIG. 1. Nose curve for minimum drag with specular reflection.

The numerical results shown here differ considerably from that given by Carter. Also, in Fig. 3 in his paper, the nose curve corresponding to $y' > \sqrt{3}$ is erroneous.

REFERENCE

[1] Carter, W. J., *Optimum Nose Shapes for Missiles in the Superaerodynamic Region*, Journal of the Aeronautical Sciences, Vol. 24, No. 7, pp. 527–532, July, 1957.

Supersonic Flow Around Blunt Bodies

Hyman Serbin

Physical Scientist, Aeronautics Department, The RAND Corporation, Santa Monica, Calif.

June 7, 1957

THE NEWTONIAN THEORY of impact has been shown to be useful for pressure calculations on the forward facing part of bodies moving at high speed. It is now a familiar practice to use this information to calculate nonviscous velocities at the wall and then to estimate rates of heat transfer. This procedure is perhaps open to question; heat-transfer rates depend on velocity gradients which are not given by the Newtonian analysis. Nor can one obtain information on boundary-layer stability or all the body stability derivatives. It seems, therefore, inevitable that, as design proceeds with these hypersonic missiles, there will be a greater need for more accurate aerodynamic theories either to predict what will happen in unfamiliar flight conditions or to effect an extrapolation from a known test result to the design condition.

A start in this direction has been made by the writer[1, 2] for two kinds of blunt bodies, one with a flat-disc face and the other with a hemispherical face. Our theory depends on the limiting

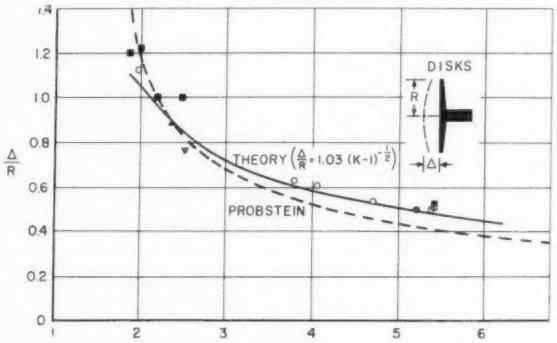

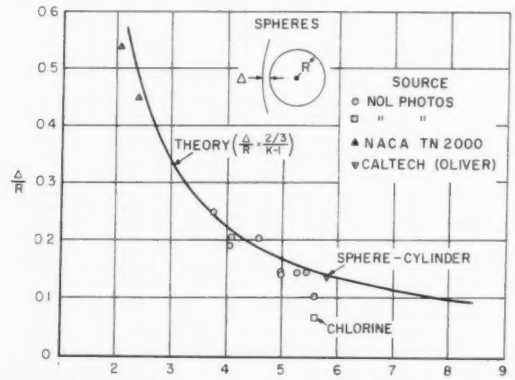

FIG. 1 (*Top*). Detachment distance versus density ratio K for discs. FIG. 2 (*Bottom*). Detachment distance versus density ratio K for spheres.

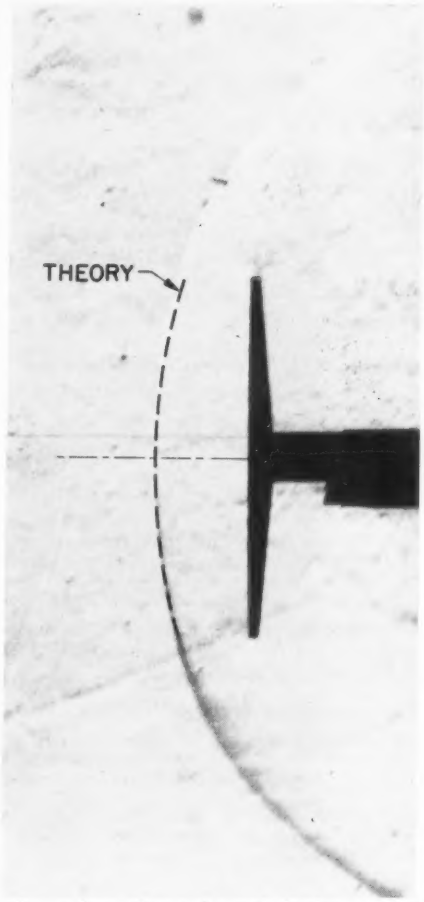

FIG. 3. Comparison of experimental shock wave pattern at $M = 6.7$ with theory.

case where γ, the ratio of specific heats, approaches unity without being equal to 1. The limit $\gamma = 1$ characterizes the Newtonian theory; hence our theory may be characterized as a reformulation of the Newtonian theory on the basis of gas dynamics.

Following the scheme used by Prandtl for the simplification of the hydrodynamic equations when the Reynolds Number is large, we have simplified the gas-dynamic equations in the limit where M, the free-stream Mach Number, is large, and $\gamma \to 1$. The results obtained include the shock detachment distance, shock shape, streamlines, and velocities. These are to be regarded as asymptotic values appropriate to the limits described above.

For the purposes of designing at high speed, the results seem to be very satisfactory. However, since there is a substantial amount of data for blunt bodies at low supersonic speeds, it is of interest to see how our results can be extended into this speed range.

There seems to be an impression among some aerodynamicists that the case $\gamma \neq 1$, $M < \infty$ can be correlated by replacing both parameters by the single parameter.

K = density ratio across normal shocks at free-stream M.

We do not know the origin of this remark; however, it may be easily derived from our equations[1] for large K, at least for the subsonic part of the flow field.

To translate our results to finite Mach Number, one need only make the formal substitution

$$(\gamma - 1)/2 \to 1/K \qquad (1)$$

In particular, the shock detachment distance Δ takes the form

$$\Delta/R = 1.03\,K^{-1/2} \quad \text{disc} \tag{2}$$

$$\Delta/R = (2/3)K^{-1} \quad \text{sphere} \tag{3}$$

where R represents the radius of the disc and sphere respectively.

Another analysis of the flow around blunt bodies has been presented recently by Probstein.[3] At the end of his paper, Probstein takes occasion to rewrite our asymptotic formula for discs in a similar fashion to that shown above but with K replaced by $K - 1$.

Within the framework of our theory (K large), there is no way to distinguish K from $K - 1$. The use of either one in Eqs. (2) and (3) is equally satisfactory when one examines test data at large K. However, the use of $K - 1$ is attractive from a *formal* standpoint because when the free-stream Mach Number approaches unity, the distance Δ so expressed approaches infinity. This is consistent with our knowledge of transonic flow.

Thus, our formal rule is to make the substitution everywhere in references 1 and 2

$$(\gamma - 1)/2 \rightarrow 1/(K - 1) \tag{4}$$

from which the stand-off formulas become

$$\Delta/R = 1.03\,(K - 1)^{-1/2} \quad \text{disc} \tag{5}$$

$$= 2/3\,(K - 1)^{-1} \quad \text{sphere} \tag{6}$$

Plots of these relations are shown in Figs. 1 and 2, respectively, and compared with test data. Fig. 1 also shows theoretical results drawn from Probstein. The agreement between test and our theory is very satisfactory at high K (= high M). What is surprising, and hardly to be anticipated, is the good agreement in the low supersonic range.

A similar comparison could be made between the theoretically-derived and experimentally-observed shock. They appear to be almost identical at the higher Mach Numbers (Figs. 3 and 4). The lower Mach numbers have not been checked.

Quite apart from the evidence presented, it appears that our theory is accurate (to principal order in K^{-1}) because all the equations defining the flow field are utilized. The shock shape is a "consequence" of the analysis, not part of an assumption. To mention one item of interest, the velocity is constant in magnitude along each streamline almost up to the sonic line. The direction of flow, however, changes continuously so that the flow is not the shear flow assumed by some writers.

We have dwelt on the validity of the theory principally because of one theoretical consequence which is somewhat unexpected. According to our theory, the velocity along the streamline at the wall would be zero almost up to the shoulder of the body. This means that the inviscid flow near the wall resembles a Couette flow. This is quite different from what one would expect on the basis of slender-body aerodynamics. There the inviscid theory shows a finite velocity at the wall which must be reduced to zero by interposing a viscous boundary layer. On the other hand, our theoretical flow would exhibit a temperature discontinuity which can conceivably be bridged by a kind of boundary layer.

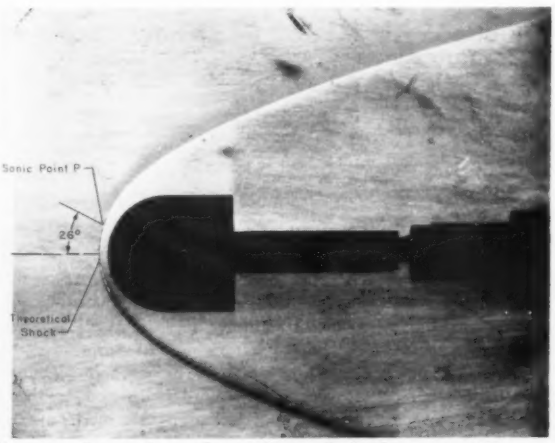

FIG. 4. Comparison of experimental shock wave pattern at $M = 5.8$ with theory.

It might be argued that a velocity discontinuity would appear in a second-order analysis, and this is indeed the case. Yet it would be worth while to see if the available heat-transfer data could not be satisfactorily predicted on the basis of the first-order inviscid shear flow already derived.

REFERENCES

[1] Serbin, H., *Hypersonic, Non-Viscous Flow around a Circular Disk Normal to the Stream*, The Rand Corporation, Research Memorandum RM-1713, May 3, 1956.

[2] Serbin, H., *Hypersonic, Non-Viscous Flow around a Sphere*, The RAND Corporation, Research Memorandum RM-1772, August 13, 1956.

[3] Probstein, R. F., *Inviscid Flow in the Stagnation Point Region of Very Blunt-Nosed Bodies at Hypersonic Flight Speeds*, WADC TN 56-395, September, 1956.

Marin's Strength Hypothesis*

A. D. Topping
Engineer Specialist (Stress), Goodyear Aircraft Corporation, Akron, Ohio
June 17, 1957

A HYPOTHESIS for describing the limiting conditions of stress in materials having different properties in different directions and different strengths in tension and compression was recently proposed by Marin.[1] It is the purpose of this note to show that the hypothesis is not only questionable, but untenable.

Marin begins with the distortion energy or octahedral shear theory of strength, according to either of which the stress-space surface describing failure is a circular cylinder whose axis makes equal angles with each of the principal stress axes and is the axis of hydrostatic stress. Its equation may be written either as Marin's Eq. (2) or his Eq. (7). This theory has been successful in predicting over a fairly wide range yield strengths of isotropic ductile metals having equal tensile and compressive strengths. Marin speculates that it can be made to apply to all materials by generalizing Eq. (2) to the form of his Eq. (12)—i.e.,

$$(\sigma_1 - a)^2 + (\sigma_2 - b)^2 + (\sigma_3 - c)^2 + q[(\sigma_1 - a)(\sigma_2 - b) + (\sigma_2 - b)(\sigma_3 - c) + (\sigma_3 - c) \times (\sigma_1 - a)] = \sigma^2$$

where σ_1, σ_2, and σ_3 are principal stresses.

Eq. (12) contains five constants, a, b, c, q, and σ, to be determined experimentally. If one considers now an orthotropic material having different tensile and compressive strengths along each of its three natural axes, it is apparent that any equation purporting to describe the limiting stress conditions for such a material must have at least six independent constants.

The possibility remains that Eq. (12) may prove useful for some less general case. Upon further examination, it can be seen that in a rectangular coordinate system with the coordinates σ_1, σ_2, σ_3, Eq. (12) describes one of the following surfaces of revolution depending on the value of q:

$q < -1$, hyperboloid of one sheet
$q = -1$, circular cylinder
$-1 < q < 2$, ellipsoid of revolution
$q = 2$, two planes perpendicular to hydrostatic axis
$q > 2$, hyperboloid of two sheets

Consider now the triaxial strength of an isotropic material having unequal tensile and compressive strengths, a problem to

* The writer is indebted to his colleague, Mr. J. D. Marketos, for identification of the geometric surfaces described by Marin's equation.

which Marin's "generalized strength theory" should apply as to a mere specific case.

Marin implies that his hypothesis is applicable to both yield and ultimate strengths. This is impossible because we know from experience that yielding is simply not the same phenomenon as rupture; rupture cannot always be described as a function of stress alone. Yielding is a shearing or sliding phenomenon while rupture may be either a sliding failure or a cleavage or separation failure. The application of a hydrostatic tension may produce rupture, but not yielding. Thus it is conceivable that rupture occurs before yielding. The nature of the yield surface for states of stress in this region is only of academic interest, of course, and is quite incapable of being determined experimentally. The limiting stress surface for rupture is closed at that end of the hydrostatic stress axis. At the compression end of this axis, however, we find experimentally neither yielding nor rupture of nonporous materials. Thus the limiting surface for either must be open at that end.

For an isotropic material having unequal tensile and compressive strengths, $a = b = c$ in Eq. (12), and the axis of symmetry of the surfaces which it describes becomes the hydrostatic axis. Considering the possible shapes of the surface, one may eliminate at once the values $q = -1$ (since then the simple tensile and compressive strengths would be equal); $q = 2$ and $-1 < q < 2$, since an ellipsoid is closed at both ends of the hydrostatic axis. The hyperboloid of one sheet is obviously not applicable to rupture, but might possibly describe yielding. As for the hyperboloid of two sheets, clearly both sheets could not have physical significance. That sheet which is open toward the compression end of the hydrostatic axis, however, does have a plausible shape, provided $a > \sigma/3(1 + q)$ so that a pure hydrostatic stress must be tensile to cause failure. Both $q > 2$ and $q < -1$ are particular cases of the theory of strength first proposed by Schleicher[2] and which Nadai[3, 4] has shown can be stated as $\tau_y = f(p)$, where τ_y is the octahedral shear and p is the hydrostatic or octahedral normal stress. It differs from the Mohr theory in stress space only in that it is a surface of revolution, while Mohr limiting surface has a hexagonal cross section which can be inscribed inside the circular cross section of the Schleicher-Nadai surface at the same octahedral normal stress[5, 6, 7]. Both theories impose a higher degree of symmetry on the limiting surface than does the requirement of isotropy, and furthermore, careful triaxial tests of marble and other rocks by various investigators, notably von Kármán, Böker, and Ros and Eichinger, yield results which cannot be described by a surface of revolution.[6, 8] Expressions which do describe the results have been suggested.[6, 7, 8] Further, the yield surface approaches asymptotically a circular cylinder at sufficiently high hydrostatic pressures.[6, 9] Such a surface could not be a hyperboloid. On the other hand, the rupture of a material should be described by a strain criterion rather than a stress criterion.[7, 8]

Owing perhaps to a lack of data due to the difficulty of triaxial testing of strong materials, metals having unequal tensile and compressive strengths do not appear to have been similarly investigated. Because brittleness is not so much a property of a material as a function of hydrostatic stress (among other things),[7] and also because such metals—e.g., cast metals—tend to be brittle, it is reasonable to suppose in the absence of evidence to the contrary, that they behave much as the rocks do.

Having thus disposed of Marin's hypothesis, a theory of strength for orthotropic materials proposed by Norris[10] may be noted. It also was generalized from the distortion energy theory but with the aid of a physical model. The resulting equations unlike Marin's, could only be plotted with six-dimensional coordinates. Norris found his theory to be in fair agreement with the results of some biaxial tests; nevertheless, some similar objections may be raised to it.

References

[1] Marin, J., *Theories of Strength for Combined Stresses and Nonisotropic Materials*, Journal of the Aeronautical Sciences, Vol. 24, No. 4, pp. 265–268, 274, April 1957.

[2] Schleicher, F., *Der Spannungszustand und die Fliessgrenze (Plastizitätsbedingung)*, ZAMM, Vol. 6, p. 199, 1926. See also Vol. 5, p. 478, 1925.

[3] Nadai, A., *Theories of Strength*, J. Appl. Mech., Vol. 1, No. 3, pp. 111–129, 1933.

[4] Nadai, A., *Theory of Flow and Fracture of Solids*, Vol. 1, pp. 207–228, McGraw-Hill Book Company, Inc., New York, 1950.

[5] Meldahl, A., *A New Graphical Method of Representing Strength Characteristics*, Brown Boveri Review, Vol. 31, No. 8, pp. 260–267, 1944. See also the Engineer's Digest, Vol. 2, No. 12, pp. 609–612, 1945.

[6] Topping, A. D., *The Use of Experimental Constants in the Application of Theories of Strength to Rock*, Proc. of the Second Midwestern Conference on Solid Mechanics, September 8, 9, 1955; Research Series No. 129, Purdue Univ. Engrg. Experiment Station, Lafayette, Ind., pp. 178–192.

[7] Topping, A. D., *Behavior of Materials Under Combined Stresses in Pressurized Structures*, Aeronautical Engineering Review, Vol. 16, No. 2, pp. 56–59, February, 1957.

[8] Topping, A. D., *Rock Strength: The Conditions of Failure*, World Oil, Vol. 141, No. 4, pp. 109–117, September, 1955.

[9] Torre, C., *Die Mechanik der Grenzbeanspruchungen*, Österreichisches Ingenieur-Archiv, Vol. 4, No. 1, pp. 93–108, 1950.

[10] Norris, C. B., *Strength of Orthotropic Materials Subjected to Combined Stresses*, Report No. 1816, Forest Products Laboratory, Madison, Wis., July, 1950.

Author's Reply

Joseph Marin

Head, Department of Engineering Mechanics, College of Engineering, The Pennsylvania State University

August 16, 1957

MR. TOPPING considers that the theory proposed by the writer is not valid. In order to prove his conclusion, it would be necessary to make a comparison between test results and the proposed theory. This has not been done since there is little available data on strength of nonisotropic materials subjected to combined stresses. The theory proposed may only be satisfactory for biaxial states of stress. The fact that the proposed nonisotropic theory reduces to a strength relation which has been found satisfactory for isotropic materials under biaxial stresses indicates that the proposed relation may provide an adequate representation for the biaxial strengths of nonisotropic materials.

It is recognized that yield and ultimate strengths correspond to different phenomena. It does not follow, however, that similar mathematical expressions (relating the principal stresses and uniaxial strength values) cannot be used to define both yield and ultimate strengths under combined stresses.

A Finite Vortex Method for Slender Wing-Body Combinations

George S. Campbell

Research Engineer, Hughes Aircraft Company, Culver City, Calif.

July 12, 1957

Introduction

IN THE APPLICATION of the slender-body theory to aerodynamic problems, the base-plane geometry is frequently too complicated to permit the usual transformation of the body to a circle. However, it has been found that such problems may be solved by using a reasonable number of two-dimensional vortices and satisfying boundary conditions at appropriate "control points" in the cross-flow plane. The method is demonstrated for a slender wing plus infinite body and compared with the more exact theory.[1] Although this procedure has been used to predict loads on a missile with folding wing panels, details of this application are deferred to a later date.

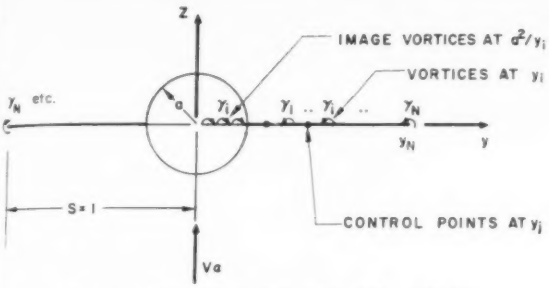

FIG. 1. Geometry of the wing-body problem.

ANALYSIS

The method for calculating the lift distribution of an arbitrary wing body is illustrated for the specific configuration shown in Fig. 1. A slender wing is mounted on an infinitely long circular cylinder, the combination being at angle of attack α. The wing is represented by N vortices across each panel, and the body is represented by a doublet at the origin. For each wing vortex there must be a corresponding image vortex within the body in order to cancel induced velocities at the body surface. The boundary condition of no flow through the wing is satisfied at N control points located midway between the vortices.

This procedure leads to a set of simultaneous equations that must be solved for the unknown vortex strengths γ_i.

$$\sum_{i=1}^{N} C_{ij}\gamma_i = 1 + (a/y_j)^2, \quad j = 1, \ldots N \tag{1}$$

The coefficients C_{ij} represent the downwash induced at the control points y_j by the vortices at $\pm y_i$ and at the image points $\pm a^2/y_i$.

$$C_{ij} = \frac{1}{2}\left[-\frac{1}{y_j - y_i} + \frac{1}{y_j + y_i} + \frac{1}{y_j - (a^2/y_i)} - \frac{1}{y_j + (a^2/y_i)} \right] \tag{2}$$

The terms on the right side of Eq. (1) represent the potential of the flow at infinity and the doublet at the origin. All lengths in these equations are expressed in semispans, and the vortex strength γ_i is made nondimensional by $\pi V \alpha s$. The positions of vortices and control points are, respectively,

$$\left.\begin{aligned} y_i &= a + [i(1-a)/N] \\ y_j &= a + [j - (1/2)]\,[(1-a)/N] \end{aligned}\right\} \tag{3}$$

For a given choice of N, the unknown vortex strengths γ_i are obtained by solving Eqs. (1) to (3). The wing loading is proportional to the bound vorticity Γ_i.

$$\Gamma_i = \sum_{n=i}^{N} \gamma_n \tag{4}$$

The load distribution over the body may be obtained by evaluating the velocity potential at the surface of the body due to all the vortices.

$$(1/q\alpha s)\,(dL/dy)_B = 2\sum_{i=1}^{N} \gamma_i \left\{ \pi - 2\tan^{-1}\left[(2y_i\sqrt{a^2 - y^2})/(y_i^2 - a^2) \right] \right\} \tag{5}$$

RESULTS

In order to evaluate the accuracy obtainable with the approximate method, results calculated from the preceding equations are compared with the "exact" slender-body results of reference 1. It is of course realized that the approximate method is necessary only for more complicated cross sections.

The variation of wing and body lift with diameter to span ratio is shown in Fig. 2 for several values of N, the number of vortices. Lift has been divided by lift of the exposed wing alone to give the usual interference factors of Morikawa.[2] The calculations show the expected improvement in accuracy with an increased number of vortices. ($N = \infty$ corresponds to the exact theory.[2]) Calculations for a wing alone show that the error in lift prediction is inversely proportional to N.

The load distribution for a wing-body combination of 0.3 diameter to span ratio is shown in Fig. 3. The exact result was obtained from the potential function given in reference 1 so that for unit semispan

$$\left.\begin{aligned} (1/q\alpha s)\,(dL/dy)_W &= 4\sqrt{(1 - y^2)\,[1 - (a^4/y^2)]} \\ (1/q\alpha s)\,(dL/dy)_B &= 4\sqrt{(1 + a^2)^2 - 4y^2} - 8\sqrt{a^2 - y^2} \end{aligned}\right\} \tag{6}$$

The use of a finite number of vortices overpredicts the tip loading of the wing but has relatively little effect on the body load distribution.

By way of summary, it has been found that a reasonably small number of two-dimensional vortices can be used to calculate the aerodynamic loads on slender wing-body combinations. The method is sufficiently general to permit arbitrary missile cross

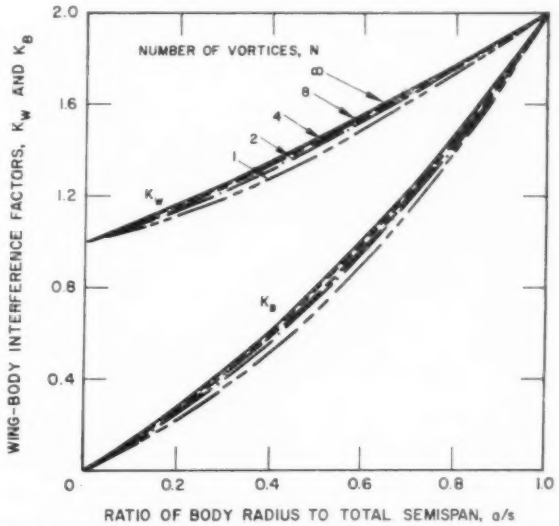

FIG. 2. Effect of the number of wing vortices on the lift-interference factors calculated for slender wing-body combinations.

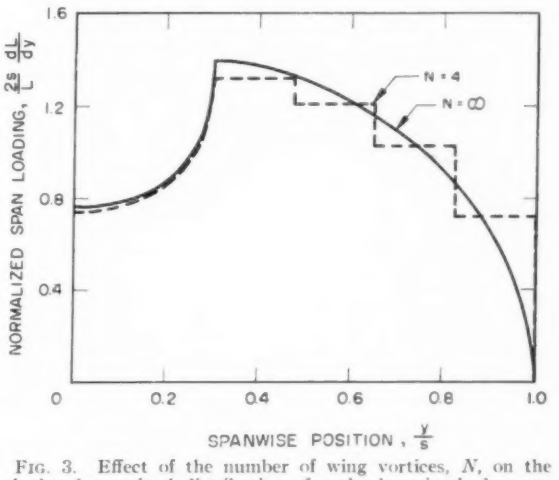

FIG. 3. Effect of the number of wing vortices, N, on the calculated span-load distribution of a slender wing-body combination, $a = 0.3s$.

sections provided computing machinery is available for the numerical calculation.

References

[1] Spreiter, John R., *The Aerodynamic Forces on Slender Plane and Cruciform-Wing and Body Combinations*, NACA Report 962, 1950.

[2] Morikawa, George, *Supersonic Wing-Body Lift*, Journal of the Aeronautical Sciences, Vol. 18, No. 4, pp. 217–228, April, 1951.

Calculation of Local Heat-Transfer Coefficients on Slender Surfaces of Revolution by the Mangler Transformation

Shao-Yen Ko
Senior Research Scientist, Minneapolis-Honeywell Regulator Company, Hopkins, Minn.

August 16, 1957

Introduction

The heat transfer by convection from slender surfaces of revolution in axisymmetrical flow is of current interest with regard to projectiles, airplane fuselages, rocket motors, etc. At sufficiently high altitudes and speeds laminar boundary layers can exist at very high Reynolds Numbers. For a laminar boundary layer, the velocity and temperature profiles, momentum and displacement thicknesses, and wall shear stress can be evaluated by using the Mangler transformation.[4] This enables direct use of the solution for flows over a two-dimensional body with a free-stream velocity distribution for the determination of the boundary-layer quantities in the three-dimensional case. This paper extends the Mangler transformation into the evaluation of the local heat-transfer coefficient on slender three-dimensional surfaces of revolution in axisymmetrical flow. The mean heat-transfer coefficient over the entire surface can be evaluated by integration. A typical example of this transformation technique is given for the case of laminar heat transfer from semi-ellipsoidal surfaces of fineness ratio 4.

Mangler Transformation

The three-dimensional body with a given pressure gradient was transformed to a related two-dimensional body by means of the following transformation variables

$$\bar{x} = \int_0^x [K^2 r_w^2(x)/L^2]\, dx \tag{1}$$

$$\bar{y} = [K r_w(x)/L]\, y \tag{2}$$

Where x was measured from the forward stagnation point along a meridian profile, y was measured from the surface of the body along a normal; r_w was the radial coordinate of the body of revolution in a meridional plane and L was its total length. The barred variables are coordinates for the equivalent two-dimensional body. K is an arbitrary constant.

Furthermore, it was assumed that

$$p(x, y) = \bar{p}(\bar{x}, \bar{y}) \tag{3}$$

and

$$T(x, y) = \bar{T}(\bar{x}, \bar{y}) \tag{4}$$

Calculation of Local Coefficients of Heat Transfer

The theoretical calculations predicted the distribution of the local coefficients of heat transfer assuming the constant properties and incompressible flow. The method utilized the Mangler transformation as a basis. This enabled using directly the wedge-type flow solutions for the corresponding two-dimensional surface in the determination of the boundary-layer quantities for the three-dimensional case.

The pressure distribution used in this example calculation for flow past a semi-ellipsoidal body with axis ratio of 1:4 was the theoretical approximation given by McNown and Hsu.[3] The corresponding velocity distribution at the outer edge of the boundary came from the pressure distribution by means of the Bernoulli equation

$$U^* = U/U_0 = 1 - [(p - p_0)/(U_0^2/2)]^{1/2} \tag{5}$$

In the evaluation of local heat-transfer coefficients on the surface of the semi-ellipsoidal body, 25 calculating stations were chosen along its major axis with finer steps near the stagnation point. The dimensionless values of $\bar{x}^*$ for the two-dimensional case were obtained from Eq. (1) by graphic integration at each calculating station. The Euler Number of the equivalent two-dimensional surface was evaluated at each calculating station from the definition

$$\bar{m} = (\bar{x}^*/\bar{U}^*)\,(d\bar{U}^*/d\bar{x}^*) \tag{6}$$

For each Euler Number $\bar{m}$, there is a corresponding wedge. The graphic results by Brown[1] gave the heat-transfer parameter $f(\bar{m})$ for wedge flow, here applied as

$$\left[(h\bar{S}/k)/\sqrt{(\bar{U}_0\bar{S}/\nu)}\right]\left[\sqrt{(\bar{x}/\bar{S})}/\sqrt{(\bar{U}/\bar{U}_0)}\right] = f(\bar{m}) \tag{7}$$

where S was the total length of the body of revolution measured from stagnation point along the meridian profile.

The last step of the calculations was to carry out the inverse transformation to get the heat-transfer parameter for the three-dimensional case from the values for the two-dimensional case. The following relations between the two-dimensional quantities and the three-dimensional quantities exist:

For Two-Dimensional Case		*For Three-Dimensional Case*
$\bar{S}$	=	S
$\bar{h}$	=	h/Kr_w^*
$\bar{U}_0$	=	U_0
$\bar{U}$	=	U
$\bar{x}$	=	$\int_0^x K^2 r_w^{*2}\, dx$

(8)

Substitution of Eq. (8) into Eq. (7) yielded the local heat-transfer parameters at each calculating station on the surface of the semi-ellipsoidal body as

$$\frac{N_{Nu}}{N_{Re,s}} = \frac{hS/k}{\sqrt{(U_0S)/\nu}} = \sqrt{\frac{U}{U_0}} \cdot \frac{\bar{S}/L}{\sqrt{\int_0^{x^*} (r_w^{*2}\, dx^*)/r_w^{*2}}} \cdot f(\bar{m}) \tag{9}$$

Fig. 1 presents the final results of local heat-transfer parameters on the surface of the semi-ellipsoidal body. Local heat-transfer parameters of a flat plate based on Eq. (10) also appear in this figure.

$$(hS/k)/(U_0S/\nu)^{1/2} = 0.292/(x/S)^{1/2} \tag{10}$$

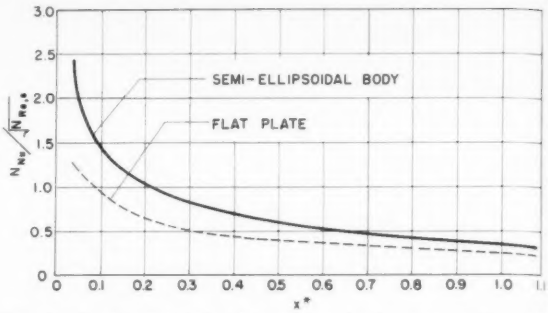

Fig. 1. Local coefficients of heat transfer from semi-ellipsoidal surfaces of fineness ratio 4 for Prandtl Number of 0.71.

Integrating the theoretical local coefficients determines the mean coefficients.

A mean coefficient of heat transfer around a body of revolution is by definition

$$h_m = (2\pi/A)\int_0^S h\, r_w\, dx \tag{11}$$

The result of this integration is expressed as

$$h_m S/k = C(U_\infty S/\nu)^{1/2} (\nu/\alpha)^{1/3} \quad (12)$$

For the present example of semi-ellipsoidal surfaces of fineness ratio 4, the value of C was found to be 0.672. This value has been compared with the mass-transfer experimental results obtained by Ko and Sogin.[2] The presented calculation gave results 10 per cent lower than their experimental values. In view of the approximative nature of this calculation, the agreement was considered satisfactory.

References

[1] Brown, W. B., *Exact Solution of the Laminar Boundary Layer Equations for a Porous Plate with Variable Fluid Properties and a Pressure Gradient in the Main Stream*, Proc. of The First U.S. National Congress of Applied Mechanics, 843–852, 1951.

[2] Ko, Shao-Yen, and Sogin, H. H., *Laminar Mass and Heat Transfer from Ellipsoidal Surfaces of Fineness Ratio 4 in Axisymmetrical Flow*, ASME Paper No. 57-SA-44 to be published in ASME Transactions.

[3] McNown, J. S., and Hsu, E. Y., *Pressure Distribution from Theoretical Approximations of the Flow Pattern*, Heat Transfer and Fluid Mechanics Institute, Berkeley, Calif., 65–76, 1949.

[4] Mangler, W., *Zustammenhang Zwischen ebenen und rotations-symmetrischen Grenschichten in kompressiblen Flussigkeiten*, ZAMM, Vol. 28, 1948.

Thermal Stresses in a Circular Bulkhead Subjected to a Radial Temperature Distribution

Marvin Forray and Melvin Zaid

Scientific Research Staff, Republic Aviation Corporation, Farmingdale, N.Y.

August 21, 1957

Summary

The purpose of this note is to determine the thermal stress in an unrestrained circular bulkhead (Fig. 1) consisting of a web and a cap assembly subjected to a general axially symmetrical radial temperature distribution. The frequently occurring case of a parabolic temperature distribution, which includes linearly varying and uniform temperatures, is considered in detail. The special case of a centrally located "hot spot"[1] is included in the general solution. In actual practice the bulkhead is attached to the outer shell of the fuselage of the aircraft and additional stresses are induced.[2]

General Solution

The differential equation[3] of a disc subjected to an axially symmetrical temperature distribution is

$$\nabla^4\phi = -\alpha E \nabla^2 T \quad (1)$$

where ϕ, α, E are respectively the Airy stress function, the coefficient of linear expansion, and the flexural modulus.

The components of stress are determined from

$$\sigma_r = (1/r)(d\phi/dr), \quad \sigma_\theta = (d^2\phi/dr^2), \quad \tau_{r\theta} = 0 \quad (2)$$

The stress-strain relations are

$$\epsilon_r = (du/dr) = (1/E)(\sigma_r - \nu\sigma_\theta) + \alpha T \quad (3)$$

and

$$\epsilon_\theta = (u/r) = (1/E)(\sigma_\theta - \nu\sigma_r) + \alpha T \quad (4)$$

where u is the radial displacement.

It can be shown that

$$\phi = A \log r + Br^2 \log r + cr^2 + D - \alpha E \int (dr/r) \int Trdr \quad (5)$$

is the complete solution of Eq. (1). Since the stresses and displacements are unaffected by D, it is taken to be zero.

Considering the case of a web without a central hole, the condition of finite stress at $r = 0$, requires $A = B = 0$. Thus the web stress function becomes

$$\phi_1 = c_1 r^2 - \alpha_1 E_1 \int (dr/r) \int Trdr \quad (6)$$

c_1 is to be determined from the associated stress or displacement conditions at $r = a$.

In using Eq. (5) for the cap stress function, the stress or displacement boundary conditions must be satisfied at $r = a$ and $r = b$. In addition it is necessary to insure that the displacement (u) obtained from Eqs. (3) and (4) be identical. From Eqs. (2), (3), (4), and (5) the difference between these radial displacements is

$$\Delta = 4Br/E \quad (7)$$

Setting $\Delta = 0$ and hence $B = 0$, the cap stress function becomes

$$\phi_2 = A_2 \log r + c_2 r^2 - \alpha_2 E_2 \int (dr/r) \int Trdr \quad (8)$$

The stresses in the web and cap are then evaluated by use of Eq. (2) and the associated stress functions. These are

$$\sigma_{r_1} = 2c_1 - (\alpha_1 E_1/r^2) \int Trdr \quad (9)$$

$$\sigma_{\theta_1} = 2c_1 + (\alpha_1 E_1/r^2) \int Trdr - \alpha_1 E_1 T \quad (10)$$

$$\sigma_{r_2} = (A_2/r^2) + 2c_2 - (\alpha_2 E_2/r^2) \int Trdr \quad (11)$$

$$\sigma_{\theta_2} = -(A_2/r^2) + 2c_2 + (\alpha_2 E_2/r^2) \int Trdr - \alpha_2 E_2 T \quad (12)$$

where the subscripts 1 and 2 refer to web and cap, respectively.

For the special cap and web combination shown in Fig. 1, the boundary conditions are

$$t_1\sigma_{r_1}(a) = t_2\sigma_{r_2}(a) \quad (13)$$

$$\sigma_{r_2}(b) = 0 \quad (14)$$

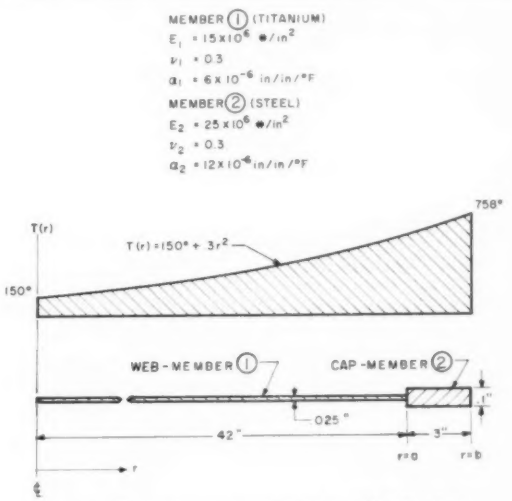

Fig. 1. Structure and temperature distribution.

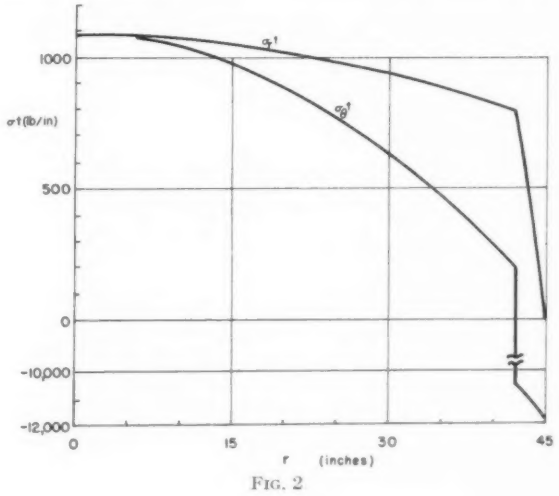

Fig. 2

$$u_1(a) = u_2(a) \tag{15}$$

where the last condition can be replaced by

$$\epsilon_{\theta_1}(a) = \epsilon_{\theta_2}(a) \tag{16}$$

Using Eqs. (4), (16), and (9) to (14) inclusive, the values of the coefficients are determined to be

$$A_2/b^2\alpha_2E_2T^*(b) = 1 - [2c_2/\alpha_2E_2T^*(b)] \tag{17}$$

$$\frac{2c_1}{\alpha_2E_2T^*(b)} = \left(\frac{\alpha_1}{\alpha_2}\frac{E_1}{E_2} - \frac{t_2}{t_1}\right)\frac{T^*(a)}{T^*(b)} + \left(\frac{b}{a}\right)^2\frac{t_2}{t_1} - \left(\frac{t_2}{t_1}\right)\left[\left(\frac{b}{a}\right)^2 - 1\right]\frac{2c_2}{\alpha_2E_2T^*(b)} \tag{18}$$

$$-\frac{2c_2}{\alpha_2E_2T^*(b)} = \frac{\left[(1+\nu_2) + (1-\nu_1)\dfrac{t_2}{t_1}\dfrac{E_2}{E_1} - 2\dfrac{\alpha_1}{\alpha_2}\right]\dfrac{T^*(a)}{T^*(b)} - \left(\dfrac{b}{a}\right)^2\left[\dfrac{t_2}{t_1}\dfrac{E_2}{E_1}(1-\nu_1) + (1+\nu_2)\right]}{\left(\dfrac{b}{a}\right)^2(1+\nu_2) + (1-\nu_2) + \dfrac{t_2}{t_1}\left(\left(\dfrac{b}{a}\right)^2 - 1\right)(1-\nu_1)\dfrac{E_2}{E_1}} \tag{19}$$

where

$$T^*(r) = (1/r^2)\int Trdr \tag{20}$$

Numerical Illustration

For the purposes of illustration consider the structure of Fig. 1. The web and cap are assumed to be made of titanium and stainless steel respectively. The given geometrical and physical properties, and temperature distribution are indicated in Fig. 1. The resulting stress distribution is shown in Fig. 2.

References

[1] Parkes, E. W., *The Stresses in a Plate Due to a Local Hot Spot*, Aircraft Eng., pp. 67–69, March, 1957.

[2] Forray, M. J., and Switzky, H., *Thermal Stresses in a Solid Circular Bulkhead Subjected to a General Temperature Distribution in the Radial Direction*, Republic Aviation Corporation, Report No. E-SAM-17, May, 1956.

[3] Timoshenko, S., and Goodier, J. N., *Theory of Elasticity;* McGraw-Hill Book Company, Inc., N. Y. 1951.

Boundary-Layer Correction in Supersonic Nozzle Scaling

Abraham Kogan

Department of Aeronautical Engineering, Israel Institute of Technology, Haifa, Israel

September 3, 1957

Symbols

- l = length of supersonic part of nozzle
- M = Mach Number
- N = positive integer
- u = velocity
- x = length parameter
- y = distance from wall
- δ = boundary-layer thickness
- δ^* = displacement thickness
- θ = momentum thickness
- ν = kinematic viscosity
- ρ = density
- τ_0 = local friction stress at the wall
- 1 = value outside boundary layer
- $\bar{\ }$ = value corresponding to arithmetic mean temperature between wall and free stream

Discussion

Using von Kármán's Momentum integral for compressible flow, Tucker[1, 2] has obtained the following results for the boundary-layer development in a supersonic tunnel:

$$[\delta(x)/l] = (1/F)\left\{[\delta(0)/l] + \int_0^{x/l} F(\delta/\theta)\,(\bar{\rho}/\rho_1)\,(\tau_0/\bar{\rho}u_1^2)d(x/l)\right\} \tag{1}$$

and

$$[\delta^*(x)/l] = (1/G)\left\{[\delta^*(0)/l] + \int_0^{x/l} G(\delta^*/\theta)\,(\bar{\rho}/\rho_1)\,(\tau_0/\bar{\rho}u_1^2)d(x/l)\right\} \tag{2}$$

The ratios δ/θ and δ^*/θ were calculated by Tucker as functions of the local Mach Number M by postulating the power law

$$(u/u_1) = (y/\delta)^{1/N}$$

They are tabulated in reference 2 as functions of M for different values of N.

The parameters F, G, and $\bar{\rho}/\rho_1$ in Eqs. (1) and (2) are also functions of M only:

$$F = \frac{\theta/\delta}{(\theta/\delta)_{M=1}}\exp.\int_1^M \frac{2 - M^2 + (\delta^*/\delta)}{M\{1 + [(\gamma-1)/2]M^2\}}\,dM$$

$$G = [(\delta/\delta^*)/(\delta/\delta^*)_{M=1}]F$$

$$\bar{\rho}/\bar{\rho}_1 = 1/\{1 + [(\gamma-1)/4]M^2\}$$

Only the skin friction coefficient $\tau_0/(1/2)\bar{\rho}u_1^2$ varies with the Reynolds Number based on the distance x from the throat. We observe, however, that the variation of the friction coefficient with x is very slow.

$$\tau_0/(1/2)\bar{\rho}u_1^2 = 0.0262\left(\frac{\bar{\nu}}{u_1x}\right)^{1/7}$$

If we neglect the variation of $\tau_0/(1/2)\bar{\rho}u_1^2$ with x and replace it by a suitable constant, the resulting approximations for Eqs. (1) and (2) will contain integrands that depend on x only implictly through M.

Let us consider a family of nozzles obtained by proportional scaling of a given nozzle. The length parameter x/l will be the same function of M for the whole family. We can therefore represent the boundary-layer development for any one of these nozzles by the following approximate form of Eqs. (1) and (2):

$$[\delta(x)/l] = [1/F(M)]\left\{[\delta(0)/l] + \int_0^M f(M)dM\right\}$$

$$(\delta^*/l) = [1/G(M)]\left\{[\delta^*(0)/l] + \int_0^M g(M)dM\right\}$$

with

$$f(M) = CF(\delta/\theta)\,(\bar{\rho}/\rho_1)\,[d(x/l)/dM]$$

$$g(M) = CG(\delta^*/\theta)\,(\bar{\rho}/\rho_1)\,[d(x/l)/dM]$$

where C is the constant approximate value of the friction coefficient.

Thus, it appears that when a nozzle is developed from a given prototype by geometrical scaling of the perfect-fluid-flow wall streamline, the boundary-layer correction may be calculated to a fair approximation by proportion from the prototype boundary-layer correction.

References

[1] Tucker, M., *Approximate Turbulent Boundary-Layer Development in Plane Compressible Flow along Thermally Insulated Surfaces with Application to Supersonic Tunnel Contour Correction*, NACA TN 2045, 1950.

[2] Tucker, M., *Approximate Calculation of Turbulent Boundary-Layer Development in Compressible Flow*, NACA TN 2337, 1951.

Hypersonic Flow Around a Sphere

R. D. Linnell
Staff Scientist, Convair Scientific Research Laboratory, San Diego, Calif.
September 4, 1957

SUMMARY

This note presents an estimate of the stagnation-point surface-velocity gradient and the axial shock detachment distance for hypersonic flow around a sphere. Real gas effects are taken into account. The predicted values correlate well with available experimental data which are for perfect gas conditions.

SYMBOLS

a, b, c = constants, Eq. (9)
D = diameter of the sphere
f = function of θ
g = function of r
k = ρ_∞/ρ_s
p = pressure
r = radial coordinate, distance from center of sphere
R = shock radius, radial coordinate of shock
u = radial component of velocity
U_∞ = free-stream velocity
v = circumferential component of velocity
β = $(2/D)v'_{\theta=0}$, stagnation-point surface velocity gradient
δ = $r - (D/2)$, radial distance from sphere surface
γ = ratio of specific heats
λ = ρ_s/ρ_t
ρ = mass density
θ = polar coordinate angle, measured from stagnation point

Subscripts

∞ = conditions in free stream
s = conditions just behind the shock
t = stagnation point conditions
0 = conditions at the axis, $\theta = 0$

primes denote differentiation

THE VELOCITY GRADIENT

THE DENSITY in the flow between the shock and the sphere is assumed to be constant at ρ_t. This permits use of the incompressible Bernoulli equation along the axis

$$p = p_t - (\rho_t u^2/2) \tag{1}$$

Since the shock is normal at the axis, the normal shock equations give $u_s = -kU_\infty$ and $p_s = p_\infty + (1 - k)\,\rho_\infty U_\infty^2$ directly behind the shock. These values are substituted into Eq. (1) to obtain the stagnation pressure.

$$p_t = p_\infty + \{\rho_\infty U_\infty^2\,[2\lambda(1 - k) + k]/2\lambda\} \tag{2}$$

If the surface pressure coefficient distribution is assumed to be Newtonian, giving

$$p = p_t \cos^2\theta + p_\infty \sin^2\theta \tag{3}$$

then the surface velocity obtained from the Bernoulli equation on the surface is

$$v = U_\infty \sqrt{2\lambda k(1 - k) + k^2}\,\sin\theta \tag{4}$$

and β is

$$\beta = (2/D)U_\infty \sqrt{2k\lambda(1 - k) + k^2} \tag{5}$$

If λ is set equal to unity ($\rho_t = \rho_s$) in Eq. (5), the Li and Geiger[1] result is obtained. Values calculated from Eq. (5) are shown in Fig. 1 along with test data points[2] for perfect gas conditions in a wind tunnel. The correlation for perfect gas is improved by using perfect gas values of λ for $\gamma = 1.4$.

The effect of using real gas values of λ, obtained from Feldman,[3] is to decrease β about 5 per cent.

THE DETACHMENT DISTANCE

The shock detachment distance corresponding to the surface conditions obtained above is obtained by starting with the continuity equation

$$\sin\theta\,(\partial u r^2/\partial r) + r\,(\partial v \sin\theta/\partial\theta) = 0 \tag{6}$$

If v is assumed to be of the form $U_\infty f(\theta)g'(r)/r$, then according to Eq. (4) $f = \sin\theta$ so

$$v = U_\infty \sin\theta g'(r)/r \tag{7}$$

From Eq. (6) it is found that

$$u = -2U_\infty \cos\theta g(r)/r^2 \tag{8}$$

For g assume a three term series in δ

$$g = a + b\delta + c\delta^2 \tag{9}$$

The constant a is zero since the radial velocity must be zero at the surface of the sphere. According to Eqs. (4) and (7) b must be given by

$$b = (D/2)\sqrt{2\lambda k(1 - k) + k^2} \tag{10}$$

Additional boundary conditions can be obtained at the shock, on the axis where $\delta = \Delta_0$. From $u_s = -kU_\infty$ and Eq. (8)

$$2b\Delta_0 + 2c\Delta_0^2 = k\,[\Delta_0 + (D/2)]^2 \tag{11}$$

Another relation between Δ_0 and c can be obtained by matching

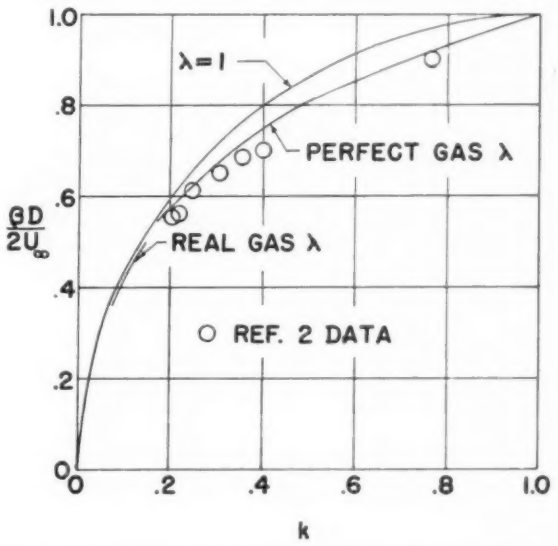

FIG. 1. Stagnation-point surface-velocity gradient parameter.

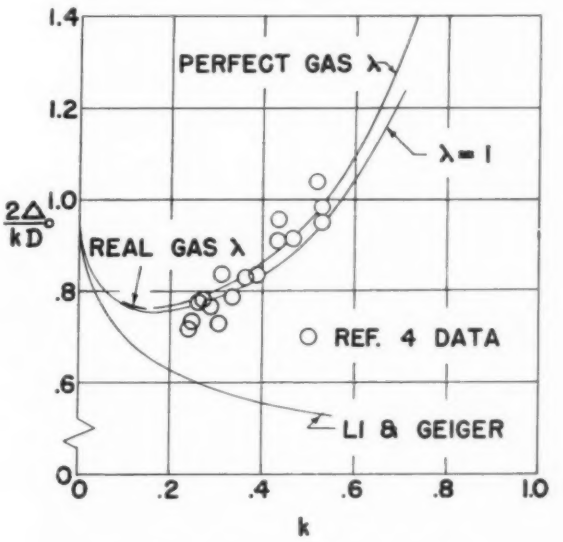

FIG. 2. Shock detachment distance parameter.

$dv/d\theta$ along the shock evaluated at the axis. The oblique shock relations provide

$$dv/d\theta_{,s} = U_\infty[1 - (1 - k)(R_0''/R_0)] \tag{12}$$

where R_0'' is unknown. But for a sphere the shock is almost spherical near $\theta = 0$ and therefore R_0'' is assumed to be zero.

A fourth condition is then obtained by equating the shock relation value to the value obtained from Eq. (7).

$$b + 2c\Delta_0 = \Delta_0 + (D/2) \tag{13}$$

Elimination of c between Eqs. (11) and (13) gives the equation for the shock detachment distance at the axis

$$\frac{2\Delta_0}{D} = \frac{\sqrt{[1 + (2b/D)]^2 - 4k(2b/D)} - [1 + (2b/D) - 2k]}{2(1 - k)} \tag{14}$$

where $2b/D$ is given by Eq. (10).

Calculated values of the detachment parameter $2\Delta_0/kD$ are shown in Fig. 2. The correlation with the test data[3] obtained under perfect gas conditions is good for both b based on $\lambda = 1$ and for perfect gas λ. The effect of using real gas values of λ is to increase Δ_0 about 2 per cent. The theoretical result of Li and Geiger[1] is also shown.

References

[1] Li, T. Y., and Geiger, R. E., *Stagnation Point of a Blunt Body in Hypersonic Flow*, Journal of the Aeronautical Sciences, Vol. 24, No. 1, p. 19, January, 1957.

[2] Korobkin, I., and Gruenwald, K. H., *Investigation of Local Laminar Heat Transfer on a Hemisphere for Supersonic Mach Numbers at Low Rates of Heat Flux*, Journal of the Aeronautical Sciences, Vol. 24, No. 3, p. 188, March, 1957.

[3] Feldman, S., *Hypersonic Gas Dynamic Charts for Equilibrium Air*, AVCO Research Laboratory, January, 1957.

[4] Heybey, W. H., *Shock Distances in Front of Symmetrical Bodies*, Navord Report 3591, December, 1953.

Creep Buckling of Tubes in Torsion

Iain Finnie

Materials Engineering and Corrosion Department, Shell Development Company, Emeryville, Calif.

September 5, 1957

There is little published information on the creep buckling of members other than pin ended columns. Even in this relatively simple case the complexity of a complete creep-buckling analysis has led to the use of approximate solutions. In the simplest of these the effects of column eccentricity are ignored, and the tangent modulus of the inelastic buckling solution is replaced by a time-dependent tangent modulus.[1] The object of the present note is to indicate the extension of the time-dependent modulus approach to other types of buckling and, in particular, to compare the prediction for torsional buckling with experiment.

Inelastic buckling solutions may be obtained by replacing the elastic modulus in the elastic buckling equations by an effective modulus. In general, the effective modulus involves both the tangent modulus $E_t = \partial\sigma/\partial\epsilon$ and the secant modulus $E_s = \sigma/\epsilon$ where σ and ϵ are stress and strain.† It is known that when longitudinal bending predominates, as in the familiar Euler column, the effective modulus is the tangent modulus. When longitudinal bending is small compared to twisting, the secant modulus is the effective modulus. Examples approaching this condition are a long cylinder in torsion, a cruciform section column which buckles by twisting, or a long flange with one unloaded edge simply supported. An example, given by Stowell,[2] of the more general case is the square plate loaded as a column for which the effective modulus is $(0.114\,\sigma/\epsilon + 0.886\,\partial\sigma/\partial\epsilon)$.

When only the tangent modulus is involved, we may write the critical stress for inelastic buckling as $\sigma_{cr} = C E_t$ where C is some function of the specimen dimensions. Writing the total strain under creep conditions of the column material as $\epsilon = f(\sigma, t, E)$ where t is time and E the elastic modulus, we find $\sigma_{cr} = C \div (\partial f/\partial\sigma)$ from which σ_{cr} is obtained as a function of time. The application of this type of solution to pin ended columns has been discussed by Carlson.[1]

Following the same procedure when only the secant modulus is involved, we write $\sigma_{cr} = C E_s$ or $\epsilon_{cr} = C$ and the stress disappears from the buckling equation. This implies that for buckling predominantly by twisting there is a critical strain independent of the creep behavior of the material. The time at which the critical strain is reached will, of course, depend on the stress and material properties. For the more general case in which both secant and tangent modulus are involved, we would replace both these quantities by their time dependent values.

A prediction of torsional buckling will illustrate the preceding method. For hollow cylinders, length L, wall thickness h, and radius R, such that $50\ h/R < (L/R)^2 < 10\ R/h$, Batdorf[3] has given the critical shear stress for elastic buckling as

$$\tau_{cr} = 0.747\ E(h/R)^{5/4}(R/L)^{1/2} \tag{1}$$

Gerard[4] has stated that the inelastic buckling stress may be obtained from Eq. (1) if E is replaced by $E_s(1 - \mu_e)^{3/4}/(1 - \mu)^{3/4}$. Taking μ_e and μ, the elastic and plastic values of Poisson's ratio as 0.3 and 0.5, Eq. (1) becomes

$$\tau_{cr} = 0.865\ E_s(h/R)^{5/4}(R/L)^{1/2} \tag{2}$$

The secant modulus $E_s = \sigma^*/\epsilon^*$ may be written in terms of the shear stress τ and shear strain γ. Remembering that for torsion of a tube, the principal stresses and strains are $\sigma_1 = -\sigma_2 = \tau$, $\epsilon_1 = -\epsilon_2 = \gamma/2$, and using the invariants defined in the preceding footnote, we obtain $E_s = 3\tau/\gamma$. Substituting into Eq. (2) leads to

$$\gamma_{cr} = 2.6(h/R)^{5/4}(R/L)^{1/2} \tag{3}$$

for the critical shear strain at which torsional buckling should occur.

Since unwanted buckling had troubled the writer during studies of multiaxial stress rupture, several tests were run to investigate the applicability of Eq. (3). Just as with columns, the creep buckling of tubes in torsion is observed as a deformation increasing with time. There is, therefore, some difficulty in defining a time or strain at which it can be said that creep buckling has occurred. One indication of torsional buckling is the decrease in axial length of the tube being twisted. Measurements of this quantity as a function of the angle of twist are shown in Fig. 1 for a plastic tube and for aluminum tubes under three different twisting moments. The angle of twist-time curves for the aluminum tubes are shown in Fig. 2. In the case of the plastic tube the total time of test, 0.2 hour, was too short to enable this relation to be obtained. The specimen dimensions are $L = 5$ in., $h = 0.100$ in., $R_{average} = 0.75$ in., and the corresponding critical angle of twist $\theta_{cr} = \gamma_{cr}\ L/R$ predicted by Eq.

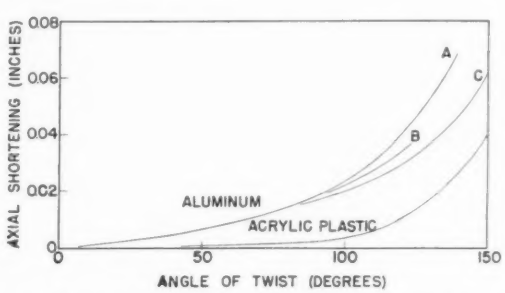

Fig. 1. Axial shortening as a function of angle of twist for one plastic tube and three aluminum tubes.

† Under multiaxial stress, σ and ϵ must be replaced by the invariant quantities

$$\sigma^* = (1/\sqrt{2})\,[(\sigma_1 - \sigma_2)^2 + (\sigma_2 - \sigma_3)^2 + (\sigma_3 - \sigma_1)^2]^{1/2}$$

$$\epsilon^* = (\sqrt{2}/3)\,[(\epsilon_1 - \epsilon_2)^2 + (\epsilon_2 - \epsilon_3)^2 + (\epsilon_3 - \epsilon_1)^2]^{1/2}$$

written here in terms of principal stresses and strains.

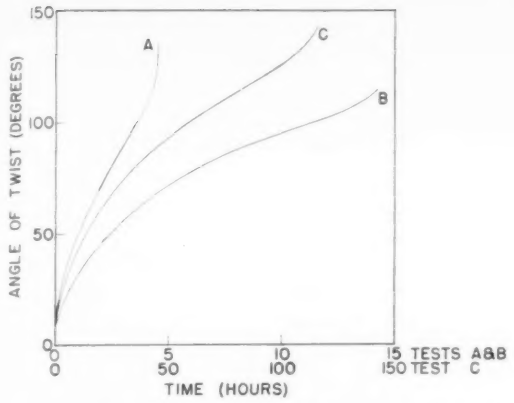

FIG. 2. Angle of twist as a function of time for three aluminum tubes.

(3) is about 31°. At this angle, buckling could only be detected as a slight ellipticity of cross section (perpendicular diameters of 1.600 in. differing by 0.010 in.). With increasing angle of twist the ellipticity and axial shortening increase.

As another example we may take the specimen dimensions ($L = 2.3$ in., $H = 0.03$ in., $R_{average} = 0.265$ in.) used by Johnson, Mathur, and Henderson[5] for multiaxial rupture studies. Eq. (3) predicts $\gamma_{cr} = 0.058$ while for a copper specimen which failed in rupture after 5,442 hours these authors reported a rupture shear strain of $\gamma = 0.144$.

We would conclude that the general form of the curves in Figs. 1 and 2 lends support to the hypothesis that torsional buckling should occur at shear strains depending only on the specimen dimensions and independent of stress or the material tested. However, the critical strain predicted by the secant modulus may underestimate the shear strain at which creep buckling becomes significant.

REFERENCES

[1] Carlson, R. L., *Time Dependent Tangent Modulus Applied to Column Creep Buckling*, J. Appl. Mech., Vol. 23, p. 390, 1956.

[2] Stowell, E. Z., *A Unified Theory of the Plastic Buckling of Columns and Plates*, NACA Technical Report No. 898, 1948.

[3] Batdorf, S. B., *A Simplified Method of Elastic Stability Analysis for Thin Cylindrical Shells (I), Donnell's Equations*, NACA TN 1341, 1947.

[4] Gerard, G., *Compressive and Torsional Buckling of Thin Walled Cylinders in Yield Region*, NACA TN 3726, 1956.

[5] Johnson, A. E., Henderson, J., and Mathur, V. D., *Combined Stress Creep Fracture of Commercially Pure Copper at 250°C.*, The Engineer, Vol. 196, pp. 261–265, 299–301, 1956.

On the Stream Functions in Nonsteady Three-Dimensional Flow

M. Z. v. Krzywoblocki
Professor, Panel on Fluid Dynamics, University of Illinois, Urbana, Ill.
September 9, 1957

CONSIDER the continuity equation

$$\rho_{,t} + (\rho u)_{,x} + (\rho v)_{,y} + (\rho w)_{,z} = 0$$

The stream functions satisfying identically this equation are:

(1) One-dimensional nonsteady flow (t, x)

$$\rho = \psi_{,x}; \quad (\rho u) = -\psi_{,t}; \quad \psi = \psi(x, t)$$

(2) Two-dimensional steady flow (x, y)

$$\rho u = \psi_{,y}; \quad \rho v = -\psi_{,x}; \quad \psi = \psi(x, y)$$

(3) Two-dimensional nonsteady flow (t, x, y)

$$\rho = \frac{D(\psi, \vartheta)}{D(x, y)}; \quad \rho u = \frac{D(\psi, \vartheta)}{D(y, t)};$$

$$\rho v = \frac{D(\psi, \vartheta)}{D(t, x)}; \quad \psi = \psi(x, y, t); \quad \vartheta = \vartheta(x, y, t);$$

$$\frac{D(\psi, \vartheta)}{D(x, y)} = \begin{vmatrix} \psi_{,x} & \psi_{,y} \\ \vartheta_{,x} & \vartheta_{,y} \end{vmatrix} = \psi_{,x}\vartheta_{,y} - \psi_{,y}\vartheta_{,x}, \quad \text{etc.}$$

(4) Three-dimensional steady flow (x, y, z)

$$\rho u = \frac{D(\psi, \vartheta)}{D(y, z)}; \quad \rho v = \frac{D(\psi, \vartheta)}{D(z, x)}; \quad \rho w = \frac{D(\psi, \vartheta)}{D(x, y)};$$

$$\psi = \psi(x, y, z); \quad \vartheta = \vartheta(x, y, z);$$

(5) Three-dimensional nonsteady flow (t, x, y, z)

$$\rho = \frac{D(\psi, \vartheta, \epsilon)}{D(x, y, z)}; \quad \rho u = -\frac{D(\psi, \vartheta, \epsilon)}{D(y, z, t)};$$

$$\rho v = \frac{D(\psi, \vartheta, \epsilon)}{D(z, t, x)}; \quad \rho w = -\frac{D(\psi, \vartheta, \epsilon)}{D(t, x, y)};$$

$$\frac{D(\psi, \vartheta, \epsilon)}{D(x, y, z)} = \begin{vmatrix} \psi_{,x} & \psi_{,y} & \psi_{,z} \\ \vartheta_{,x} & \vartheta_{,y} & \vartheta_{,z} \\ \epsilon_{,x} & \epsilon_{,y} & \epsilon_{,z} \end{vmatrix};$$

$$\psi = \psi(x, y, z, t); \quad \epsilon = \epsilon(x, y, z, t), \text{ etc.}$$

The stream functions in a three-dimensional steady flow were used by some authors in the past.[1] The more proper name in a nonsteady flow may be the particle function.

REFERENCE

[1] Skobelkin, V. I., *Variational Principles in Hydrodynamics*, Soviet Physics JETP, Vol. 4, No. 1, pp 68–72, February, 1957.

Mass Transfer Cooling at Mach Number 4.8†

B. M. Leadon,* C. J. Scott, and G. E. Anderson
Rosemount Aeronautical Laboratories, University of Minnesota Minneapolis, Minn.
September 9, 1957

MASS-TRANSFER EXPERIMENTS on a 5 mil wire porous cone of 20° total angle have been conducted at $M_\infty = 4.8$ using air and helium injection. Details of the experimental technique are described in references 1 and 2. In the laminar boundary layer the recovery factors and heat-transfer coefficients measured with zero injection agreed within ±6.5 per cent with theory. Transition Reynolds Numbers observed on the porous cone with zero injection were half as large as observed on a smooth, impermeable model of identical geometry in the same channel, but injection of large amounts of air or helium did not cause transition to move forward from its zero-injection position on the porous cone. Distributed roughness of this type apparently does not disturb impermeable wall theory, but it masks whatever effective roughness may be caused by discrete pore injection.

The 12-in. model had a $2^3/_4$-in. solid tip, $1^3/_4$ in. of increasing porosity, and then 3 in. of fairly constant porosity (and laminar boundary layer) to the beginning of the transition region. Local measurements of temperature recovery factors and heat-transfer coefficients plotted against an injection parameter, f_w* (Fig. 1) indicated that the effect of injecting air is well predicted by theory[3] even though the actual injection distribution differed considerably from the assumed $(x^{-1/2})$ distribution.

With helium injection the temperature recovery factors displayed a tendency to rise with f_w* before falling below the zero injection value (see Fig. 2). This tendency has been found

† This research was sponsored by the Office of Scientific Research of the ARDC, USAF, under Contract AF 18 (600)-1226.

* Now with Convair Scientific Research Department, San Diego.

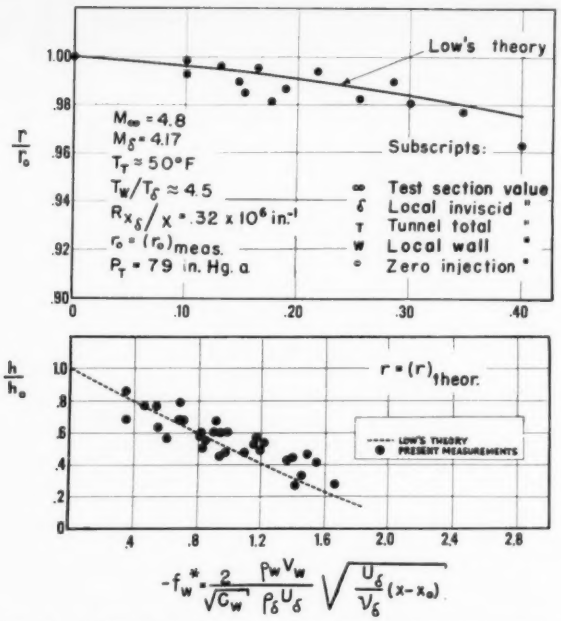

FIG. 1. Effect of air injection upon laminar temperature recovery factors and local heat-transfer coefficients.

theoretically under the assumption of constant Prandtl Number (P_r),[4] but not when P_r variations were considered.[5] Local heat-transfer coefficients with helium injection appear to confirm variable P_r theories although experimental recovery factors were used in reducing the data. For the range of f_w^* in Fig. 2 the measured concentrations of helium at the wall agreed with theoretical predictions,[4, 5] but fell below at higher $f_w^{*\prime}s$. The

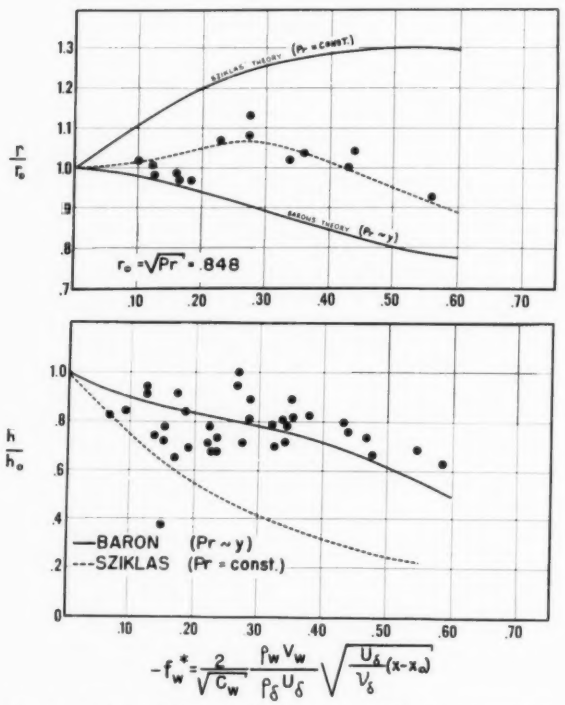
SZIKLAS THEORY (Pr = CONST.)
BARON'S THEORY (Pr ~ y)
$r_0 = \sqrt{Pr} = .848$
—BARON (Pr ~ y)
---SZIKLAS (Pr = const.)
$-f_w^* = \frac{2}{\sqrt{C_w}} \frac{\rho_w V_w}{\rho_\delta U_\delta} \sqrt{\frac{U_\delta}{\nu_\delta (x-x_0)}}$

FIG. 2. Effect of helium injection upon laminar temperature recovery factors and local heat-transfer coefficients.

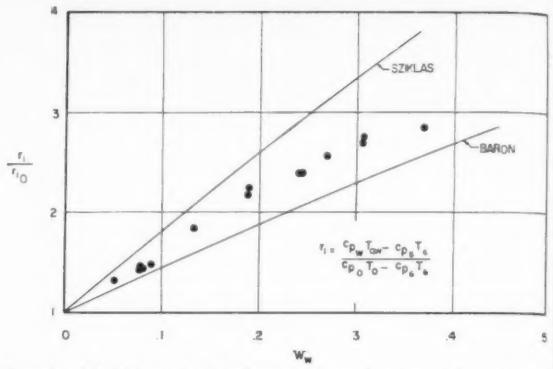

FIG. 3. Variation of enthalpy recovery factors with wall concentration.

variation of enthalpy recovery factors with wall helium mass fraction is shown in Fig. 3.

REFERENCES

[1] Leadon, B. M., and Scott, C. J., *Transpiration Cooling Experiments in a Turbulent Boundary Layer at M = 3*, Journal of the Aeronautical Sciences, Readers' Forum, Vol. 23, No. 8, pp. 798, 799, August, 1956.

[2] Leadon, B. M., Scott, C. J., and Anderson, G. E., *Mass-Transfer Cooling of a 20° Porous Cone at M = 5*, Univ. of Minnesota Report No. 143, 1957.

[3] Low, G. M., *The Compressible Laminar Boundary Layer with Fluid Injection*, NACA TN 3404 1955.

[4] Sziklas, E. A., *An Analysis of the Compressible Laminar Boundary Layer with Foreign-Gas Injection*, United Aircraft Corporation Report SR-0539-8, 1956.

[5] Baron, J. R., *The Binary-Mixture Boundary Layer Associated with Mass Transfer Cooling at High Speeds*, MIT Tech. Report 160, 1956.

Boundary-Layer Slip Solutions for a Flat Plate*

Hidenori Hasimoto
Assistant Professor, Department of Aeronautics, University of Kyoto, Kyoto, Japan
September 10, 1957

THE FLAT-PLATE boundary-layer problem with slip has been studied by several authors. In this problem we must solve the boundary-layer equations

$$u(\partial u/\partial x) + v(\partial u/\partial y) = \nu(\partial^2 u/\partial y^2) \quad (1)$$

$$(\partial u/\partial x) + (\partial v/\partial y) = 0 \quad (2)$$

taking into account the boundary conditions

$$u = h(\partial u/\partial y), \quad v = 0 \quad \text{at } y = 0 \quad (3)$$

$$u \to 1 \quad \text{at } x = 0 \text{ and as } y \to \infty \quad (4)$$

where h is the slip parameter proportional to the mean free path length.

Recently Schaaf and Sherman[1] discussed the qualitative nature of the flow by solving the Rayleigh equation (or Oseen equation) corresponding to Eq. (1). Bell[2] examined the solutions of this simplified equation and showed the nonuniformity of the local skin friction as $x \to 0$ and $h \to 0$.

In this note I want to show a direct method of approach to Eqs. (1) to (4), using the von Mises transformation.

Taking the stream function ψ, such that

$$u = \partial\psi/\partial y, \quad v = -\partial\psi/\partial x \quad (5)$$

and x as two independent variables, Eqs. (1) to (4) are trans-

* The author wishes to express his cordial thanks to Professors I. Imai and K. Tamada for their continual encouragement throughout this work.

formed to

$$\partial u/\partial x = \nu(\partial/\partial\psi)\,[u(\partial u/\partial\psi)] \quad (6)$$

$$\partial u/\partial\psi = 1/h \quad \text{at } \psi = 0 \quad (7)$$

$$u \to 1 \quad \text{as } \psi \to \infty \quad (8)$$

In terms of new independent variables ξ, η

$$\xi = 2\sqrt{\nu x}/h \quad (9)$$

$$\eta = \psi/(2\sqrt{\nu x}) \quad (10)$$

Eqs. (6) to (8) are reduced to another form

$$(\partial/\partial\eta)\,[u(\partial u/\partial\eta)] + 2\eta(\partial u/\partial\eta) = 2\xi(\partial u/\partial\xi) \quad (11)$$

$$\partial u/\partial\eta = \xi \quad \text{at } \eta = 0 \quad (12)$$

$$u = 1 \quad \text{as } \eta \to \infty \quad (13)$$

Assuming that u can be expressed in a power series of ξ

$$u = 1 + \sum_{n=1}^{\infty} \xi^n f_n(\eta) \quad (14)$$

We obtain from Eqs. (11) to (13)

$$L_1[f_1] = f_1'' + 2\eta f_1' - 2f_1 = 0, \quad f_1'(0) = 1, \quad f_1(\infty) = 0 \quad (15)$$

$$L_2[f_2] = f_2'' + 2\eta f_2' - 4f_2 = -(f_1'^2 + f_1 f_1''), \quad f_2'(0) = 0, \quad f_2(\infty) = 0 \quad (16)$$

$f_1(\eta)$ is found to be

$$f_1(\eta) = -E_1(\eta) \quad (17)$$

where $E_n(\eta)$ is the repeated integral of the error function

$$E_n(\eta) = i^n \operatorname{erfc}\eta = \int_\eta^\infty E_{n-1}(\eta)d\eta, \quad E_0(\eta) = \operatorname{erfc}\eta = (2/\sqrt{\pi})\int_\eta^\infty e^{-\eta^2}d\eta \quad (18)$$

Introducing f_1 into the right-hand side of Eq. (16), and taking into account the boundary conditions, f_2 can be easily determined to be

$$f_2(\eta) = -(1/2)(E_1^2 + E_0E_2) + (7/4)E_2 \quad (19)$$

Making use of these results the local skin-friction coefficient C_f and the total skin-friction coefficient C_D for a plate of length L are given respectively by

$$C_f = [\mu u(x, 0)/h]/(\rho u_\infty^2/2) = (2\nu/hu_\infty) \times \{1 - (2/\sqrt{\pi})(\sqrt{\nu x}/h\sqrt{u_\infty}) + [(5/4) - (2/\pi)] \times (\nu x/h^2u_\infty) + \ldots\} \quad (20)$$

and

$$C_D = \int_0^L C_f dx \Big/ L = (2\nu/hu_\infty)\{1 - (4/3\sqrt{\pi})(\sqrt{\nu L}/h\sqrt{u_\infty}) + [(5/8) - (1/\pi)](\nu L/h^2u_\infty) + \ldots\} \quad (21)$$

C_f is finite at $x = 0$, in contrast with the Blasius solution corresponding to the case $h = 0$, and is larger than the value expected from the free-molecule flow theory. Further it may be noticed that the value of C_D obtained from the Rayleigh equation is given by[1]

$$C_D = (2\nu/hu_\infty) \times [1 - (4/3\sqrt{\pi})(\sqrt{\nu L}/h\sqrt{u_\infty}) + (\nu L/2h^2u_\infty) + \ldots] \quad (22)$$

which is in accord with Eq. (21) as far as the second term and is larger than Eq. (21) because of the third term. In this respect the Rayleigh solution may be considered to offer a very good approximation to the solution of Eqs. (1) to (4) if $\sqrt{\nu L}/(h\sqrt{u_\infty})$ is small, although in this region Eqs. (1) to (4) must be used with some reservation.

References

[1] Schaaf, S. A., and Sherman, F. S., *Skin Friction in Slip Flow*, Journal of the Aeronautical Sciences, Vol. 21, No. 2, pp. 85–90, 144, February, 1953.

[2] Bell, S., *Studies of Boundary Layer Slip Solutions and Alden's Method for Boundary Layer Correction*, Univ. of California Institute of Engineering Research Tech. Report, No. 20–106, December, 1955.

A Simple Graphical Method for Constructing Two-Dimensional Supersonic Flows by Means of a Drafting Machine

F. Edward Ehlers
Mathematical Services Unit, Physical Research Staff, Boeing Airplane Company, Seattle, Wash.

September 10, 1957

Summary

A simplification of the Puckett field method of characteristics for supersonic two-dimensional flows is explained. By means of special tables given here, an engineer can construct the Mach net rapidly using a drafting machine without any intermediate calculations.

Introduction

PUCKETT[2] HAS DEVELOPED a simple method of designing two-dimensional supersonic nozzles by the method of characteristics. The walls of the nozzle are made up of short, straight sections having the same angle increment at each junction. Considering each vertex as introducing a Prandtl-Meyer expansion through a given angle and resulting in a deflection of the stream of this same angle, one can find the direction of the lines of the Mach net by simple calculations using the tables of the Prandtl-Meyer expansion angle in references 1, 2, and 3. The method described herein is essentially the method of Puckett[1, 2] but special tables are provided which eliminate the necessity of any intermediate calculations. The following discussion explains the use of the special tables given in this note.

Theory

Suppose a parallel uniform stream of air is flowing between two parallel walls at a Mach Number of unity. At the point where the wall turns through an angle, $\Delta\theta$, an expansion will occur. The flow will be accelerated and turned through an angle $\Delta\theta$ in a centered fan region of characteristics or Mach lines. If $\Delta\theta$ is small, say 1°, then the centered fan may be approximated by a single Mach line across which the velocity changes discontinuously. For an angle change of 1°, the Mach angle changes from $\mu = 90°$ to $\mu = 67.574°$ while the flow angle changes from 0° to 1° (see page 504.211–1, reference 2). The direction with respect to the horizontal of the last Mach line of the fan is $67.574° - 1° = 66.574°$. To approximate the centered fan by a single Mach line, we choose the Prandtl-Meyer angle of 1/2° which is the average of the Prandtl-Meyer angles before and after the fan. The Mach angle corresponding to this Prandtl-Meyer angle is $\mu = 72.099°$. The direction of the mean Mach line then is found to be

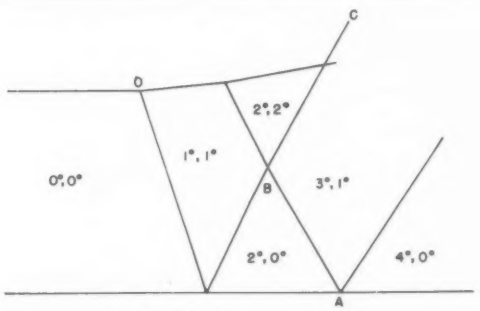

FIG. 1. Mach net construction.

TABLE 1 — $\mu - \theta$ For $\theta > 0$; $\mu + \theta$ For $\theta < 0$ — 1 Degree Steps

ω / θ	0 – 1	1 – 2	2 – 3	3 – 4	4 – 5	5 – 6	6 – 7	7 – 8	8 – 9	9 – 10
0 – 1	71° 36′	70° 36′	69° 36′	68° 36′	67° 36′	66° 36′	65° 36′	64° 36′	63° 36′	62° 36′
1 – 2	63° 57′	62° 57′	61° 57′	60° 57′	59° 57′	58° 57′	57° 57′	56° 57′	55° 57′	54° 57′
2 – 3	56° 27′	55° 27′	54° 27′	53° 27′	52° 27′	51° 27′	50° 27′	49° 27′	48° 27′	47° 27′
3 – 4	49° 01′	48° 01′	47° 01′	46° 01′	45° 01′	44° 01′	43° 01′	42° 01′	41° 01′	40° 01′
4 – 5	41° 39′	40° 39′	39° 39′	38° 39′	37° 39′	36° 39′	35° 39′	34° 39′	33° 39′	32° 39′
5 – 6	34° 20′	33° 20′	32° 20′	31° 20′	30° 20′	29° 20′	28° 20′	27° 20′	26° 20′	25° 20′
6 – 7	27° 03′	26° 03′	25° 03′	24° 03′	23° 03′	22° 03′	21° 03′	20° 03′	19° 03′	18° 03′
7 – 8	19° 48′	18° 48′	17° 48′	16° 48′	15° 48′	14° 48′	13° 48′	12° 48′	11° 48′	10° 48′
8 – 9	12° 34′	11° 34′	10° 34′	9° 34′	8° 34′	7° 34′	6° 34′	5° 34′	4° 34′	3° 34′
9 – 10	5° 21′	4° 21′	3° 21′	2° 21′	1° 21′	0° 21′	359° 21′	358° 21′	357° 21′	356° 21′
10 – 11	358° 08′	357° 08′	356° 08′	355° 08′	354° 08′	353° 08′	352° 08′	351° 08′	350° 08′	349° 08′
11 – 12	350° 56′	349° 56′	348° 56′	347° 56′	346° 56′	345° 56′	344° 56′	343° 56′	342° 56′	341° 56′
12 – 13	343° 46′	342° 46′	341° 46′	340° 46′	339° 46′	338° 46′	337° 46′	336° 46′	335° 46′	334° 46′
13 – 14	336° 38′	335° 38′	334° 38′	333° 38′	332° 38′	331° 38′	330° 38′	329° 38′	328° 38′	327° 38′
14 – 15	329° 32′	328° 32′	327° 32′	326° 32′	325° 32′	324° 32′	323° 32′	322° 32′	321° 32′	320° 32′
15 – 16	322° 28′	321° 28′	320° 28′	319° 28′	318° 28′	317° 28′	316° 28′	315° 28′	314° 28′	313° 28′
16 – 17	315° 26′	314° 26′	313° 26′	312° 26′	311° 26′	310° 26′	309° 26′	308° 26′	307° 26′	306° 26′
17 – 18	308° 26′	307° 26′	306° 26′	305° 26′	304° 26′	303° 26′	302° 26′	301° 26′	300° 26′	299° 26′
18 – 19	301° 28′	300° 28′	299° 28′	298° 28′	297° 28′	296° 28′	295° 28′	294° 28′	293° 28′	292° 28′
19 – 20	294° 32′	293° 32′	292° 32′	291° 32′	290° 32′	289° 32′	288° 32′	287° 32′	286° 32′	285° 32′
20 – 21	287° 38′	286° 38′	285° 38′	284° 38′	283° 38′	282° 38′	281° 38′	280° 38′	279° 38′	278° 38′
21 – 22	280° 46′	279° 46′	278° 46′	277° 46′	276° 46′	275° 46′	274° 46′	273° 46′	272° 46′	271° 46′
22 – 23	273° 56′	272° 56′	271° 56′	270° 56′	269° 56′	268° 56′	267° 56′	266° 56′	265° 56′	264° 56′
23 – 24	267° 08′	266° 08′	265° 08′	264° 08′	263° 08′	262° 08′	261° 08′	260° 08′	259° 08′	258° 08′
24 – 25	260° 22′	259° 22′	258° 22′	257° 22′	256° 22′	255° 22′	254° 22′	253° 22′	252° 22′	251° 22′
25 – 26	253° 38′	252° 38′	251° 38′	250° 38′	249° 38′	248° 38′	247° 38′	246° 38′	245° 38′	244° 38′
26 – 27	246° 56′	245° 56′	244° 56′	243° 56′	242° 56′	241° 56′	240° 56′	239° 56′	238° 56′	237° 56′
27 – 28	240° 16′	239° 16′	238° 16′	237° 16′	236° 16′	235° 16′	234° 16′	233° 16′	232° 16′	231° 16′
28 – 29	233° 38′	232° 38′	231° 38′	230° 38′	229° 38′	228° 38′	227° 38′	226° 38′	225° 38′	224° 38′
29 – 30	227° 02′	226° 02′	225° 02′	224° 02′	223° 02′	222° 02′	221° 02′	220° 02′	219° 02′	218° 02′
30 – 31	220° 28′	219° 28′	218° 28′	217° 28′	216° 28′	215° 28′	214° 28′	213° 28′	212° 28′	211° 28′
31 – 32	213° 56′	212° 56′	211° 56′	210° 56′	209° 56′	208° 56′	207° 56′	206° 56′	205° 56′	204° 56′
32 – 33	207° 26′	206° 26′	205° 26′	204° 26′	203° 26′	202° 26′	201° 26′	200° 26′	199° 26′	198° 26′
33 – 34	200° 58′	199° 58′	198° 58′	197° 58′	196° 58′	195° 58′	194° 58′	193° 58′	192° 58′	191° 58′
34 – 35	194° 32′	193° 32′	192° 32′	191° 32′	190° 32′	189° 32′	188° 32′	187° 32′	186° 32′	185° 32′

TABLE 1. Angular directions of the Mach lines running downward to the right for positive flow angles and upward to the right for negative flow angles.

TABLE 1E — $\mu + \theta$ For $\theta > 0$; $\mu - \theta$ For $\theta < 0$ — 1 Degree Steps

ω / θ	0 – 1	1 – 2	2 – 3	3 – 4	4 – 5	5 – 6	6 – 7	7 – 8	8 – 9	9 – 10
0 – 1	72° 36′	73° 36′	74° 36′	75° 36′	76° 36′	77° 36′	78° 36′	79° 36′	80° 36′	81° 36′
1 – 2	64° 57′	65° 57′	66° 57′	67° 57′	68° 57′	69° 57′	70° 57′	71° 57′	72° 57′	73° 57′
2 – 3	57° 27′	58° 27′	59° 27′	60° 27′	61° 27′	62° 27′	63° 27′	64° 27′	65° 27′	66° 27′
3 – 4	50° 01′	51° 01′	52° 01′	53° 01′	54° 01′	55° 01′	56° 01′	57° 01′	58° 01′	59° 01′
4 – 5	42° 39′	43° 39′	44° 39′	45° 39′	46° 39′	47° 39′	48° 39′	49° 39′	50° 39′	51° 39′
5 – 6	35° 20′	36° 20′	37° 20′	38° 20′	39° 20′	40° 20′	41° 20′	42° 20′	43° 20′	44° 20′
6 – 7	28° 03′	29° 03′	30° 03′	31° 03′	32° 03′	33° 03′	34° 03′	35° 03′	36° 03′	37° 03′
7 – 8	20° 48′	21° 48′	22° 48′	23° 48′	24° 48′	25° 48′	26° 48′	27° 48′	28° 48′	29° 48′
8 – 9	13° 34′	14° 34′	15° 34′	16° 34′	17° 34′	18° 34′	19° 34′	20° 34′	21° 34′	22° 34′
9 – 10	6° 21′	7° 21′	8° 21′	9° 21′	10° 21′	11° 21′	12° 21′	13° 21′	14° 21′	15° 21′
10 – 11	359° 08′	0° 08′	1° 08′	2° 08′	3° 08′	4° 08′	5° 08′	6° 08′	7° 08′	8° 08′
11 – 12	351° 56′	352° 56′	353° 56′	354° 56′	355° 56′	356° 56′	357° 56′	358° 56′	359° 56′	0° 56′
12 – 13	344° 46′	345° 46′	346° 46′	347° 46′	348° 46′	349° 46′	350° 46′	351° 46′	352° 46′	353° 46′
13 – 14	337° 38′	338° 38′	339° 38′	340° 38′	341° 38′	342° 38′	343° 38′	344° 38′	345° 38′	346° 38′
14 – 15	330° 32′	331° 32′	332° 32′	333° 32′	334° 32′	335° 32′	336° 32′	337° 32′	338° 32′	339° 32′
15 – 16	323° 28′	324° 28′	325° 28′	326° 28′	327° 28′	328° 28′	329° 28′	330° 28′	331° 28′	332° 28′
16 – 17	316° 26′	317° 26′	318° 26′	319° 26′	320° 26′	321° 26′	322° 26′	323° 26′	324° 26′	325° 26′
17 – 18	309° 26′	310° 26′	311° 26′	312° 26′	313° 26′	314° 26′	315° 26′	316° 26′	317° 26′	318° 26′
18 – 19	302° 28′	303° 28′	304° 28′	305° 28′	306° 28′	307° 28′	308° 28′	309° 28′	310° 28′	311° 28′
19 – 20	295° 32′	296° 32′	297° 32′	298° 32′	299° 32′	300° 32′	301° 32′	302° 32′	303° 32′	304° 32′
20 – 21	288° 38′	289° 38′	290° 38′	291° 38′	292° 38′	293° 38′	294° 38′	295° 38′	296° 38′	297° 38′
21 – 22	281° 46′	282° 46′	283° 46′	284° 46′	285° 46′	286° 46′	287° 46′	288° 46′	289° 46′	290° 46′
22 – 23	274° 56′	275° 56′	276° 56′	277° 56′	278° 56′	279° 56′	280° 56′	281° 56′	282° 56′	283° 56′
23 – 24	268° 08′	269° 08′	270° 08′	271° 08′	272° 08′	273° 08′	274° 08′	275° 08′	276° 08′	277° 08′
24 – 25	261° 22′	262° 22′	263° 22′	264° 22′	265° 22′	266° 22′	267° 22′	268° 22′	269° 22′	270° 22′
25 – 26	254° 38′	255° 38′	256° 38′	257° 38′	258° 38′	259° 38′	260° 38′	261° 38′	262° 38′	263° 38′
26 – 27	247° 56′	248° 56′	249° 56′	250° 56′	251° 56′	252° 56′	253° 56′	254° 56′	255° 56′	256° 56′
27 – 28	241° 16′	242° 16′	243° 16′	244° 16′	245° 16′	246° 16′	247° 16′	248° 16′	249° 16′	250° 16′
28 – 29	234° 38′	235° 38′	236° 38′	237° 38′	238° 38′	239° 38′	240° 38′	241° 38′	242° 38′	243° 38′
29 – 30	228° 02′	229° 02′	230° 02′	231° 02′	232° 02′	233° 02′	234° 02′	235° 02′	236° 02′	237° 02′
30 – 31	221° 28′	222° 28′	223° 28′	224° 28′	225° 28′	226° 28′	227° 28′	228° 28′	229° 28′	230° 28′
31 – 32	214° 56′	215° 56′	216° 56′	217° 56′	218° 56′	219° 56′	220° 56′	221° 56′	222° 56′	223° 56′
32 – 33	208° 26′	209° 26′	210° 26′	211° 26′	212° 26′	213° 26′	214° 26′	215° 26′	216° 26′	217° 26′
33 – 34	201° 58′	202° 58′	203° 58′	204° 58′	205° 58′	206° 58′	207° 58′	208° 58′	209° 58′	210° 58′
34 – 35	195° 32′	196° 32′	197° 32′	198° 32′	199° 32′	200° 32′	201° 32′	202° 32′	203° 32′	204° 32′

TABLE 2. Angular directions of the Mach lines running upward to the right for positive flow angles and downward to the right for negative flow angles.

$$\mu - \theta = 72.099° - \frac{1° + 0°}{2} = 71.599°$$

$$\mu - \theta = 71°36'$$

Where this Mach line reaches the lower boundary (see Fig. 1), it is reflected as an expansion wave in such a way that the angle of flow behind the line is parallel to the wall. The flow behind the reflected wave has expanded through a total Prandtl-Meyer angle of $\omega = 2°$ while the flow before the Mach line has expanded through a Prandtl-Meyer angle of $\omega = 1°$. The mean Mach line is given by the Prandtl-Meyer angle of $\omega = 1^1/_2°$ which is found from the tables of reference 2 to be $\mu = 64.450°$. The angle of the mean Mach line with the horizontal is

$$\mu + \theta = 64.450° + \frac{0° + 1°}{2} = 64.95°$$

$$\mu + \theta = 64°57'$$

Use of the Tables

Tables for $\mu + \theta$ and $\mu - \theta$ are given for steps of 1° in ω and θ by Tables 1 and 2. In constructing the Mach net, it is wise to put in each mesh the value of the Prandtl-Meyer angle and of the flow angle (see Fig. 1). If the flow direction is measured positive in the counter-clockwise direction, the Mach line running upward and to the right or downstream direction is the $\mu + \theta$ characteristic for $\theta > 0$. Since the table of $\mu + \theta$ contains only positive flow angles, the same Mach line for $\theta < 0$ is given by the $\mu - \theta$ table. Similarly, the angle of the Mach line downward and to the left is found in the table of $\mu - \theta$ for $\theta > 0$ and in the table of $\mu + \theta$ for $\theta < 0$. For example, the angle of Mach line AB in the figure is found in the third row and first column of Table 1 to be 59°27′, and the angle of the Mach line BC is found in the third row and second column of Table 2 to be 61°27′. In the tables, the Prandtl-Meyer angle is designated by ω and the flow angle by θ.

The tables give results for flow angles up to 10°. Higher flow angles can be found by adding (or subtracting) multiples of 10° to the angles in the tables.

References

[1] Arnold, B. H., *Method of Characteristics and Application to the Design of Two-Dimensional Supersonic Nozzles*, Boeing Document R4BW 12128.

[2] Naval Ordnance, *Handbook of Supersonic Aerodynamics*, Vol. II, Bureau of Ordnance, October 1, 1950.

[3] Puckett, A. E., *Supersonic Nozzle Design*, J. Applied Mech., pp. A-265–270, December, 1946.

[4] Ehlers, F. Edward, *A Simple Graphical Method of Calculating Two-Dimensional, Isentropic, Supersonic Flows Using the Brunning Drafting Machine*, Boeing Mathematical Note No. 120, November 28, 1955.

A Note on the Reflection of Sound Waves at an Oblique Shock†

C. T. Chang*

Aeronautics Department, The Johns Hopkins University, Baltimore, Md.

September 12, 1957

THE ONLY DISTURBANCES that can interact with a shock from downstream are sound waves. Following the general procedure of reference (1), it is shown in this note that the nature of the reflected sound waves and the reflection coefficient can be readily determined. If β is the shock angle and θ is the inclination of the normal to the wave front with respect to the downstream main-flow velocity U, and A the speed of sound of the downstream main flow, the wave front drifts along the shock at a speed of (see Fig. 1)

$$C_s = (A + U \cos\theta)/\cos(\theta - \beta) \tag{1}$$

Referring to the coordinate frame OXY, where the X axis is taken along the downstream effective flow velocity U_e, the problem can be reduced to a steady one.[1] The magnitude and inclination α of U_e is given by the law of sines

$$C_s/\sin\alpha = U_e/\sin\beta = U/\sin(\alpha - \beta) \tag{2}$$

As indicated previously,[1] disturbances corresponding to sound waves can be conveniently represented by the scalar potential ϕ, governed by a simple wave equation, thus

$$\phi = \phi_r(X + Y\cot\mu_e) + \phi_i(X - Y\cot\mu_e) \tag{3}$$

where

$$\mu_e = \text{arc sin}\,(A/U_e) \tag{4}$$

is the effective downstream Mach angle. Clearly, ϕ_i represents the given incident wave while ϕ_r represents the unknown reflected wave.

The component of the perturbed velocity taken along the Y axis, $\tilde{v}$, and the perturbed pressure $\tilde{p}$ are related to the scalar potential by

$$\tilde{v} = \phi_Y, \quad \tilde{p} = -\phi_X/\sin\mu_e \tag{5}$$

At the shock, they are related to the local shock angle ψ_Y by the condition

† The work reported was sponsored by Project Squid, which is jointly supported by the Office of Naval Research, The Office of Scientific Research (Air Force), and the Office of Ordnance Research (Army) under contract numbers N6-ORI-105 T.O. III, NR-098-038.

* Formerly, Research Assistant, Aeronautics Department, The Johns Hopkins University. Now at the Division of Engineering and Applied Physics, Harvard University.

$$\begin{bmatrix} p_r \\ \bar{p}_r \end{bmatrix} = \begin{bmatrix} p_i \\ \bar{p}_i \end{bmatrix} = \begin{bmatrix} \pi_{21}\,(M\cos\beta - C_s/A) \\ \pi_{31}\,(M\cos\beta - C_s/A)\cos(\alpha-\beta) + \pi_{41}\sin(\alpha-\beta) \end{bmatrix} \sin(\alpha-\beta)\psi_Y \quad \text{at } X\sin(\alpha-\beta) + Y\cos(\alpha-\beta) = 0 \tag{6}$$

where flow parameters with subscript (r) are those pertaining to reflected waves while parameters with subscript (i) are those pertaining to incident waves. π_{31}, π_{e1}, and π_{41}, as indicated in references (1) and (2), are parameters which depend on the shock strengh χ, defined as the ratio of unperturbed pressures across the shock.

Using Eqs. (3), (5) and (6), it can be deduced that[2]

$$p_r/p_i = K(\theta, \beta, \chi) \tag{7}$$

The parameter K can now be viewed as a reflection coefficient. For a given medium, K generally is a function of the shock strength χ, the shock angle β, and the inclination θ of the incident wave. Its variation with respect to θ at a fixed value of β is given in Fig. 1.

A positive value of K indicates the reflected wave is of the same kind as the incident wave, namely, an expansion wave reflects as an expansion wave; a negative value of K indicates the reflected wave is of the opposite kind as the incident wave, namely, an expansion wave reflects as a compression wave. For a given shock strength χ, there are two inclinations of the incident wave at which no reflection occurs; one of them corresponds to the normal incidence, the other one depends on the particular value of the shock strength χ under consideration.

Once the reflected sound wave is known, the shock deflection ψ_Y can be determined. Finally, the accompanying vorticity and entropy disturbances generated at the shock can be evaluated from the remaining conditions at the shock.

References

[1] Chang, C. T., *Interaction of a Plane Shock and Oblique Plane Disturbances With Special Reference to Entropy Waves*, Journal of the Aeronautical Sciences, Vol. 24, No. 9, pp. 675–682, September, 1957.

[2] Chang, C. T., *On the Interaction of Weak Disturbances and a Plane Shock of Arbitrary Strength in a Perfect Gas*, Dissertation, The Johns Hopkins University, 1955.

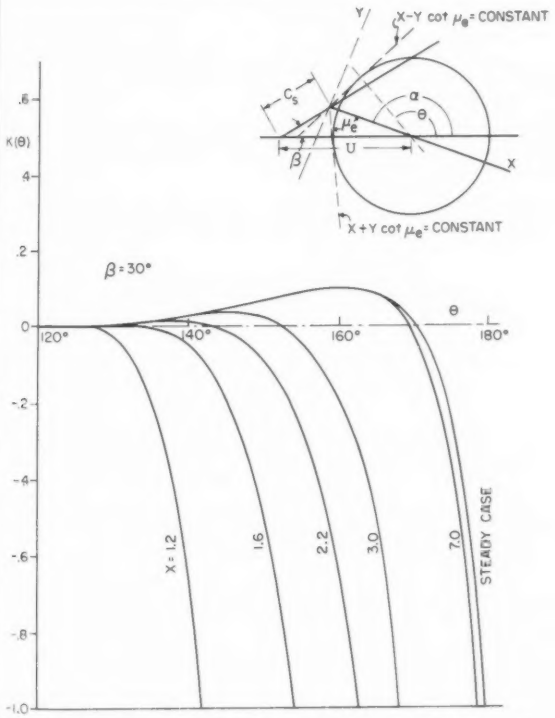

FIG. 1. Sound-wave reflection coefficient vs. incident angle.

Application of Görtler's Series Method to the Boundary-Layer Energy Equation

E. M. Sparrow
Lewis Flight Propulsion Laboratory, NACA, Cleveland, Ohio

September 20, 1957

Introduction

IN A RECENT ARTICLE of considerable importance, Görtler[1] has presented a new series method for calculation of steady laminar incompressible boundary-layer flows under conditions of variable free-stream velocity. Our purpose here is to sketch out the application of his method to the heat-transfer problem for a two-dimensional body with variable free-stream velocity. Both the surface temperature T_w and the ambient temperature T_∞ are taken to be uniform, but, of course, $T_w \neq T_\infty$. Such an extension is easily carried out provided that full use is made of Görtler's results, and, in fact, we are immediately able to provide numerical results for the heat transfer from a symmetrical body with a stagnation point for $Pr = 1$.

Detailed consideration was given by Görtler to free-stream velocities of the type

$$U(x) = x^m\{s_0 + s_1x^{m+1} + s_2x^{2(m+1)} + \ldots\} \tag{1}$$

$$U(x) = x^m\{s_0 + s_{1/2}x^{1/2(m+1)} + s_1x^{m+1} + s_{3/2}x^{3/2(m+1)} + \ldots\} \tag{2}$$

Numerical treatment was carried out for the cases $m = 0$ and $m = 1$ for the first series, and for $m = 1$ for the second series. For these situations, universal functions have been computed[2] which may be used in determining the details of the boundary-layer flow on two-dimensional bodies.

Further, Görtler considered the case of an infinite cylinder in yaw subject to variable free-stream velocities of the type noted above. He formulated the equations for determining the cross-flow velocity component W (parallel to cylinder axis) and gives universal functions[2] corresponding to $U(x)$ of Eq. (1) for $m = 1$.

The Heat-Transfer Problem

We start with the energy equation for incompressible steady flow over a two-dimensional body and then introduce the following variables (due to Görtler)

$$\left.\begin{aligned} \eta &= yU(x)\Big/\sqrt{2\nu\int_0^x U(x)\,dx} \\ \xi &= (1/\nu)\int_0^x U(x)\,dx \\ F(\xi,\eta) &= \psi\Big/\sqrt{\nu\int_0^x U(x)\,dx} \end{aligned}\right\} \tag{3}$$

The result of this substitution is

$$(1/Pr)\Theta_{\eta\eta} + (F + 2\xi F_\xi)\Theta_\eta = 2\xi F_\eta\Theta_\xi \tag{4a}$$

where Pr is the Prandtl number and $\Theta = (T - T_w)/(T_\infty - T_w)$. The appropriate boundary conditions are

$$\Theta(\xi, 0) = 0, \quad \Theta(\xi, \eta) \to 1 \text{ as } \eta \to \infty \tag{4b}$$

But, except for the factor $1/Pr$, Eqs. (4a) and (4b) are identical to Görtler's Eq. (83) for the cross-flow velocity component W of the yawed cylinder problem. So, the mathematical formulation and results for the velocity problem on the yawed cylinder become applicable, with only simple modifications, to our two-dimensional heat-transfer problem. In particular, for $Pr = 1$, there is a one-to-one correspondence in the results for Θ and W.

Results For $Pr = 1$

As has already been noted, there are available[2] universal functions for the W problem corresponding to a free-stream velocity of Eq. (1) with $m = 1$—i.e., for

$$U(x) = s_0x + s_1x^3 + s_2x^5 + \dots \tag{5}$$

(Eq. (5) corresponds to the flow about a symmetric body with a stagnation point.) For this free-stream velocity, we can easily write down an expression for the local heat flux q at the surface of our two-dimensional body. First introduce the *principal function* $\beta(\xi)$ according to the definition

$$\beta(\xi) = 2U'(x)\int_0^x U(x)\,dx \Big/ U^2(x) \tag{6}$$

and then set $\beta(\xi) = \beta_0 + \beta_1\xi + \beta_2\xi^2 + \dots$ for the present case. With this definition, the heat-transfer result is

$$\begin{aligned}[Nu_x/Re_x](2\xi)^{1/2} = {} & 0.5705 + (0.06212\,\beta_1)\xi + \\ & (-0.02105\,\beta_1^2 + 0.06345\,\beta_2)\xi^2 + (0.00826\,\beta_1^3 - \\ & 0.03880\,\beta_1\beta_2 + 0.06273\,\beta_3)\xi^3 + (-0.00364\,\beta_1^4 + \\ & 0.02222\,\beta_1^2\beta_2 - 0.03632\,\beta_1\beta_3 - 0.01769\,\beta_2^2 + \\ & 0.06150\,\beta_4)\xi^4 + (0.00175\,\beta_1^5 - 0.01299\,\beta_1^3\beta_2 + 0.02050 \times \\ & \beta_1^2\beta_3 + 0.01994\,\beta_1\beta_2^2 - 0.03437\,\beta_1\beta_4 - 0.03300\,\beta_2\beta_3 + \\ & 0.06016\,\beta_5)\xi^5 \end{aligned} \tag{7}$$

where $Nu_x = qx/(T_w - T_\infty)k$, $Re_x = Ux/\nu$

The relationship between ξ and x is provided by Eq. (3). As a simple illustration, suppose that $U(x) = s_0x$, $(s_1 = s_2 = \dots 0)$. Then, $\xi = Re_x/2$ and $\beta_0 = 1$, $\beta_1 = \beta_2 \dots = 0$. For this situation, the heat-transfer result becomes: $Nu_x/Re_x^{1/2} = 0.5705$.

For the velocity variation of Eq. (1) with $m = 0$ (flow around bodies with a cuspidal point at leading edge), Görtler does not provide universal functions for the W problem. Hence, results for the temperature problem cannot be written without considerable further computation. The necessary differential equations are given as Eqs. (104) through (109) in Görtler's paper. It is only necessary to change all the W's (or w's) to thetas.

For the free-stream velocity of Eq. (2), Görtler does not solve the yawed cylinder problem. So, the differential equations for the two-dimensional temperature problem are not directly available there. But, they may be easily obtained by following Görtler's procedure. Introducing the expansions

$$F(\xi,\eta) = \sum_{n=0}^{\infty} F_{n/2}(\eta)\xi^{n/2}, \quad \Theta(\xi,\eta) = \sum_{n=0}^{\infty} \Theta_{n/2}(\eta)\xi^{n/2} \tag{8}$$

into Eq. (4), we find the following differential equations for computing the temperature distribution corresponding to the free-stream velocity of Eq. (2).

$$\Theta_0'' + F_0\Theta_0' = 0, \quad \Theta_0(0) = 0, \quad \Theta_0(\infty) = 1 \tag{9a}$$

$$\left.\begin{aligned} &\Theta_{n/2}'' + F_0\Theta_{n/2}' - nF_0'\Theta_{n/2} = \\ &\qquad \sum_{j=1}^{n}(n-j)F_{j/2}'\Theta_{1/2(n-j)} - (j+1)F_{j/2}\Theta_{1/2}'_{(n-j)} \\ &\Theta_{n/2}(0) = \Theta_{n/2}(\infty) = 0, \quad n = 1, 2, 3 \dots \end{aligned}\right\} \tag{9b}$$

Then, the functions $\Theta_{n/2}$ are written in terms of universal functions in precisely the same fashion as is done by Görtler for the $F_{n/2}$ in his Eq. (114). Tabulated values for the $F_{n/2}$ are available for $m = 1$.

Extension To $Pr \neq 1$

The series method of solution for Eq. (4) with $Pr \neq 1$ can be formulated without additional effort. For the free-stream velocity of Eq. (1), it is only necessary to take Görtler's Eqs. (104) to (109); first replace all W's (or w's) by thetas, and then multiply all second derivatives by $1/Pr$.

For the velocity variation of Eq. (2), all that is required is to replace Θ'' in Eqs. (9a) and (9b) by Θ''/Pr.

The universal functions for $F(\xi,\eta)$ which are compiled by Görtler are, of course, usable as input data in the solution of Eq. (4) for any Prandtl Number.

References

[1] Görtler, Henry, *A New Series for the Calculation of Steady Laminar Boundary Layer Flows*, J. Math. Mech., Vol. 6, No. 1, pp. 1–66, 1957.

[2] *Progress Report No. 37*, Harvard University Computation Laboratory, March, 1955.

Rotating Stall in a Single-Stage Axial Compressor

(*Continued from page 10*)

[7] Stenning, Alan H., *Stall Propagation in Cascades of Airfoils*, Journal of the Aeronautical Sciences, Vol. 21, No. 10, pp. 711–713, October, 1954.

[8] Marble, Frank E., *Propagation of Stall in a Compressor Blade Row*, Journal of the Aeronautical Sciences, Vol. 22, No. 8, pp. 541–544, August, 1955.

[9] Sears, W. R., *Rotating Stall in Axial Compressors*, Z. Angew. Math. Phys., Vol. 6, No. 6, pp. 429–455, 1955.

[10] Fabri, J., and Jarlan, L., Comptes Rendus, Académie des Sciences, Paris, Vol. 243, No. 23, 1956.

[11] Fabri, J., and Siestrunck, R., Comptes Rendus, Académie des Sciences, Paris, Vol. 243, No. 22, pp. 1718–1721, 1956.

[12] Valensi, J., *Etude de l'Écoulement de l'Air Autour d'une Helice*, Publications Scientifiques et Techniques du Ministère de l'Air, No. 73, 1935.

[13] Valensi, J., *Application de la Méthode des Fumées a l'Etude des Champs Aérodynamiques*, Publications Scientifiques et Techniques du Ministère de l'Air, No. 128, 1938.

[14] Patterson, John L., *A Miniature Electrical Pressure Gage Utilizing a Stretched Flat Diaphragm*, NACA TN 2659, 1952.